

การกักตัวของเส้นสนามแม่เหล็กในเกาะของความปั่นป่วน



นายนิมิตร กิมประพันธ์

สถาบันวิทยบริการ

จุฬาลงกรณ์มหาวิทยาลัย

วิทยานิพนธ์นี้เป็นส่วนหนึ่งของการศึกษาตามหลักสูตรปริญญาวิทยาศาสตรมหาบัณฑิต

สาขาวิชาฟิสิกส์ ภาควิชาฟิสิกส์

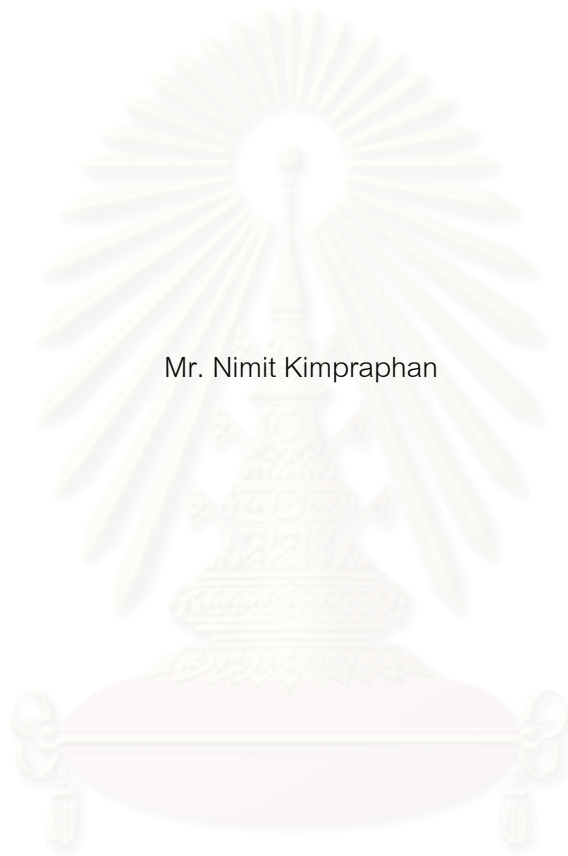
คณะวิทยาศาสตร์ จุฬาลงกรณ์มหาวิทยาลัย

ปีการศึกษา 2548

ISBN 974-14-3740-4

ลิขสิทธิ์ของจุฬาลงกรณ์มหาวิทยาลัย

TRAPPING OF MAGNETIC FIELD LINES IN ISLANDS OF TURBULENCE



Mr. Nimit Kimpraphan

สถาบันวิทยบริการ  
A Thesis Submitted in Partial Fulfillment of the Requirements  
for the Degree of Master of Science Program in Physics

Department of Physics

Faculty of Science

Chulalongkorn University

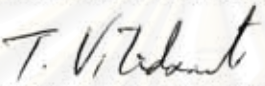
Academic Year 2005

ISBN 974-14-3740-4


Thesis Title TRAPPING OF MAGNETIC FIELD LINES IN ISLANDS OF  
TURBULENCE  
By Mr. Nimit Kimpraphan  
Field of study Physics  
Thesis Advisor Assistant Professor Sojiphong Chatraphorn, Ph.D.  
Thesis Co-advisor Associate Professor David Ruffolo, Ph.D.

---

Accepted by the Faculty of Science, Chulalongkorn University in Partial  
Fulfillment of the Requirements for the Master's Degree


  
.....Deputy Dean for Administrative Affairs,  
Acting Dean, The Faculty of Science  
(Associate Professor Tharapong Vitidsant, Ph.D.)

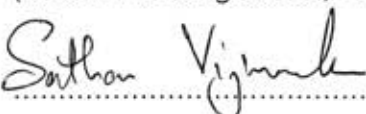
THESIS COMMITTEE

  
..... Chairman  
(Associate Professor Mayuree Natenapit, Ph.D.)

  
..... Thesis Advisor  
(Assistant Professor Sojiphong Chatraphorn, Ph.D.)

  
..... Thesis Co-advisor  
(Associate Professor David Ruffolo, Ph.D.)

  
..... Member  
(Nakorn Phaisangittisakul, Ph.D.)

  
..... Member  
(Sathon Vijarnwannahluk, Ph.D.)

นิมิตร กิมประพันธ์ : การกักตัวของเส้นสนามแม่เหล็กในเกาะของความปั่นป่วน (TRANSFER OF MAGNETIC FIELD LINES BETWEEN ISLANDS OF TURBULENCE)

อ. ที่ปรึกษา : ศศ.ดร. โสจิพงษ์ ฉัตรรากรณ์, อ.ที่ปรึกษาร่วม : รศ.ดร.เควิต รุฟโฟโล,  
124 หน้า. ISBN 974-14-3740-4.

เราพิจารณากลุ่มของเส้นสนามแม่เหล็กในสนามปั่นป่วน โดยใช้แบบจำลองสององค์ประกอบของสนามแม่เหล็กปั่นป่วน ซึ่งประกอบด้วยองค์ประกอบแบบแผ่นและแบบสองมิติตามแมทริวส์และคณะ (1990) สนามปั่นป่วนในรูปแบบนี้ประสบความสำเร็จในการอธิบายปรากฏการณ์ครอปเอาท์ (dropout) ของอนุภาคพลังงานสูงที่มาจากดวงอาทิตย์ เราสามารถพิจารณาว่าอนุภาคพลังงานสูงตามเส้นสนามแม่เหล็กจากดวงอาทิตย์ เส้นสนามแม่เหล็กเหล่านี้ถูกกักอยู่ในโครงสร้างขนาดเล็กที่เรียกว่า "เกาะของความปั่นป่วน" ชั่วครวณก่อนที่จะพุ่งกระจายทั่วทั้งอวกาศ เราได้พัฒนาระเบียบวิธีในการจำลอง ได้แก่ ระเบียบวิธีกรนับกล่อง (Box-Counting), ระเบียบวิธีแอนไอโซทรอปี (Anisotropy), ระเบียบวิธีแลตทิซคู่ (Dual Lattice), และระเบียบวิธีส่วนประกอบमुखสำคัญ (Principal Components) และใช้วิเคราะห์ข้อมูลจากการตามเส้นสนามแม่เหล็กในสนามปั่นป่วน โดยเราเปลี่ยนค่าพารามิเตอร์ต่าง ๆ ได้แก่ อัตราส่วนของพลังงานของการกวัดไกวต่อสนามเฉลี่ย รัศมีของวงกลมตั้งต้น มาตรการส่วนความยาวขนาน และมาตรการส่วนความยาวตั้งฉาก จากผลการวิเคราะห์เราสามารถบอกถึงเงื่อนไขและมาตรการส่วนความยาวที่ครอปเอาท์เกิดขึ้น

สถาบันวิทยบริการ  
จุฬาลงกรณ์มหาวิทยาลัย

ภาควิชา ... ฟิสิกส์..... ลายมือชื่อนิมิตร..... ปิยะ คุ้มวงศ์.....  
สาขาวิชา ... ฟิสิกส์..... ลายมือชื่ออาจารย์ที่ปรึกษา..... โสจิพงษ์ ฉัตรรากรณ์.....  
ปีการศึกษา ... 2548..... ลายมือชื่ออาจารย์ที่ปรึกษาร่วม..... เควิต รุฟโฟโล.....

## 4572345023 : MAJOR PHYSICS

KEY WORD: MAGNETIC FIELD LINES / TURBULENCE / DROPOUT / TRAPPING / MAGNETIC ISLANDS

NIMIT KIMPRAPHAN : TRAPPING OF MAGNETIC FIELD LINES IN ISLANDS OF  
TURBULENCE. THESIS ADVISOR : ASST. PROF. SOJIPHONG CHATRAPHORN,  
Ph.D., THESIS COADVISOR : ASSOC. PROF. DAVID RUFFOLO, Ph.D., 124 pp. ISBN  
974-14-3740-4.

Groups of magnetic field lines in turbulence fields are considered. We use the two-component model of magnetic turbulence, including the slab and the two-dimensional components following Matthaeus et al. (1990). This form of the turbulent field can successfully explain the dropout phenomena of solar energetic particles. We can consider that the solar energetic particles follow the magnetic field lines from the Sun. These magnetic field lines are trapped in the small-scale structures called the "magnetic islands" for a while before diffusing throughout all space. Simulation methods, e.g., the Box-Counting Method, the Anisotropy Method, the Dual Lattice Method, and the Principal Component Method, are developed and used to analyze the data from tracing the magnetic field lines in turbulence fields. We vary the magnetic parameter values, e.g., the fluctuation energy to the mean field energy ratio, the radius of the initial circle, the parallel length scale, and the perpendicular length scale. From the analysis results, we can obtain conditions and length scales over which dropouts can occur.

สถาบันวิทยบริการ  
จุฬาลงกรณ์มหาวิทยาลัย

Department ...Physics..... Student's signature *Nimit Kimpraphan*  
Field of study ...Physics..... Advisor's signature *S. Chatrathorn*  
Academic year ...2005..... Co-advisor's signature *David Ruffolo*



# ACKNOWLEDGEMENTS

First of all, I am very grateful to my family for their very strong support and cheerfulness. I am very proud to be their son.

I would like to express my gratitude to my co-advisor, Assoc. Prof. Dr. David Ruffolo, for his attention, guidance, and help to me in everythings with endurance and kindness.

I would like to give my sincere thanks to my advisor, Assist. Prof. Dr. Sojiphong Chatraphorn, and my thesis committee, Assoc. Prof. Dr. Mayuree Natenapit, Dr. Nakorn Phaisangittisakul, and Dr. Sathon Vijarnwannaluk, for reading and offering suggestions on my thesis.

I would like to thank Prof. Dr. George Rowlands from the University of Warwick, Assist. Prof. Dr. Michael Antony Allen, Dr. Julian Poulter and Dr. Alejandro Sáiz from Mahidol University very much for discussions and giving some ideas.

I would like to thank Dr. Piyanate Chuychai, Mr. Peera Pongkitiwanichkul, and Mr. Jakapan Meechai, for their helpful discussions about magnetic turbulence, especially Mr. Peera for allowing me to use his computer program for tracing the magnetic field lines.

I also thank all of the members of the Space Physics and Energetic Particles Lab, present and former, for their friendliness.

Finally, I would like to give special thanks to Miss Premtip Thanarung-  
rangkul, for her willpower and care.

This work was supported by the Thailand Research Fund and the Commission for Higher Education.

# CONTENTS

page

<b>Abstract in Thai</b> .....	<b>iv</b>
<b>Abstract in English</b> .....	<b>v</b>
<b>Acknowledgements</b> .....	<b>vi</b>
<b>Contents</b> .....	<b>vii</b>
<b>List of Figures</b> .....	<b>ix</b>

<b>CHAPTER I INTRODUCTION</b> .....	<b>1</b>
1.1 Introduction.....	1
1.2 Objectives.....	2
1.3 Outline.....	2

<b>CHAPTER II THEORETICAL BACKGROUND</b> .....	<b>3</b>
2.1 The Sun and Interplanetary Magnetic Field.....	3
2.1.1 Solar Activity.....	3
2.1.2 Interplanetary Magnetic Field.....	6
2.1.3 Paradox of Dropouts.....	6
2.2 Model of the Magnetic Turbulence.....	10
2.2.1 Turbulence in Nature.....	10
2.2.2 Turbulence in the Interplanetary Magnetic Field.....	13
2.2.3 Diffusion Coefficient.....	16
2.3 Simulations of Turbulent Magnetic Fields.....	23
2.3.1 Energy Cascade and Kolmogorov.....	23
2.3.2 Generating Representations of Turbulent Magnetic Fields.....	25

<b>CHAPTER III DATA ANALYSIS METHODS</b> .....	29
3.1 Box-Counting Dimension.....	30
3.1.1 Method .....	30
3.1.2 Process.....	32
3.2 Anisotropy.....	32
3.2.1 Method .....	32
3.2.2 Process.....	38
3.3 Dual Lattice .....	39
3.3.1 Method .....	39
3.3.2 Process.....	40
3.4 Principal Components .....	40
3.4.1 Method .....	40
3.5.2 Process.....	44
<b>CHAPTER IV RESULTS AND DISCUSSIONS</b> .....	45
4.1 Box-Counting Dimension.....	45
4.2 Anisotropy.....	49
4.3 Dual Lattice .....	79
4.4 Principal Components .....	108
<b>CHAPTER V SUMMARY</b> .....	117
<b>References</b> .....	<b>121</b>
<b>Vitae</b> .....	<b>124</b>



# LIST OF FIGURES

page

- Figure 2.1 a) Groups of sunspots and location of a major flare that occurred on October 28<sup>th</sup>, 2003. The picture on the left was taken in white light, and shows the active region (sunspot group) that caused the flare. The picture on the right was taken in extreme ultraviolet light, showing the flare. b) A coronal mass ejection, which occurred on August 18<sup>th</sup>, 1980. This picture was taken in white light by blocking the Sun, shading the strong sunlight. (Picture credits: a) [http://earthobservatory.nasa.gov/Newsroom/NewImages/images.php3?img\\_id=16345](http://earthobservatory.nasa.gov/Newsroom/NewImages/images.php3?img_id=16345) b) P. Charbonneau and O. R. White) ..... 4
- Figure 2.2 Effect of solar energetic particles and interplanetary shocks to the Earth. (Picture credit: L. J. Lanzerotti) ..... 5
- Figure 2.3 The structure of solar wind, the interplanetary magnetic field and the trajectory of high energy particles along the interplanetary magnetic field. .... 7
- Figure 2.4 Data of two impulsive solar flares occurring on January 9<sup>th</sup> – 10<sup>th</sup>, 1999 as detected by the ULEIS instrument on the *ACE* spacecraft. (a) Scatter plot of energy of H-Fe ions in MeV per nucleon versus arrival time at 1 AU. (b) H-Fe counts versus time in  $\sim 14$  minute bins. The vertical lines show dropout features. (c) Interplanetary magnetic field angle in the geocentric solar ecliptic (GSE)  $x - y$  plane. (d) Interplanetary magnetic field angle normal to the GSE  $x - y$  plane. We see that dropouts do not correspond to IMF discontinuities. (Picture credit: Mazur et al. 2000) ..... 8

- Figure 2.5 Locations of *Ulysses* during Day 250, 2000 to Day 17, 2001 compared with the Sun, Earth, and equatorial plane. (Picture credit: McKibben et al. 2001) ..... 9
- Figure 2.6 Plot between the flux of  $\sim 30 - 70$  MeV of solar energetic protons versus time (six hour averages) during Day 250, 2000 to Day 17, 2001. The black line traces data from the *Ulysses* spacecraft and the light line traces data from the *IMP-8* spacecraft. (Picture credit: McKibben et al. 2001) ..... 9
- Figure 2.7 Illustration of interplanetary magnetic field lines populated with solar energetic particles from a localized source region near the Sun, as expected for an impulsive solar flare. At the radius of Earth orbit, some magnetic field lines are trapped in some regions of the “core” while other magnetic field lines are spread out widely in the “halo” region. (Picture credit: Ruffolo et al. 2003) ..... 11
- Figure 2.8 Trace of five magnetic field lines in pure slab field with varied initial positions. Because  $\vec{b}^{slab}$  depends on only  $z$ , all magnetic field lines undergo the same random walk in  $x(z)$  and  $y(z)$ . ..... 14
- Figure 2.9 Contour plot of the potential function  $a(x, y)$ . Light areas are the local maxima and dark areas are the local minima. ..... 16
- Figure 2.10 Trace of a magnetic field line in pure 2D turbulence. This trace uses the potential function shown in Fig. 2.9. If we project the magnetic field line into  $x - y$  plane, it follows a contour of constant  $a(x, y)$ . ..... 17

Figure 2.11 Illustration of the magnetic field line random walk perpendicular to the mean field ( $\Delta x$ ), displacement between nearby field lines ( $X \equiv x_2 - x_1$ ), and their separation ( $\Delta X \equiv X - X_0$ ). (Picture credit: Ruffolo et al. 2004) .....	19
Figure 2.12 Schematic of two random field lines and definitions of various quantities. (Picture credit: Ruffolo et al. 2004) .....	19
Figure 2.13 Illustration of the Richardson cascade. (Picture credit: <a href="http://www.ipp.mpg.de/~fsj/PAPERS_1/tutorial_1.pdf">http://www.ipp.mpg.de/~fsj/PAPERS_1/tutorial_1.pdf</a> ) .....	24
Figure 2.14 The Kolmogorov spectrum. (Picture credit: Chuychai 2005) .....	26
Figure 3.1 Covering a line, a surface, and a solid cube with cubes of side length $\epsilon$ . (Picture credit: <a href="http://www.math.sunysb.edu/~scatt/Book331/Fractal_Dimension.html">http://www.math.sunysb.edu/~scatt/Book331/Fractal_Dimension.html</a> ) .....	31
Figure 3.2 Scatter plot of magnetic field lines in slab+2D turbulent field, for varying distance $\Delta z$ along the mean field. The energy ratio between the slab and 2D components in this simulation is 20:80 and all initial positions of magnetic field lines are at $z = 0$ . .....	33
Figure 3.3 Initial positions of magnetic field lines in a pure slab turbulent field. ..	34
Figure 3.4 Scatter plot of magnetic field lines in pure slab turbulence. The initial positions of these magnetic field lines are in a specific circle in the $x - y$ plane but at random $z$ locations. ....	35

Figure 3.5 Illustration of the summation of direction vectors as a measure of Dual lattice. Area 1 is at the edge of a group of magnetic field lines while area 2 is inside a group of magnetic field lines. Direction vectors to point within the dashed circle are summed. We can see that the summation of direction vectors in area 1 is larger than the summation of direction vectors in area 2. The energy ratio between the slab and 2D component in this simulations is 20:80. The initial positions of magnetic field lines are located in a circle with radius equal  $0.5\lambda_{\perp}$  in  $x - y$  plane at  $z = 0$ . . . . . 37

Figure 3.6 Illustration of the Dual Lattice Method. In this work, we define that if the number of magnetic field lines in one box more than 6 times greater or lesser than that in the neighboring box, we will decide that the junction between these boxes is at the edge of a group of magnetic field lines and count it. The junction between the central box and the right box is considered to be at the edge of a group of magnetic field lines, while that between the left box and central box is not. . . . . 41

Figure 3.7 Illustration of the principal components. The top figures show the group of magnetic field lines in pure slab turbulence with a random initial position in  $z$ . The principal components of this group of magnetic field lines in both directions have similar lengths. The figures on the bottom show the group of magnetic field lines in a slab+2D field. The principal component of this group of magnetic field lines is longer in one direction than the other one. Furthermore, the ratio of principal components of the group of magnetic field lines in the slab+2D field at low  $z$  is greater than the ratio of principal components at higher  $z$ . . . . . 43

Figure 4.1 The number of boxes containing the magnetic field lines vs. the size of the boxes at $\Delta z = 0$ .	46
Figure 4.2 The number of boxes containing the magnetic field lines vs. the size of the boxes at $\Delta z = 20$ .	46
Figure 4.3 The number of boxes containing the magnetic field lines vs. the size of the boxes at $\Delta z = 40$ .	47
Figure 4.4 The number of boxes containing the magnetic field lines vs. the size of the boxes at $\Delta z = 60$ .	47
Figure 4.5 The number of boxes containing the magnetic field lines vs. the size of the boxes at $\Delta z = 80$ .	48
Figure 4.6 The number of boxes containing the magnetic field lines vs. the size of the boxes at $\Delta z = 99$ .	48
Figure 4.7 Anisotropy number vs. $\Delta z$ when the turbulence fluctuation to mean field ratio is 0.25.	51
Figure 4.8 Anisotropy number vs. $\Delta z$ when the turbulence fluctuation to mean field ratio is 0.50.	52
Figure 4.9 Anisotropy number vs. $\Delta z$ when the turbulence fluctuation to mean field ratio is 0.75.	53
Figure 4.10 Anisotropy number vs. $\Delta z$ when the turbulence fluctuation to mean field ratio is 1.00.	54
Figure 4.11 Anisotropy number vs. $\Delta z$ when the turbulence fluctuation to mean field ratio is 2.00.	55
Figure 4.12 Anisotropy number vs. $\Delta z$ when the radius of the initial circle is $0.5\lambda_{\perp}$ .	58

Figure 4.13 Anisotropy number vs. $\Delta z$ when the radius of the initial circle is $1.0\lambda_{\perp}$ . . . . .	59
Figure 4.14 Anisotropy number vs. $\Delta z$ when the radius of the initial circle is $2.0\lambda_{\perp}$ . . . . .	60
Figure 4.15 Anisotropy number vs. $\Delta z$ when the radius of the initial circle is $4.0\lambda_{\perp}$ . . . . .	61
Figure 4.16 Anisotropy number vs. $\Delta z$ when the radius of the initial circle is $8.0\lambda_{\perp}$ . . . . .	62
Figure 4.17 Anisotropy number vs. $\Delta z$ when the radius of the initial circle is $16.0\lambda_{\perp}$ . . . . .	63
Figure 4.18 Anisotropy number vs. $\Delta z$ when the radius of the initial circle is $32.0\lambda_{\perp}$ . . . . .	64
Figure 4.19 Anisotropy number vs. $\Delta z$ when the parallel length scale is $0.25\lambda_{\perp}$ . . . . .	66
Figure 4.20 Anisotropy number vs. $\Delta z$ when the parallel length scale is $0.5\lambda_{\perp}$ . . . . .	67
Figure 4.21 Anisotropy number vs. $\Delta z$ when the parallel length scale is $1.0\lambda_{\perp}$ . . . . .	68
Figure 4.22 Anisotropy number vs. $\Delta z$ when the parallel length scale is $2.0\lambda_{\perp}$ . . . . .	69
Figure 4.23 Anisotropy number vs. $\Delta z$ when the parallel length scale is $5.0\lambda_{\perp}$ . . . . .	70
Figure 4.24 Anisotropy number vs. $\Delta z$ when the parallel length scale is $10.0\lambda_{\perp}$ . . . . .	71



Figure 4.25 Anisotropy number vs. $\Delta z$ when the parallel length scale is $20.0\lambda_{\perp}$ .	72
Figure 4.26 Anisotropy number vs. $\Delta z$ when the perpendicular length scale is $2.0\lambda_{\perp}$ .	74
Figure 4.27 Anisotropy number vs. $\Delta z$ when the perpendicular length scale is $5.0\lambda_{\perp}$ .	75
Figure 4.28 Anisotropy number vs. $\Delta z$ when the perpendicular length scale is $10.0\lambda_{\perp}$ .	76
Figure 4.29 Anisotropy number vs. $\Delta z$ when the perpendicular length scale is $20.0\lambda_{\perp}$ .	77
Figure 4.30 Anisotropy number vs. $\Delta z$ when the perpendicular length scale is $40.0\lambda_{\perp}$ .	78
Figure 4.31 Dual lattice number vs. $\Delta z$ when the turbulence fluctuation to mean field ratio is 0.25.	80
Figure 4.32 Dual lattice number vs. $\Delta z$ when the turbulence fluctuation to mean field ratio is 0.50.	81
Figure 4.33 Dual lattice number vs. $\Delta z$ when the turbulence fluctuation to mean field ratio is 0.75.	82
Figure 4.34 Dual lattice number vs. $\Delta z$ when the turbulence fluctuation to mean field ratio is 1.00.	83
Figure 4.35 Dual lattice number vs. $\Delta z$ when the turbulence fluctuation to mean field ratio is 2.00.	84
Figure 4.36 Dual lattice number vs. $\Delta z$ when the radius of the initial circle is $0.5\lambda_{\perp}$ .	87

Figure 4.37 Dual lattice number vs. $\Delta z$ when the radius of the initial circle is $1.0\lambda_{\perp}$ . . . . .	88
Figure 4.38 Dual lattice number vs. $\Delta z$ when the radius of the initial circle is $2.0\lambda_{\perp}$ . . . . .	89
Figure 4.39 Dual lattice number vs. $\Delta z$ when the radius of the initial circle is $4.0\lambda_{\perp}$ . . . . .	90
Figure 4.40 Dual lattice number vs. $\Delta z$ when the radius of the initial circle is $8.0\lambda_{\perp}$ . . . . .	91
Figure 4.41 Dual lattice number vs. $\Delta z$ when the radius of the initial circle is $16.0\lambda_{\perp}$ . . . . .	92
Figure 4.42 Dual lattice number vs. $\Delta z$ when the radius of the initial circle is $32.0\lambda_{\perp}$ . . . . .	93
Figure 4.43 Dual lattice number vs. $\Delta z$ when the parallel length scale is $0.25\lambda_{\perp}$ . . . . .	95
Figure 4.44 Dual lattice number vs. $\Delta z$ when the parallel length scale is $0.5\lambda_{\perp}$ . . . . .	96
Figure 4.45 Dual lattice number vs. $\Delta z$ when the parallel length scale is $1.0\lambda_{\perp}$ . . . . .	97
Figure 4.46 Dual lattice number vs. $\Delta z$ when the parallel length scale is $2.0\lambda_{\perp}$ . . . . .	98
Figure 4.47 Dual lattice number vs. $\Delta z$ when the parallel length scale is $5.0\lambda_{\perp}$ . . . . .	99
Figure 4.48 Dual lattice number vs. $\Delta z$ when the parallel length scale is $10.0\lambda_{\perp}$ . . . . .	100

Figure 4.49 Dual lattice number vs. $\Delta z$ when the parallel length scale is 20.0 $\lambda_{\perp}$ . . . . .	101
Figure 4.50 Dual lattice number vs. $\Delta z$ when the perpendicular length scale is 2.0 $\lambda_{\perp}$ . . . . .	103
Figure 4.51 Dual lattice number vs. $\Delta z$ when the perpendicular length scale is 5.0 $\lambda_{\perp}$ . . . . .	104
Figure 4.52 Dual lattice number vs. $\Delta z$ when the perpendicular length scale is 10.0 $\lambda_{\perp}$ . . . . .	105
Figure 4.53 Dual lattice number vs. $\Delta z$ when the perpendicular length scale is 20.0 $\lambda_{\perp}$ . . . . .	106
Figure 4.54 Dual lattice number vs. $\Delta z$ when the perpendicular length scale is 40.0 $\lambda_{\perp}$ . . . . .	107
Figure 4.55 The longer principal component vs. $\Delta z$ for a pure slab field, starting with random initial positions in $z$ . . . . .	109
Figure 4.56 The longer principal component vs. $\Delta z$ when the energy ratio between the slab and 2D turbulence is 99:1. . . . .	109
Figure 4.57 The longer principal component vs. $\Delta z$ when the energy ratio between the slab and 2D turbulence is 90:10. . . . .	110
Figure 4.58 The longer principal component vs. $\Delta z$ when the energy ratio between the slab and 2D turbulence is 50:50. . . . .	110
Figure 4.59 The longer principal component vs. $\Delta z$ when the energy ratio between the slab and 2D turbulence is 20:80. . . . .	111
Figure 4.60 Ratio of principal components vs. $\Delta z$ for a pure slab field, starting with random initial positions in $z$ . . . . .	114

Figure 4.61 Ratio of principal components vs. $\Delta z$ when the energy ratio between the slab and 2D turbulence is 99:1. ....	114
Figure 4.62 Ratio of principal components vs. $\Delta z$ when the energy ratio between the slab and 2D turbulence is 90:10. ....	115
Figure 4.63 Ratio of principal components vs. $\Delta z$ when the energy ratio between the slab and 2D turbulence is 50:50. ....	115
Figure 4.64 Ratio of principal components vs. $\Delta z$ when the energy ratio between the slab and 2D turbulence is 20:80. ....	116



สถาบันวิทยบริการ  
จุฬาลงกรณ์มหาวิทยาลัย

# CHAPTER I

## INTRODUCTION

### 1.1 Introduction

The Sun is the nearest star to the Earth. Sometimes it has strong activity, such as the solar flares or the coronal mass ejections. This activity can produce the solar energetic particles (SEPs). The SEPs are mostly charged particles, so their trajectories follow the magnetic field lines from the Sun. The interplanetary magnetic field lines are dragged out of the Sun by the supersonic stream of ions flowing out from the Sun called the solar wind. Because the solar wind is very strongly turbulent, the magnetic field lines from the Sun are turbulent, too.

There are two reports about the solar energetic particles from an impulsive solar flare which seem contradictory. Mazur et al. (2000) reported that the flux particles near the Earth exhibits dropouts (to be explained in detail in §2.1.3). The dropouts imply that the SEPs experience little perpendicular diffusion. On the other hand, McKibben et al. (2001) reported the data from two spacecraft which were at different sides and latitudes from the Sun. The data from the two spacecraft showed the same characteristics of the flux intensity vs. time. That means the SEPs propagated throughout space with high diffusion. In the year 2003, by using the two-component model of the magnetic fluctuations, Ruffolo et al. (2003) explained the paradox of dropouts. They confirmed that there is small scale topology in the solar wind called magnetic islands. The SEPs can be trapped by the magnetic islands for a while before spreading throughout space.

In this work, we develop and use various statistical methods, i.e., the Box-Counting Method, the Anisotropy Method, the Dual Lattice Method, and the Principal Component Method to explain the behavior of the magnetic field lines in the turbulent field. We also vary some parameters such as the energy ratio between the slab turbulence and the 2D turbulence, the energy ratio between the fluctuations and the mean field, the size of the initial circle of the magnetic field lines, and the parallel and the perpendicular length scales, to study their effects on the magnetic field lines.

## 1.2 Objectives

- To develop the numerical methods to analyze the behavior of the magnetic field lines in the turbulent field.
- To explain the behavior of the magnetic field lines in the turbulent field as a function of various parameters.

## 1.3 Outline

This thesis contains 5 chapters. CHAPTER I introduces the motivations, the objectives, and the outline of this work. CHAPTER II provides the background knowledge about the interplanetary magnetic field, the transport of SEPs, and the model and simulation of the magnetic turbulence. CHAPTER III provides the methods for analyzing data of the magnetic field lines in the turbulent field. In CHAPTER IV, the results from the analytical methods are shown and discussed. CHAPTER V provides the summary of this work.



# CHAPTER II

## THEORETICAL BACKGROUND

This chapter presents some background knowledge and motivation of this work. First, I would like to introduce the nearest star, our Sun, and its effects on the Earth. Then, I will examine characteristics of the magnetic field in interplanetary space between the Sun and the Earth. Next, I will introduce the phenomenon called “dropouts,” which motivates us to study the nature of groups of particles and magnetic field lines from the Sun. Finally, I will show the model of magnetic turbulence used in this work.

### 2.1 The Sun and Interplanetary Magnetic Field

#### 2.1.1 Solar Activity

Solar activity is related to sunspots. The sunspots are areas on the surface of the Sun which have a concentrated magnetic field. The concentrated magnetic field can inhibit convection flows beneath the surface of the Sun. Therefore, the sunspots have a lower temperature and less brightness than the surrounding area. The magnetic field lines over the sunspots have elasticity. Because of rotation of the Sun and photospheric flows, the magnetic field lines can sometimes twist like rubber bands. When they untwist, they will change the elastic potential to be light, thermal energy and kinetic energy, and release these kinds of energy in the form of solar flares and coronal mass ejections (CMEs). These sudden events are called solar activity, or solar storms.

Some solar activity can affect our Earth. The strong events can produce interplanetary shocks and high energy particles called “solar energetic particles”

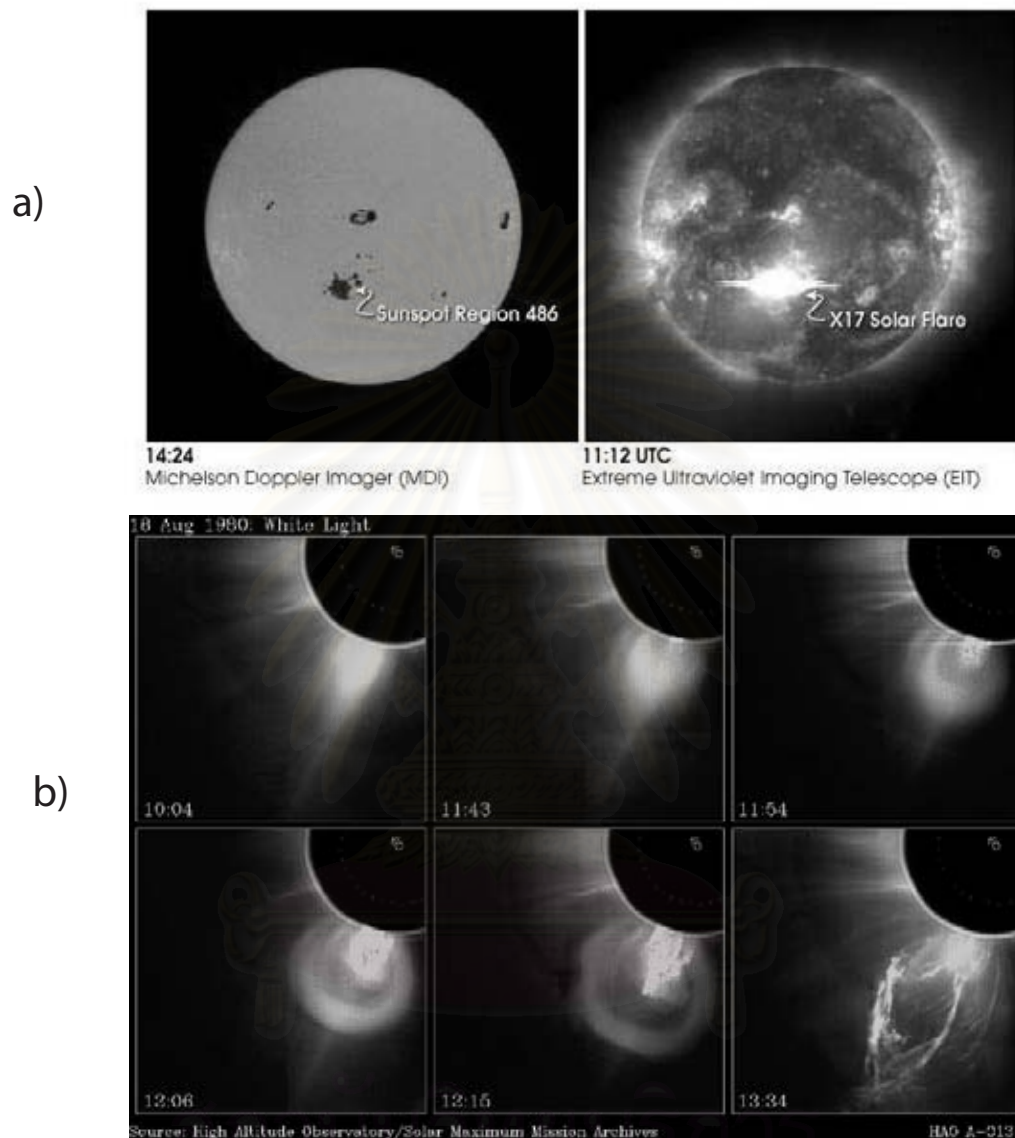


Figure 2.1: a) Groups of sunspots and location of a major flare that occurred on October 28<sup>th</sup>, 2003. The picture on the left was taken in white light, and shows the active region (sunspot group) that caused the flare. The picture on the right was taken in extreme ultraviolet light, showing the flare. b) A coronal mass ejection, which occurred on August 18<sup>th</sup>, 1980. This picture was taken in white light by blocking the Sun, shading the strong sunlight. (Picture credits: a) [http://earthobservatory.nasa.gov/Newsroom/NewImages/images.php3?img\\_id=16345](http://earthobservatory.nasa.gov/Newsroom/NewImages/images.php3?img_id=16345) b) P. Charbonneau and O. R. White)

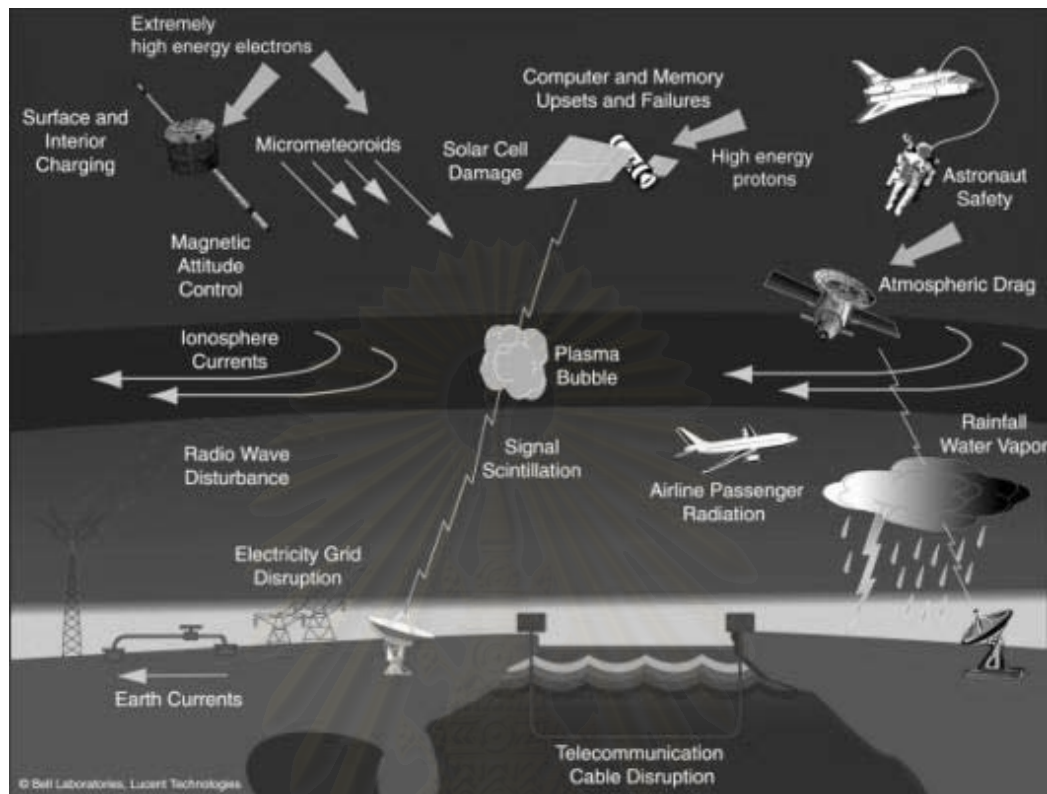


Figure 2.2: Effect of solar energetic particles and interplanetary shocks to the Earth. (Picture credit: L. J. Lanzerotti)

or SEPs. When SEPs hit the solar cell panels or electronic parts of a spacecraft, they can damage these instruments. The SEPs are also a hazard to astronauts if they are not in a protected area. As the shock pushes on the magnetosphere, trapped particles in the Earth's radiation belts can transfer energy to the atmospheric molecules. This causes these molecules to release light in the sky, known as an "aurora."

When an interplanetary shock comes to Earth, it can compress the natural magnetic field around the Earth. The changing magnetic field can produce electric currents in some objects, e.g., electric transformers or pipelines. This electric current can damage those objects and cause some problems. For example,

the damage of electric transformers in electric power plants can cause electricity failures, as in Canada on March 13<sup>th</sup>, 1989, or the damage of pipelines to transfer oil can lead to oil leaks.

### 2.1.2 Interplanetary Magnetic Field

Because the corona of the Sun has a very high temperature of  $\sim 10^6$  K, the plasma of the corona forms an outgoing flow. This stream of plasma is called the “solar wind.” The solar wind flows out of the Sun in all directions with an average speed of about 400 km/s at 1 AU. However, the solar wind has a very low density, with only about 10 particles per  $\text{cm}^3$  on average, compared with the density of the Earth’s atmosphere,  $\sim 10^{23}$  molecules per  $\text{cm}^3$  (Foukal 1989). From these properties of the solar wind, we can infer that the solar wind’s flow is strongly turbulent. The turbulence phenomenon will be explained more in §2.2.

The interplanetary magnetic field or IMF is dragged out from the Sun by the solar wind. The shape of the interplanetary magnetic field is an Archimedean spiral because of the rotation of the Sun. As we know, the solar wind has strong turbulence, which makes the IMF strongly turbulent also. We would like to know about characteristics of the IMF because SEPs, which are mostly charged particles, will follow the IMF.

### 2.1.3 Paradox of Dropouts

In the year 2000, there was a report about particles from impulsive solar flares detected by the *Advanced Composition Explorer (ACE)* spacecraft (Mazur et al. 2000), which was launched on August 25<sup>th</sup>, 1997 by NASA. This report from Mazur et al. showed that near the Earth, the group of SEPs at low energy exhibits dropouts. Dropouts are a phenomenon where the particles’ flux appears,

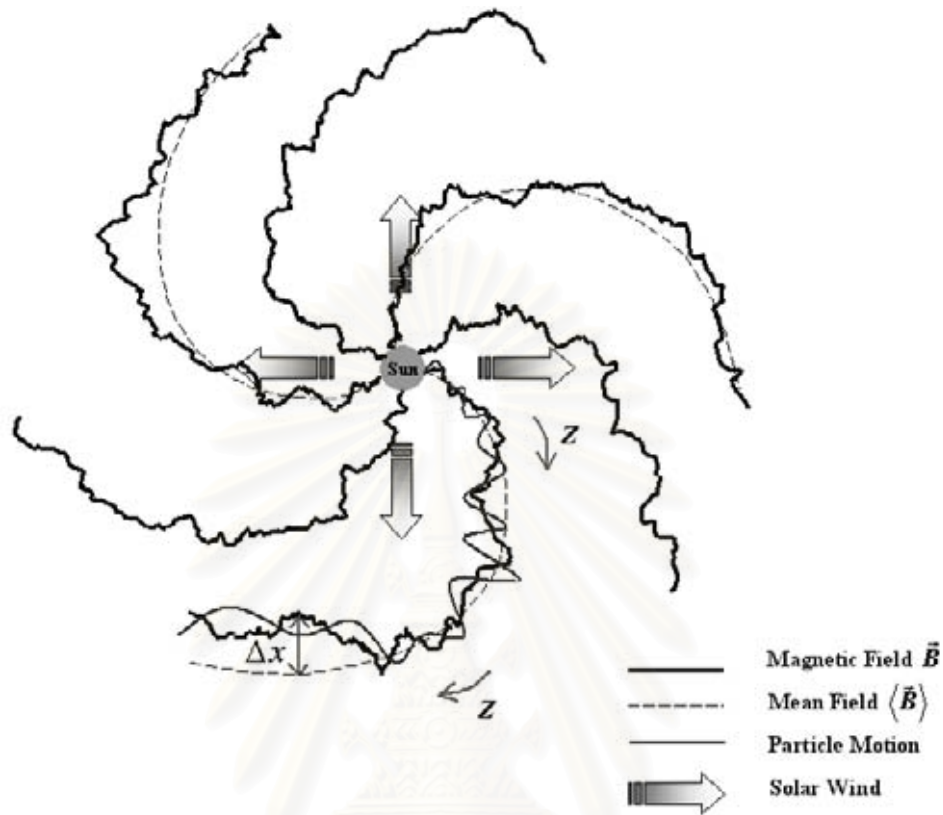


Figure 2.3: The structure of solar wind, the interplanetary magnetic field and the trajectory of high energy particles along the interplanetary magnetic field. (Picture credit: Chuychai 2005)

disappears and reappears again. That means the flux of low-energy SEPs is highly irregular and has little diffusion in some areas (Fig. 2.4).

However, in the year 2001, there was another report about SEP propagation (McKibben et al. 2001). This paper used data from two spacecraft, *Ulysses*, launched by NASA on October 6<sup>th</sup>, 1990, and *IMP-8*, launched by NASA on October 26<sup>th</sup>, 1973, which were located at opposite sides of the Sun and different solar latitudes at the time of the observations (Fig. 2.5). The data show that characteristics of flux of SEPs versus time detected by both spacecraft looks the



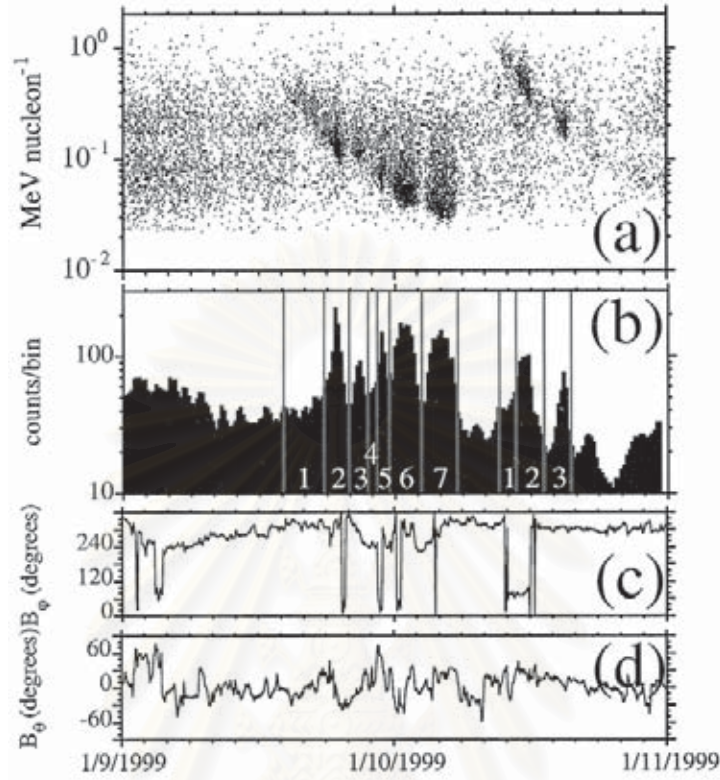


Figure 2.4: Data of two impulsive solar flares occurring on January 9<sup>th</sup> – 10<sup>th</sup>, 1999 as detected by the ULEIS instrument on the *ACE* spacecraft. (a) Scatter plot of energy of H-Fe ions in MeV per nucleon versus arrival time at 1 AU. (b) H-Fe counts versus time in  $\sim 14$  minute bins. The vertical lines show dropout features. (c) Interplanetary magnetic field angle in the geocentric solar ecliptic (GSE)  $x$ - $y$  plane. (d) Interplanetary magnetic field angle normal to the GSE  $x$ - $y$  plane. We see that dropouts do not correspond to IMF discontinuities. (Picture credit: Mazur et al. 2000)

same. That means the propagation of SEPs is smooth and highly diffusive (Fig. 2.6).

The two reports appear contradictory. The report from McKibben et al. (2001) implies such rapid diffusion of the magnetic field lines that dropout would not exist, whereas Giacalone et al. (2000) neglects diffusion altogether and propose that the convection at the surface of the Sun lead to a field line random



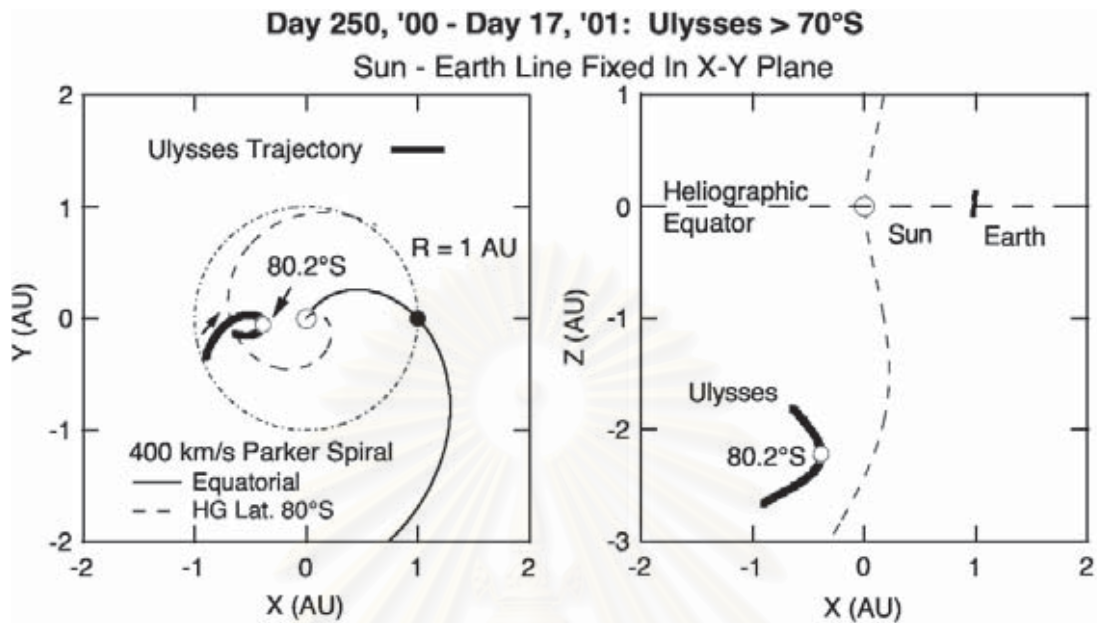


Figure 2.5: Locations of *Ulysses* during Day 250, 2000 to Day 17, 2001 compared with the Sun, Earth, and equatorial plane. (Picture credit: McKibben et al. 2001)

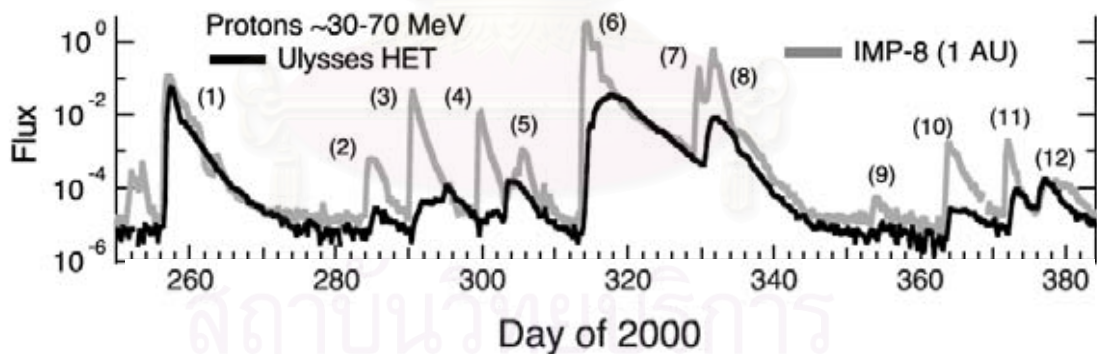


Figure 2.6: Plot between the flux of  $\sim 30 - 70$  MeV of solar energetic protons versus time (six hour averages) during Day 250, 2000 to Day 17, 2001. The black line traces data from the *Ulysses* spacecraft and the light line traces data from the *IMP-8* spacecraft. (Picture credit: McKibben et al. 2001)

walk that is consistent with dropouts. Therefore, we cannot use the perpendicular transport, which is the transport of the energetic particles perpendicular to the mean magnetic field, of a diffusive nature to explain both observations.

However, in the year 2003, there was work that showed that if we use the two-component model of magnetic fluctuations (to be explained in detail in §2.2), we can explain the paradox of dropouts of the magnetic field lines' flux (Ruffolo, Matthaeus and Chuychai 2003). By using the two-component magnetic fluctuation model, we can consider that the SEPs are trapped in some regions, which may be called the “magnetic islands”, for a while before diffusing to all space (Fig. 2.7).

Ruffolo et al. (2003) propose that dropouts occur from SEPs trapped in topological structures which developed in the solar wind, not at the surface of the Sun. Thus, SEPs can rapidly diffuse after escaping from topological traps, in agreement with McKibben et al. (2001). For another class of solar events, e.g., gradual flares or CMEs, SEPs are injected from a much wider region on the surface of the Sun than the magnetic islands, so the dropout phenomena cannot occur, in agreement with Mazur et al. (2000) and Giacalone et al. (2000).

## 2.2 Model of the Magnetic Turbulence

### 2.2.1 Turbulence in Nature

Turbulence is a type of fluid flow that is unsteady, irregular, seemingly random and chaotic, and surely the motion of every eddy or droplet is unpredictable (Pope 2000). We can see turbulent flows in everyday life, such as smoke from a car's exhaust pipe, clouds on the sky, or milk stirred into coffee. These are some characteristics of turbulent flows (Tennekes and Lumley 1994):

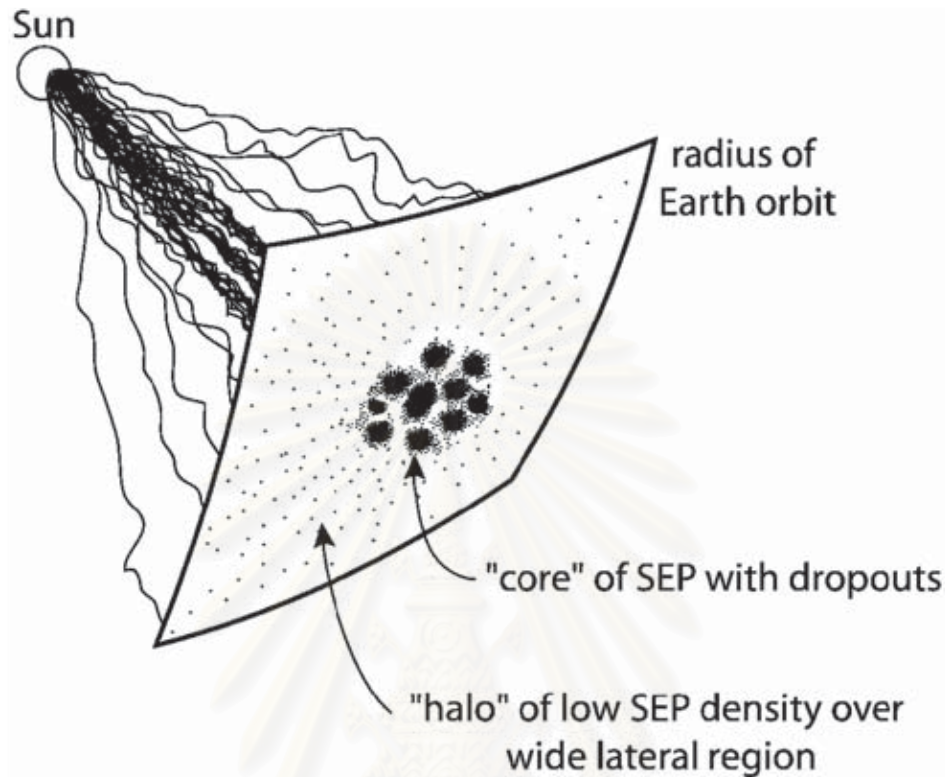


Figure 2.7: Illustration of interplanetary magnetic field lines populated with solar energetic particles from a localized source region near the Sun, as expected for an impulsive solar flare. At the radius of Earth orbit, some magnetic field lines are trapped in some regions of the “core” while other magnetic field lines are spread out widely in the “halo” region. (Picture credit: Ruffolo et al. 2003)

- **Irregularity** or randomness. Irregularity implies that we can determine turbulent motions only by statistical methods.
- **Diffusivity.** Diffusivity is another important feature of turbulent flows. If a flow pattern looks random but does not exhibit spreading of velocity fluctuations through the surrounding fluid, it is surely not turbulent.
- **Large Reynolds numbers.** The dimensionless Reynolds number of a flow

is defined as

$$Re = \frac{\mathcal{U}\mathcal{L}}{\nu}, \quad (2.1)$$

where

$Re$  is the Reynolds number,

$\mathcal{U}$  is the characteristic velocity of the flow,

$\mathcal{L}$  is a length scale of the flow, and

$\nu$  is the kinematic viscosity of the fluid.

Normally, a laminar flow, which is steady, will become a turbulent flow when its Reynolds number increases more than a critical value, typically of order  $10^3$ . For the solar wind, the Reynolds number is  $10^{12}$ . Thus, the solar wind is strongly turbulent.

- **Three-dimensional vorticity fluctuations.** Turbulence is characterized by high levels of fluctuating vorticity, which may be called “eddies.” However, the random vorticity fluctuations could not maintain themselves if the velocity fluctuations were two dimensional. Thus, the turbulence must have three-dimensional vorticity fluctuations.
- **Dissipation.** Turbulent flows are always dissipative. Turbulence is composed of eddies of different sizes. Normally the large eddies are unstable and break up. They will transfer their energy to smaller eddies. These smaller eddies are also unstable, break up, and transfer energy to even smaller eddies. This is called an energy cascade. The energy cascade will continue until the Reynolds number of an eddy is small enough to make the eddy motion stable, and the viscosity dissipates the kinetic energy most effectively. Because of energy dissipation, we have to put energy into the turbulent system all the time to maintain the turbulence.

## 2.2.2 Turbulence in the Interplanetary Magnetic Field

In this work, the model of the magnetic field is

$$\vec{B} = B_0 \hat{z} + \vec{b}(x, y, z), \quad (2.2)$$

where

$\vec{B}$  is the total magnetic field,

$B_0 \hat{z}$  is the mean magnetic field, and

$\vec{b}(x, y, z)$  is the fluctuation of the magnetic field.

The direction of the magnetic fluctuation is always perpendicular to the mean field, so  $\vec{b} \perp \hat{z}$ . Note that the  $z$  direction is the direction along the mean magnetic field and that  $x$  and  $y$  are the directions perpendicular to the mean magnetic field.

We can separate the fluctuation of the magnetic field into two parts. One part depends on only  $z$ , called “slab” fluctuations or slab turbulence. The other part depends on  $x$  and  $y$ , called “2D” fluctuations or 2D turbulence. This idea was first introduced by Matthaeus, Goldstein, and Roberts (1990), motivated by the observation that solar wind fluctuations are concentrated at nearly parallel and nearly perpendicular wave numbers. The model has provided a useful description of solar wind turbulence and particle transport (Bieber et al. 1994, 2004).

Now, the fluctuation of the magnetic field becomes

$$\vec{b}(x, y, z) = \vec{b}^{slab}(z) + \vec{b}^{2D}(x, y), \quad (2.3)$$

so

$$\vec{B} = B_0 \hat{z} + \vec{b}^{slab}(z) + \vec{b}^{2D}(x, y). \quad (2.4)$$

For slab turbulence, from the definition,  $\vec{b}^{slab}$  will have a constant same magnitude and direction in  $x$ - $y$  plane in each  $z$ . Furthermore, if we trace the

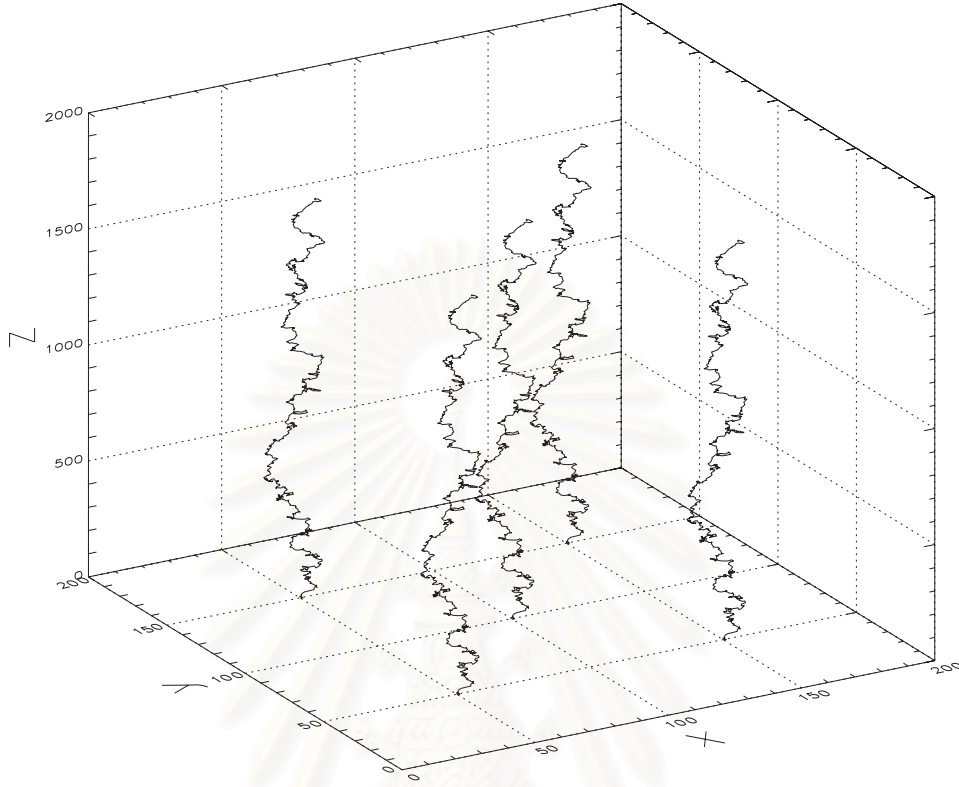


Figure 2.8: Trace of five magnetic field lines in pure slab field with varied initial positions. Because  $\vec{b}^{slab}$  depends on only  $z$ , all magnetic field lines undergo the same random walk in  $x(z)$  and  $y(z)$ .

magnetic field lines in pure slab field, all of magnetic field lines will look the same with each other by not depending on the initial position (Fig. 2.8).

Considering the 2D turbulence, from Maxwell's equation we know that

$$\vec{\nabla} \cdot \vec{B} = 0. \quad (2.5)$$

By putting equation (2.4) in equation (2.5), we will get that

$$\vec{\nabla} \cdot B_0 \hat{z} + \vec{\nabla} \cdot \vec{b}^{slab}(z) + \vec{\nabla} \cdot \vec{b}^{2D}(x, y) = 0. \quad (2.6)$$

Because  $B_0 \hat{z}$  does not depend on position and  $\vec{b}^{slab}(z)$  depends on  $z$  but has only



$x$  and  $y$  components, that means

$$\vec{\nabla} \cdot B_0 \hat{z} = 0, \quad (2.7)$$

and

$$\vec{\nabla} \cdot \vec{b}^{slab}(z) = \frac{\partial b_x^{slab}}{\partial x} + \frac{\partial b_y^{slab}}{\partial y} = 0. \quad (2.8)$$

Therefore, equation (2.6) will reduce to

$$\vec{\nabla} \cdot \vec{b}^{2D}(x, y) = 0. \quad (2.9)$$

If we assign  $a(x, y)\hat{z}$  as the vector potential for the 2D component,

$$\vec{b}^{2D}(x, y) = \vec{\nabla} \times [a(x, y)\hat{z}] \quad (2.10)$$

automatically satisfies eq. (2.9). We call  $a(x, y)$  the potential function (Fig. 2.9).

If we plot contours of constant  $a(x, y)$ , the magnetic field lines must follow those contours (Fig. 2.10).

The model of slab+2D turbulence can explain the dropouts of particles from impulsive solar flares in terms of filamentary magnetic connection to the particle source regions as we discussed in a previous section (Ruffolo, Matthaeus and Chuychai 2003). First, we have to define the areas near relative maxima or minima of  $a(x, y)$  as O-points and areas near saddle points of  $a(x, y)$  as X-points. Ruffolo, Matthaeus and Chuychai (2003) show that, out to Earth orbit, the magnetic field lines will be trapped at the regions near O-points while the magnetic field lines near X-points can spread out through space (see also Fig. 2.7). By using the idea that SEPs normally follow the magnetic field lines, we can explain the dropout observations. When a spacecraft passes a region near an O-point, it will detect a high intensity of particles, but when it passes a region

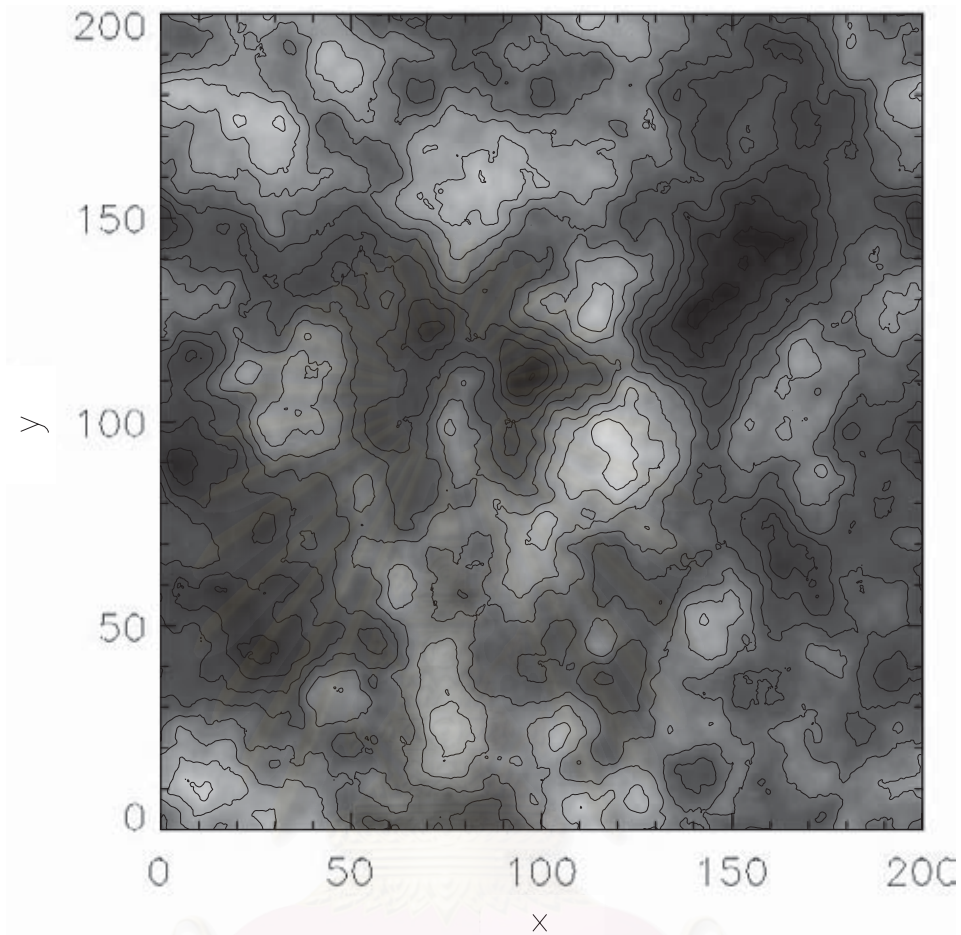


Figure 2.9: Contour plot of the potential function  $a(x, y)$ . Light areas are the local maxima and dark areas are the local minima.

near an X-point, it will detect a low intensity of particles. On the other hand, far beyond Earth orbit, all of the magnetic field lines can spread all over space. Then, we will not be able to detect dropouts there.

### 2.2.3 Diffusion Coefficient

The first calculation of the diffusion coefficient of the magnetic field line random walk in slab+2D turbulence was presented by Matthaeus et al.

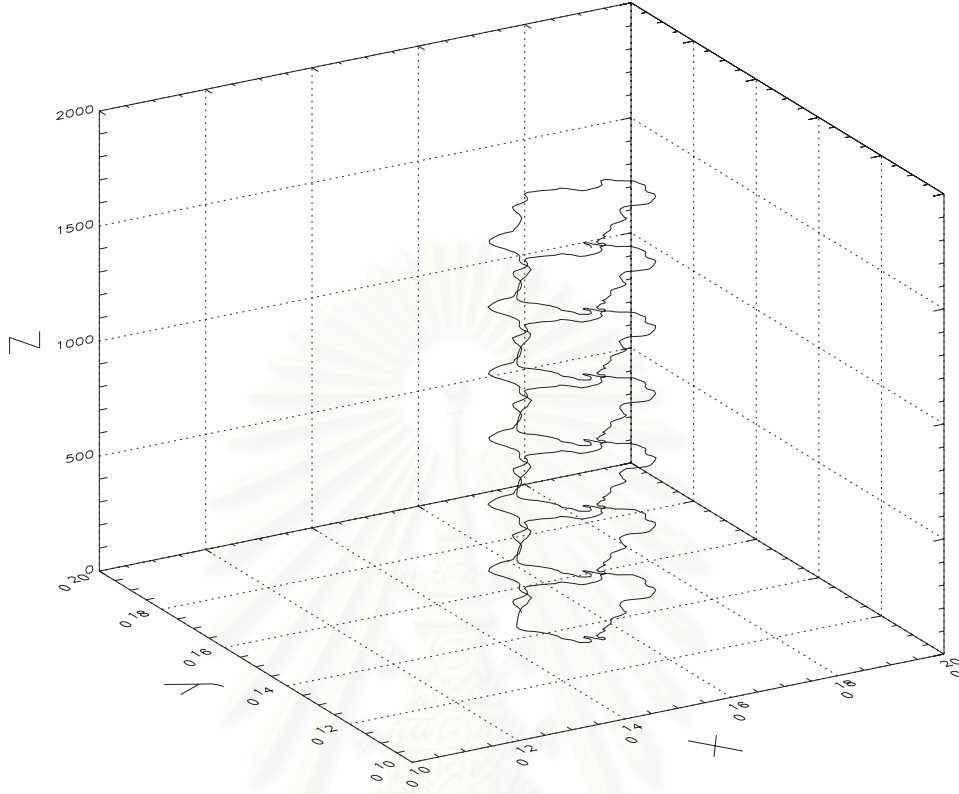


Figure 2.10: Trace of a magnetic field line in pure 2D turbulence. This trace uses the potential function shown in Fig. 2.9. If we project the magnetic field line into  $x$ - $y$  plane, it follows a contour of constant  $a(x, y)$ .

(1995). They showed that the total diffusion coefficient ( $D_{\perp}$ ), defined as  $D_{\perp} = \langle (\Delta x)^2 \rangle / 2\Delta z$ , is not simply the sum of the diffusion coefficients of the slab component ( $D_{slab}$ ) and the 2D component ( $D_{2D}$ ). By comparing with hydrodynamics, we can expect the diffusion coefficient of the field line random walk in magnetic turbulence to be  $D_{\perp} \approx \tilde{\lambda}\delta b/B_0$ , where  $\tilde{\lambda}$  is the appropriate length scale (Matthaeus et al. 1995; Ruffolo et al. 2004).

We start with the definition of a magnetic field line. A magnetic field line is tangent everywhere to the magnetic field. Thus,

$$d\vec{l} \times \vec{B} = 0, \quad (2.11)$$

where  $d\vec{l}$  is an arc length,  $d\vec{l} = \hat{i}dx + \hat{j}dy + \hat{k}dz$ . From equation (2.11), the equation of a magnetic line should be (Ruffolo, Matthaeus and Chuychai 2004)

$$\frac{dx}{B_x} = \frac{dy}{B_y} = \frac{dz}{B_z}. \quad (2.12)$$

In our work, the model of magnetic field is  $\vec{B} = B_0\hat{z} + b_x\hat{x} + b_y\hat{y}$ , the equation (2.12) becomes

$$\frac{dx}{b_x} = \frac{dy}{b_y} = \frac{dz}{B_0}. \quad (2.13)$$

We can use equation (2.13) to calculate the perpendicular displacements,  $\Delta x$  and  $\Delta y$ , over a distance  $\Delta z$  along the mean magnetic field  $B_0$  (Fig. 2.11):

$$\Delta x \equiv x(\Delta z) - x(0) = \frac{1}{B_0} \int_0^{\Delta z} b_x[x(z'), y(z'), z'] dz', \quad (2.14)$$

$$\Delta y \equiv y(\Delta z) - y(0) = \frac{1}{B_0} \int_0^{\Delta z} b_y[x(z'), y(z'), z'] dz'. \quad (2.15)$$

Then, the ensemble average of  $(\Delta x)^2$  is given by

$$\begin{aligned} \langle (\Delta x)^2 \rangle &= \frac{1}{B_0^2} \int_0^{\Delta z} \int_0^{\Delta z} \langle b_x[x(z'), y(z'), z'] b_x[x(z''), y(z''), z''] \rangle dz' dz'' \\ &= \frac{1}{B_0^2} \int_0^{\Delta z} \int_0^{\Delta z} \langle b_x(x', y', z') b_x(x'', y'', z'') \rangle dz' dz'', \end{aligned} \quad (2.16)$$

where we use the notation  $x'$  for  $x(z')$ , etc., and for  $(\Delta y)^2$  this is

$$\langle (\Delta y)^2 \rangle = \frac{1}{B_0^2} \int_0^{\Delta z} \int_0^{\Delta z} \langle b_y(x', y', z') b_y(x'', y'', z'') \rangle dz' dz''. \quad (2.17)$$

If we define  $\Delta x' \equiv x'' - x'$ ,  $\Delta y' \equiv y'' - y'$  and  $\Delta z' \equiv z'' - z'$  (Fig. 2.12), and assume the magnetic turbulence is statistically homogeneous, we can write equations (2.16) and (2.17) as

$$\langle (\Delta x)^2 \rangle = \frac{1}{B_0^2} \int_0^{\Delta z} \int_{-z'}^{\Delta z - z'} \langle b_x(0, 0, 0) b_x(\Delta x', \Delta y', \Delta z') \rangle d\Delta z' dz', \quad (2.18)$$

$$\langle (\Delta y)^2 \rangle = \frac{1}{B_0^2} \int_0^{\Delta z} \int_{-z'}^{\Delta z - z'} \langle b_y(0, 0, 0) b_y(\Delta x', \Delta y', \Delta z') \rangle d\Delta z' dz'. \quad (2.19)$$

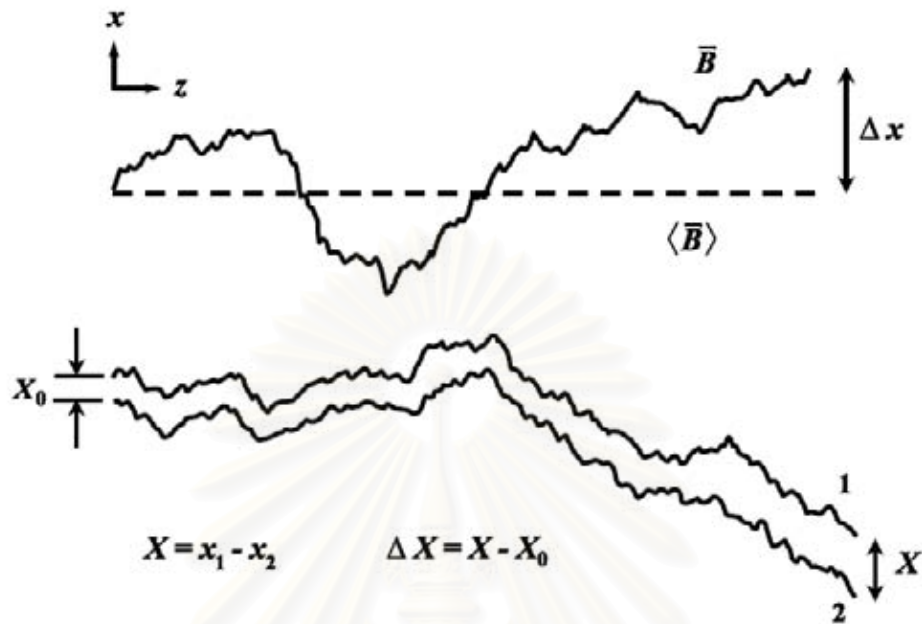


Figure 2.11: Illustration of the magnetic field line random walk perpendicular to the mean field ( $\Delta x$ ), displacement between nearby field lines ( $X \equiv x_2 - x_1$ ), and their separation ( $\Delta X \equiv X - X_0$ ). (Picture credit: Ruffolo et al. 2004)

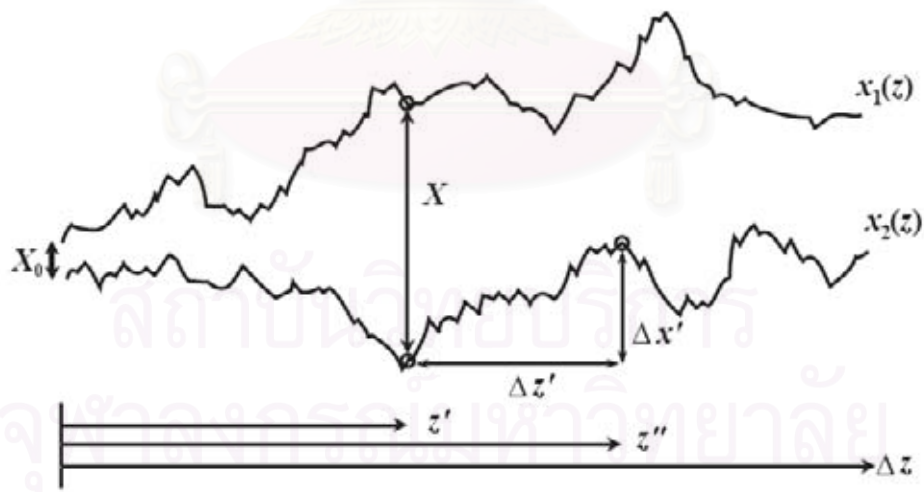


Figure 2.12: Schematic of two random field lines and definitions of various quantities. (Picture credit: Ruffolo et al. 2004)

In general, for a homogeneous turbulent field, we can define the perpendicular diffusion coefficient of the magnetic field lines as (Matthaeus et al. 1995)

$$D_{\perp} = \frac{\langle (\Delta \vec{x}_{\perp})^2 \rangle}{4\Delta z}, \quad (2.20)$$

where  $\Delta \vec{x}_{\perp}$  is the perpendicular displacement. Assuming the turbulence is axisymmetric, that is  $\langle (\Delta x)^2 \rangle = \langle (\Delta y)^2 \rangle$ , equation (2.20) becomes

$$D_{\perp} = \frac{\langle (\Delta x)^2 \rangle}{2\Delta z}. \quad (2.21)$$

If we substitute equation (2.18) into equation (2.21), we will get the diffusion coefficient of a magnetic field line.

However, the integrand in equation (2.18) is in Lagrangian form, which is in an ensemble average over representations of the magnetic turbulence, which the positions themselves depend on the representation. We can use Corrsin's hypothesis (Corrsin 1959) to separate the statistics of the magnetic fluctuations out of the probability. Thus, equation (2.18) becomes (Ruffolo et al. 2004)

$$\begin{aligned} & \langle b_x(0, 0, 0)b_x(\Delta x'(\Delta z'), \Delta y'(\Delta z'), \Delta z') \rangle \\ &= \int_{-\infty}^{\infty} \int_{-\infty}^{\infty} R_{xx}(\Delta x', \Delta y', \Delta z') P(\Delta x'|\Delta z') P(\Delta y'|\Delta z') d\Delta x' d\Delta y', \end{aligned} \quad (2.22)$$

where  $R_{xx}(\Delta x', \Delta y', \Delta z') = \langle b_x(0, 0, 0)b_x(\Delta x', \Delta y', \Delta z') \rangle$  is the correlation function in standard (Eulerian) form, and  $P(\Delta x'|\Delta z')$  and  $P(\Delta y'|\Delta z')$  are probability functions. The Fourier transform of that correlation function is the power spectrum,

$$P_{ij}(\vec{k}) = \frac{1}{(\sqrt{2\pi})^3} \int_{-\infty}^{\infty} R_{ij}(\vec{r}) e^{i\vec{k}\cdot\vec{r}} d\vec{r}. \quad (2.23)$$

This hypothesis works when the two positions are displaced by more than a coherence length in the parallel or perpendicular direction. Then, we assume



that the distributions of probabilities  $P(\Delta x'|\Delta z')$  and  $P(\Delta y'|\Delta z')$  are Gaussian distributions,

$$\begin{aligned} P(\Delta x'|\Delta z') &= \frac{1}{\sqrt{2\pi\sigma_x^2}} \exp\left[-\frac{(\Delta x')^2}{2\sigma_x^2}\right], \\ P(\Delta y'|\Delta z') &= \frac{1}{\sqrt{2\pi\sigma_y^2}} \exp\left[-\frac{(\Delta y')^2}{2\sigma_y^2}\right]. \end{aligned} \quad (2.24)$$

Finally, we assume the variances  $\sigma_x^2 = \langle(\Delta x)^2\rangle$  and  $\sigma_y^2 = \langle(\Delta y)^2\rangle$  are diffusive and statistically axisymmetric, that is

$$\langle(\Delta x)^2\rangle = \langle(\Delta y)^2\rangle = 2D_{\perp}|\Delta z'|. \quad (2.25)$$

Because slab and 2D fluctuations are orthogonal under the ensemble average, we can calculate diffusion coefficients in both slab and 2D terms. For the slab term, for the limit  $\Delta z \rightarrow \infty$ , the diffusion coefficient is

$$\begin{aligned} \frac{\langle(\Delta x)^2\rangle^{slab}}{2\Delta z} &\rightarrow \frac{1}{\sqrt{2\pi}B_0^2} \int_{-\infty}^{\infty} \pi\delta(k_z)P_{xx}^{slab}(k_z)dk_z \\ &= \sqrt{\frac{\pi}{2}} \frac{P_{xx}(0)}{B_0^2} \equiv D_{slab}. \end{aligned} \quad (2.26)$$

For  $k_z \ll k_{0z}$ , where  $k_{0z}$  is a wave number related to the outer scale ( $\ell_0$ ),  $P_{xx}^{slab}$  is roughly constant. The outer scale will be explained in detail in § 2.3. We can write the diffusion coefficient of the slab field as

$$D_{\perp}^{slab} = \frac{\langle b_x^{slab} \rangle}{B_0^2} \ell_c, \quad (2.27)$$

where  $\ell_c$  is the slab correlation length defined as

$$\ell_c = \frac{\int_0^{\infty} R_{xx}^{slab}(z)dz}{R_{xx}^{slab}(z=0)}. \quad (2.28)$$

For the 2D term, we have to distinguish the spectrum and random phases of 2D fluctuations (Matthaeus et al. 1995). First, we imagine a box of infinite

extent in the  $z$  direction but finite in the  $x$  and  $y$  directions. Then, use the Fourier transform of the integrand of equation (2.18),

$$\langle \vec{b}^{2D}(\vec{x}_\perp(z)) \cdot \vec{b}^{2D}(0) \rangle = \sum_{\vec{k}_\perp} \langle |\vec{b}^{2D}(\vec{k}_\perp)|^2 e^{i\vec{k}_\perp \cdot \vec{x}_\perp(z)} \rangle. \quad (2.29)$$

The amplitude  $|\vec{b}^{2D}(\vec{k}_\perp)|^2$ , with  $\vec{k}_\perp$  satisfying  $\vec{k}_\perp \cdot \hat{z} = 0$ , would become the power spectrum after ensemble averaging. By using Corrsin's hypothesis, we can separate equation (2.29) to

$$\langle |\vec{b}^{2D}(\vec{k}_\perp)|^2 e^{i\vec{k}_\perp \cdot \vec{x}_\perp(z)} \rangle = \langle |\vec{b}^{2D}(\vec{k}_\perp)|^2 \rangle \langle e^{i\vec{k}_\perp \cdot \vec{x}_\perp(z)} \rangle. \quad (2.30)$$

Considering the term  $\langle e^{i\vec{k}_\perp \cdot \vec{x}_\perp(z)} \rangle$ , if we assume that  $x(z)$  and  $y(z)$  are identically Gaussian distributions and are uncorrelated, by expansion of the exponential and the definition of the diffusion coefficient, this term becomes

$$\langle e^{i\vec{k}_\perp \cdot \vec{x}_\perp(z)} \rangle = e^{-k_\perp^2 D_\perp z}. \quad (2.31)$$

By substituting equations (2.29), (2.30) and (2.31) into equation (2.18), the diffusion coefficient will be

$$\begin{aligned} \frac{\langle (\Delta x)^2 \rangle^{2D}}{2\Delta z} &= \frac{1}{2} \sum_{\vec{k}_\perp} \frac{\langle |\vec{b}^{2D}(\vec{k}_\perp)|^2 \rangle}{B_0^2} \int_0^\infty e^{-k_\perp^2 D_\perp z} dz \\ &= \left( \frac{1}{2} \sum_{\vec{k}_\perp} \frac{\langle |\vec{b}^{2D}(\vec{k}_\perp)|^2 \rangle}{2k_\perp^2 B_0^2} \right) \frac{1}{D_\perp} = \frac{D_{2D}^2}{D_\perp}, \end{aligned} \quad (2.32)$$

where

$$D_{2D} = \left( \sum_{\vec{k}_\perp} \frac{\langle |\vec{b}^{2D}(\vec{k}_\perp)|^2 \rangle}{2k_\perp^2 B_0^2} \right)^{\frac{1}{2}}. \quad (2.33)$$

By comparing with hydrodynamics and equation (2.27), we can write

$$D_{2D} \equiv \frac{\langle b^{2D} \rangle}{B_0} \tilde{\lambda}, \quad (2.34)$$

where  $\tilde{\lambda}$  is the so-called “ultrascale,” defined by the weighting of the spectrum we used. Physically,  $\tilde{\lambda}$  may be related to the largest area or “island” over which the magnetic field lines are typically trapped. Mathematically, we find

$$\tilde{\lambda} \equiv \sqrt{\frac{\langle a^2 \rangle}{\langle b_{2D}^2 \rangle}}. \quad (2.35)$$

In summary,  $D_{\perp}$  is a combination of diffusion coefficients in the pure slab case and pure 2D case,

$$\frac{\langle (\Delta x)^2 \rangle}{2\Delta z} = \frac{\langle (\Delta x)^2 \rangle^{slab}}{2\Delta z} + \frac{\langle (\Delta x)^2 \rangle^{2D}}{2\Delta z}, \quad (2.36)$$

that is

$$D_{\perp} = D_{slab} + \frac{D_{2D}^2}{D_{\perp}}, \quad (2.37)$$

with the general solution

$$D_{\perp} = \frac{D_{slab} + \sqrt{D_{slab}^2 + 4D_{2D}^2}}{2}. \quad (2.38)$$

## 2.3 Simulations of Turbulent Magnetic Fields

### 2.3.1 Energy Cascade and Kolmogorov Spectrum

From the previous section, we know that one of the properties of turbulence is an energy cascade. The idea of the energy cascade was first introduced by Richardson (1922). He stated that turbulence contains eddies in different sizes. The large eddies are not stable. They will break up and transfer their energy to smaller eddies (Fig. 2.13). The rate of energy transfer per unit mass  $\varepsilon$  depends on three variables: the eddy size  $\ell$ , the characteristic velocity  $v(\ell)$  and the timescale  $\tau(\ell) \equiv \ell/v(\ell)$ . The energy transfer rate per unit mass is  $\varepsilon = v^2/\tau = v^3/\ell$ .

The theory about the energy cascade has been further developed by Kolmogorov (1941). He stated three hypotheses motivated by the idea that if  $\ell$

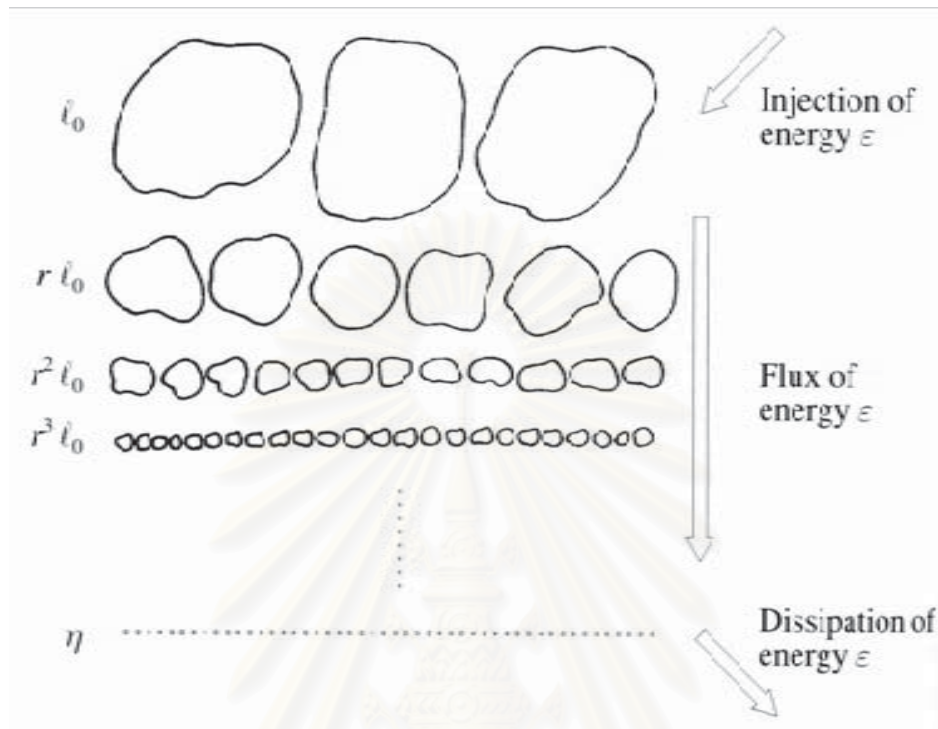


Figure 2.13: Illustration of the Richardson cascade. (Picture credit: [http://www.ipp.mpg.de/~fsj/PAPERS\\_1/tutorial\\_1.pdf](http://www.ipp.mpg.de/~fsj/PAPERS_1/tutorial_1.pdf))

decreases,  $v$  and  $\tau$  will decrease, too. His first hypothesis is the hypothesis of local isotropy: “at sufficiently high Reynolds number, the small-scale turbulent motions ( $\ell \ll l_0$ ) are statistically isotropic.” This hypothesis introduces the length scale  $l_0$  which is the length scale of the largest eddies. This length scale and its related velocity  $v_0$  are called “outer scales.” The range  $\ell > l_0$  is called the “energy-containing range.”

Kolmogorov’s second hypothesis is the first similarity hypothesis: “In every turbulent flow at sufficiently high Reynolds number, the statistics of the small-scale motions ( $\ell < l_0$ ) have a universal form that is uniquely determined by  $\nu$  and  $\varepsilon$ ,” where  $\varepsilon$  is the dissipation rate (or the energy transfer rate per unit

mass in Richardson's theory) and  $\nu$  is the viscosity. With this hypothesis, by dimensional analysis, the smallest eddy length, velocity and timescale can be written only as  $\eta \equiv (\nu^3 \varepsilon)^{1/4}$ ,  $v \equiv (\nu \varepsilon)^{1/4}$  and  $\tau \equiv (\nu/\varepsilon)^{1/2}$ , respectively. These smallest scales are called "inner scales." The range  $\ell < \eta$  is called the dissipation range.

Kolmogorov's final hypothesis is the second similarity hypothesis: "in every turbulent flow at sufficiently high Reynolds number, the statistics of the motions of scale  $\ell$  in the range  $\ell_0 \gg \ell \gg \eta$  have a universal form that is uniquely determined by  $\varepsilon$ , independent of  $\nu$ ." The range  $\ell_0 \gg \ell \gg \eta$  is called the "inertial range."

Consider the spectrum in the inertial range, written as

$$\bar{u}^2 = \int_0^\infty S(k) dk, \quad (2.39)$$

where  $S(k)$  is the spectrum and  $k$  is wave number. Because of Kolmogorov's second similarity hypothesis, by using dimensional analysis, we will get

$$S(k) \propto \varepsilon^{2/3} k^{-5/3}. \quad (2.40)$$

This relation is called "Kolmogorov's law," and a spectrum that obeys this theory is called a "Kolmogorov spectrum." All turbulent phenomena in three dimensions have a Kolmogorov spectrum (Fig. 2.14).

### 2.3.2 Generating Representations of Turbulent Magnetic Fields

Because the turbulent magnetic field is a random function, we cannot specify the function of the magnetic field directly in real space. However, the spectrum of the magnetic turbulence is a Kolmogorov spectrum, so we can generate

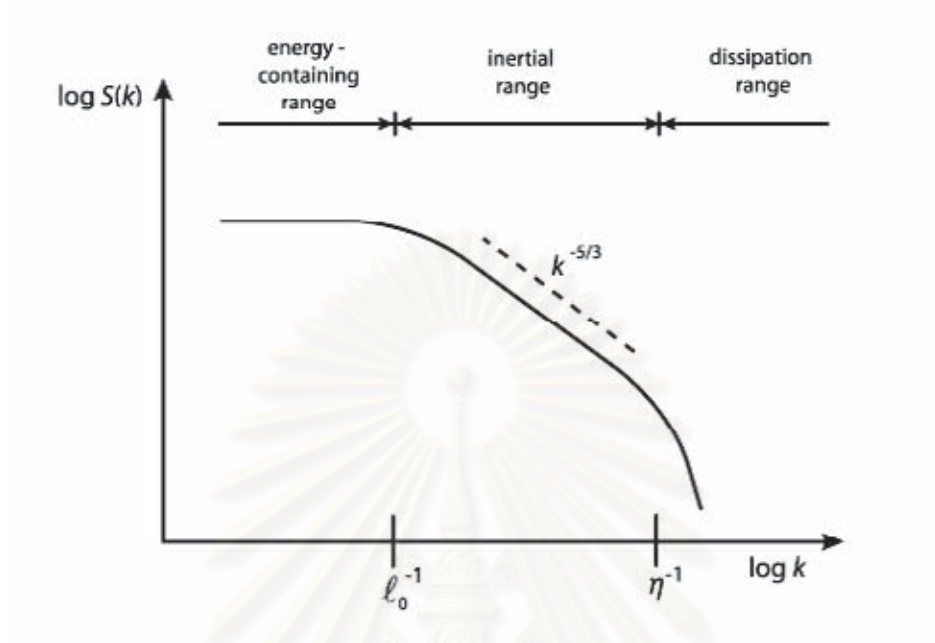


Figure 2.14: The Kolmogorov spectrum. (Picture credit: Chuychai 2005)

the power spectrum of the magnetic field in Fourier space. The omnidirectional power spectrum depends on  $k^{-5/3}$  in the inertial range.

For slab turbulence, we generate the power spectrum for the simulations as (Ruffolo et al. 2004)

$$P_{xx}^{slab}(k_z) = P_{yy}^{slab}(k_z) = \frac{C^{slab}}{[1 + (k_z \ell_z)^2]^{5/6}}, \quad (2.41)$$

where  $C^{slab}$  is a normalization constant and  $\ell_z$  is the parallel coherence length related to correlation length in equation (2.22). Because the power spectrum is the Fourier transform of the magnetic correlation function  $R_{ij} = \langle b_i(0)b_j(\vec{r}) \rangle$ , and  $R_{xx}^{slab}(z=0) = \langle b^2 \rangle$ , the slab fluctuations in  $k_z$  are

$$b_x^{slab}(k_z) = \sqrt{P_{xx}^{slab}(k_z)} e^{i\phi_x(k_z)}, \quad (2.42)$$

$$b_y^{slab}(k_z) = \sqrt{P_{yy}^{slab}(k_z)} e^{i\phi_y(k_z)}, \quad (2.43)$$



where  $i$  is  $\sqrt{-1}$  and  $\phi$  is a random phase for each  $k_z$  varying from  $0 \rightarrow 2\pi$ . Finally, we use the inverse fast Fourier transformation (Press et al. 1992) to transform the magnetic field to real space:

$$b_x^{slab}(z) = \frac{1}{\sqrt{2\pi}} \int_{-\infty}^{\infty} b_x^{slab}(k_z) e^{-ik_z z} dk_z, \quad (2.44)$$

$$b_y^{slab}(z) = \frac{1}{\sqrt{2\pi}} \int_{-\infty}^{\infty} b_y^{slab}(k_z) e^{-ik_z z} dk_z, \quad (2.45)$$

$$\vec{b}^{slab}(z) = b_x^{slab}(z)\hat{x} + b_y^{slab}(z)\hat{y}. \quad (2.46)$$

For 2D fluctuations, we can follow steps as for slab fluctuations. However, instead of using the power spectrum of the magnetic field directly, we will generate the power spectrum of the potential function  $a(x, y)$ . The power spectrum in the simulations is

$$A(k_{\perp}) = \frac{C^{2D}}{[1 + (k_{\perp}\ell_{\perp})^2]^{7/3}}, \quad (2.47)$$

where  $A(k_{\perp})$  is the power spectrum of  $a(x, y)$ ,  $C^{2D}$  is a normalization constant,  $k_{\perp} = \sqrt{k_x^2 + k_y^2}$  and  $\ell_{\perp}$  is the perpendicular coherence length related to  $\tilde{\lambda}$  in equation (2.35). The potential function in Fourier space is

$$a(k_x, k_y) = \sqrt{A(k_{\perp})} e^{i\phi(k_x, k_y)}. \quad (2.48)$$

From  $\vec{b}^{2D}(x, y) = \vec{\nabla} \times a(x, y)\hat{z}$ , in Fourier space, the equation should be

$$\vec{b}^{2D}(k_x, k_y) = -i\vec{k} \times a(k_x, k_y)\hat{z}. \quad (2.49)$$

This ensures that  $\vec{\nabla} \cdot \vec{b}^{2D}(x, y) = 0$ . Finally, use the inverse Fourier transform of  $\vec{b}^{2D}(k_x, k_y)$  to real space

$$b_x^{2D}(x, y) = \frac{1}{2\pi} \int_{-\infty}^{\infty} \int_{-\infty}^{\infty} b_x^{2D}(k_x, k_y) e^{-i(\vec{r} \cdot \vec{k})} dk_x dk_y, \quad (2.50)$$

$$b_y^{2D}(x, y) = \frac{1}{2\pi} \int_{-\infty}^{\infty} \int_{-\infty}^{\infty} b_y^{2D}(k_x, k_y) e^{-i(\vec{r} \cdot \vec{k})} dk_x dk_y. \quad (2.51)$$

In this work, for tracing the magnetic field lines numerically, we use a computer program developed by Mr. Peera Pongkitiwanchkul (Pongkitiwanchkul 2005).



สถาบันวิทยบริการ  
จุฬาลงกรณ์มหาวิทยาลัย

# CHAPTER III

## DATA ANALYSIS METHODS

In this chapter, I would like to present a few ways to analyse our data.

These are:

- **Box-Counting Dimension.** This method is used to find the dimension of an object. In the case of the group of magnetic field lines in the slab+2D field, we may use the dimension of the group of magnetic field lines to consider the length in the  $z$  direction over which the group of the magnetic field lines breaks apart or diffuses.
- **Anisotropy.** This method is developed from the box-counting method aiming to measure the edge length of the group of magnetic field lines. We consider that when the group of magnetic field lines expands or breaks apart, its edge length will increase.
- **Dual Lattice.** This method is also developed from the box-counting method. It uses the relationship of the number of magnetic field lines between any two neighboring boxes. The Dual Lattice Method also aims to measure the edge length of the group of magnetic field lines.
- **Principal Components.** This method is used to find the length and ratio of the principal components of the group of magnetic field lines. We can use the ratio of the principal components to find the length over the  $z$  direction which the group of magnetic field lines is sheared by the magnetic potential or diffuses.

## 3.1 Box-Counting Dimension

### 3.1.1 Method

The first method used to analyse data is box counting, a method for determining a fractal dimension. First, we have to know the definition of “dimension.” Basically, we know that a line has one dimension because we need only one independent variable to describe a neighborhood of any point. Therefore, a surface will have two dimensions and a solid cube will have three dimensions. Consider that, if we have cubes of side length  $\epsilon < 1$ , we need  $1/\epsilon$  cubes to cover a unit line,  $1/\epsilon^2$  to cover a unit surface, and  $1/\epsilon^3$  to cover a unit cube (Fig. 3.1). By the way, in the case of the unit surface, we can also use squares of side length  $\epsilon$  and in the case of the unit line, we can also use squares of side length  $\epsilon$  or segments of length  $\epsilon$ , the number of squares or segment will be the same as using the cubes of side length  $\epsilon$ . However, we use the cubes because they can be used in the whole unit line, unit surface, and unit cube cases. If  $N$  is the number of  $\epsilon$ -size cubes which are required to cover the geometric shapes we want and  $D$  is dimension of those geometric shapes, it obvious to show that (Simanca and Sutherland 2002)

$$D = -\lim_{\epsilon \rightarrow 0} \frac{\log(N)}{\log(\epsilon)}. \quad (3.1)$$

This definition can also be used for an object with fractional (non-integral) dimension, i.e., a fractal.

For tracing magnetic field lines, we set the initial locations inside a specific circle in the  $x$ - $y$  plane. Then, we trace the magnetic field lines along the  $z$  direction and collect the  $(x, y)$  positions of the magnetic field lines at each  $\Delta z$ .

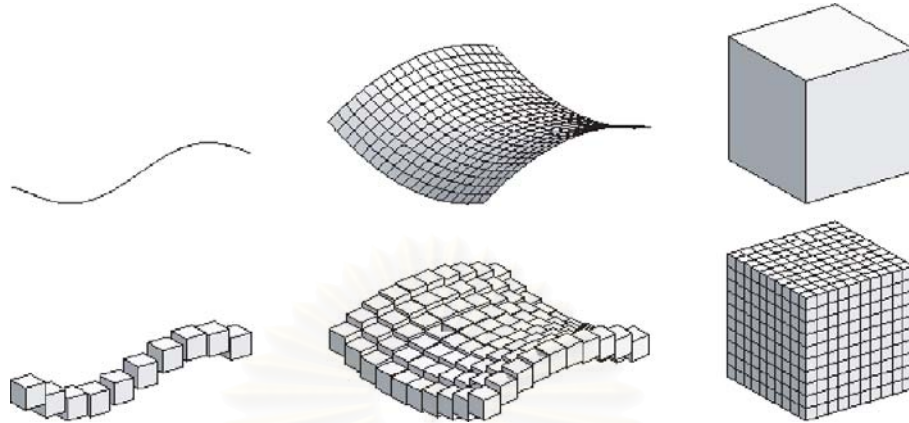


Figure 3.1: Covering a line, a surface, and a solid cube with cubes of side length  $\epsilon$ . (Picture credit: [http://www.math.sunysb.edu/~scatt/Book331/Fractal\\_Dimension.html](http://www.math.sunysb.edu/~scatt/Book331/Fractal_Dimension.html)).

However, because the limit of the memory of the computer, we can only trace a finite number  $\mathcal{N}$  of magnetic field lines. The object for which we want to measure the fractal dimension in this work is the set of the locations of magnetic field lines at each  $\Delta z$ .

By looking at the scatter plot of the group of magnetic field lines traced in a slab+2D field (Fig. 3.2), we can divide it into three regions, at  $z = 0$ , over low  $z$ , and over high  $z$ . At  $z = 0$  or at initial positions, we start all magnetic field lines at random locations in a circle. Over low  $z$ , by the effect of 2D turbulence, the group of magnetic field lines breaks apart into small groups, some of which are trapped in specific magnetic islands for a while. In this step, the group of magnetic field lines looks very much like a fractal. Finally, over high  $z$ , the group of magnetic field lines can overcome the suppression and diffuse all over the  $x$ - $y$  space. This because the magnetic field lines trapped in a magnetic island move rapidly and decorrelate the radial component of the perturbation at low  $z$ , suppressing the process of diffusive escape, but for higher  $z$  the effect of slab

turbulence makes the magnetic field lines escape from the magnetic island and diffuse (Chuychai et al. 2005). When we determine the box-counting dimension for the group of magnetic field lines in the slab+2D field, we expect to obtain different values of the dimension in these two regions.

### 3.1.2 Process

- For a given value of  $\Delta z$ , define boxes of size  $\epsilon$  over the entire simulation region (in  $x$  and  $y$ ). We start with setting a square of size  $G$  which can cover all the data points. Then, define the largest length  $\epsilon$  as  $G/3$ , rounding  $\log(\epsilon)$  to the nearest 0.05.
- Count the number of boxes ( $N$ ) which have magnetic field lines inside.
- Reduce the size of boxes. In this work, we reduce the log of the box size  $\log(\epsilon)$  by 0.05. Then, we count the number of boxes which have magnetic field lines inside again.
- Repeat the previous step until  $\epsilon$  is less than the limit value. In this work, we set the limit value to be  $0.01 \lambda_{\perp}$ .
- Plot between  $\log(N)$  and  $\log(\epsilon)$  in each step. When the plot is linear, the slope of this plot is minus one times the box-counting dimension ( $-D$ ).

## 3.2 Anisotropy

### 3.2.1 Method

As we know from Chapter II, there are different spreading and diffusion coefficients of magnetic field lines affected by pure slab turbulence and slab+2D



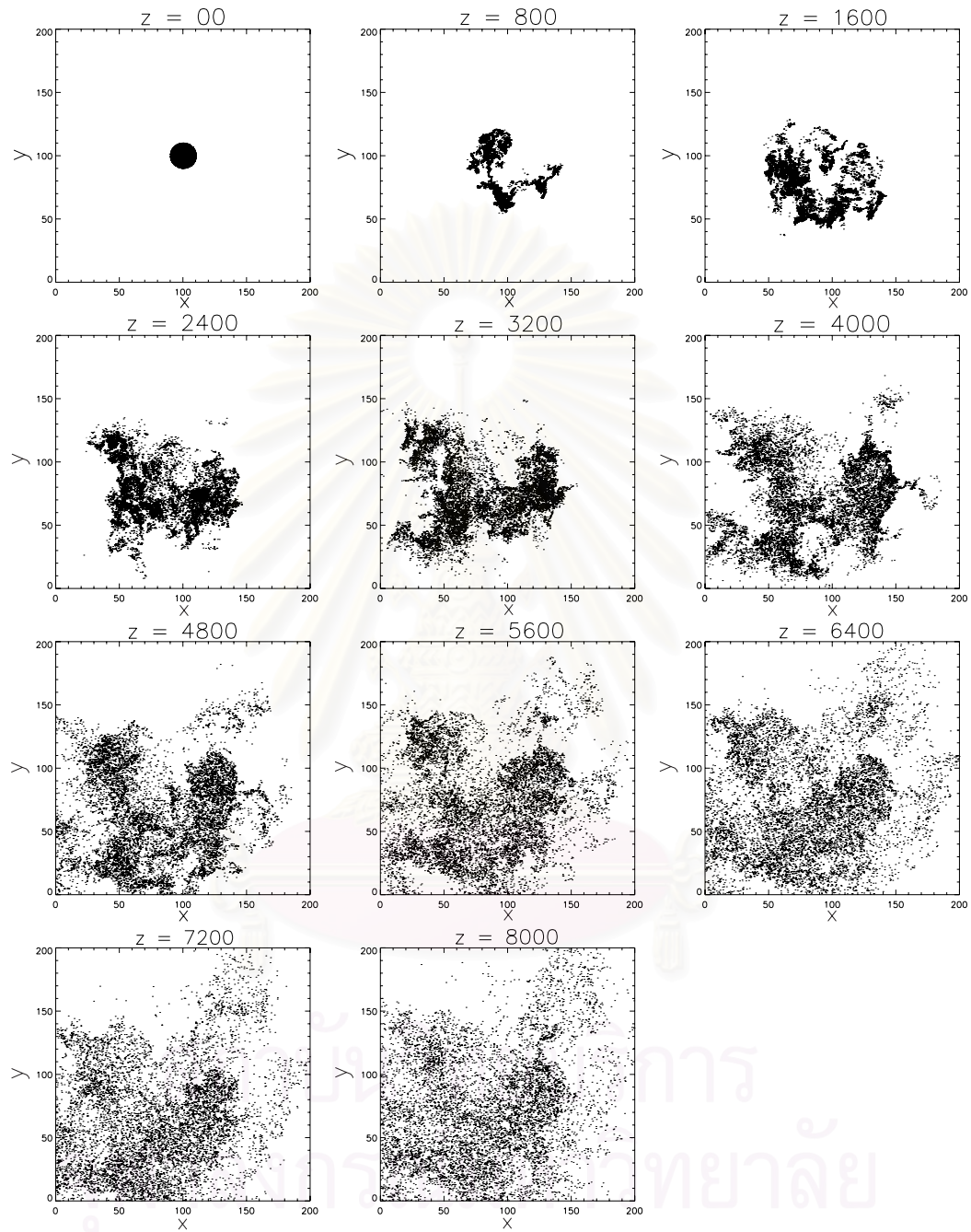


Figure 3.2: Scatter plot of magnetic field lines in slab+2D turbulent field, for varying distance  $\Delta z$  along the mean field. The energy ratio between the slab and 2D components in this simulation is 20:80 and all initial positions of magnetic field lines are at  $z = 0$ .

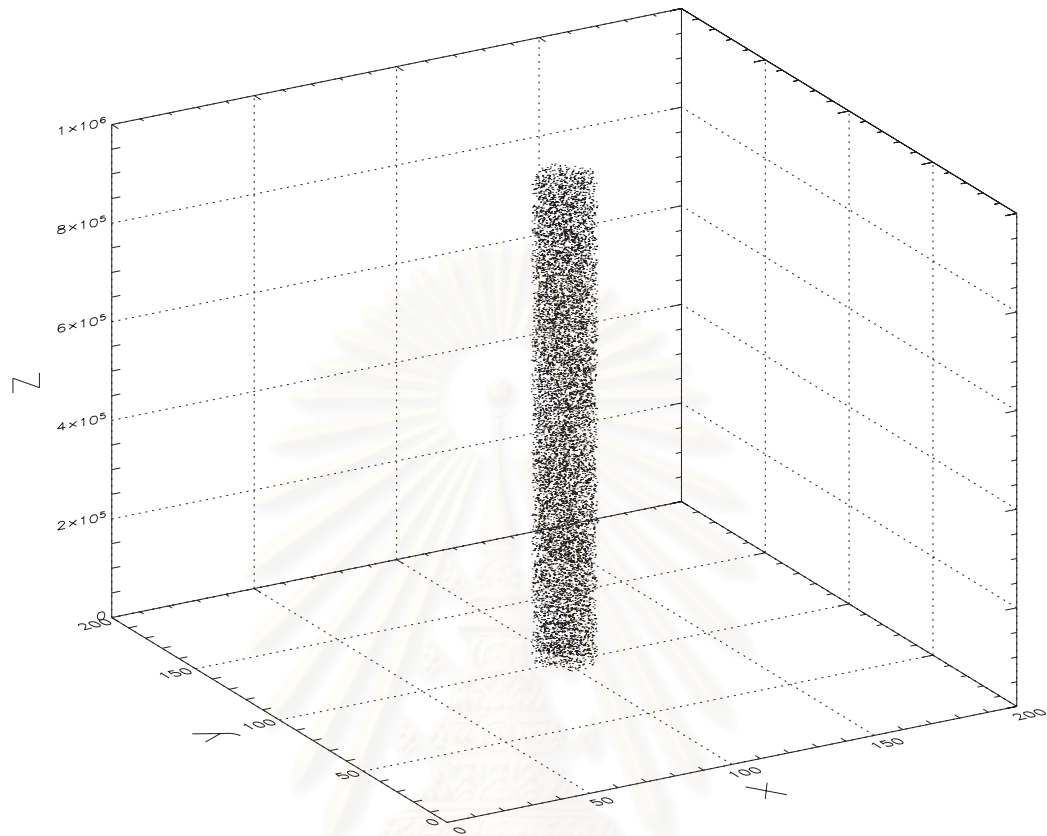


Figure 3.3: Initial positions of magnetic field lines in a pure slab turbulent field.

turbulence. In this work, for a pure slab turbulent field, we generate magnetic field lines by setting initial positions in a circle in the  $x$ - $y$  plane with random  $z$  in order to visualize the distribution of field lines (Fig. 3.3). However, in our “scatter plots,” we will plot magnetic field lines after the same  $\Delta z$  for comparison, instead of  $z$ .

For a pure slab turbulent field, from a scatter plot of magnetic field lines (Fig. 3.4), we can easily see that the group of magnetic field lines can spread throughout space without sharp boundaries and does not break apart into small groups at any  $\Delta z$  (unlike Figure 3.2). That means there are no “droupouts” as we discussed in the previous chapter for a pure slab field.

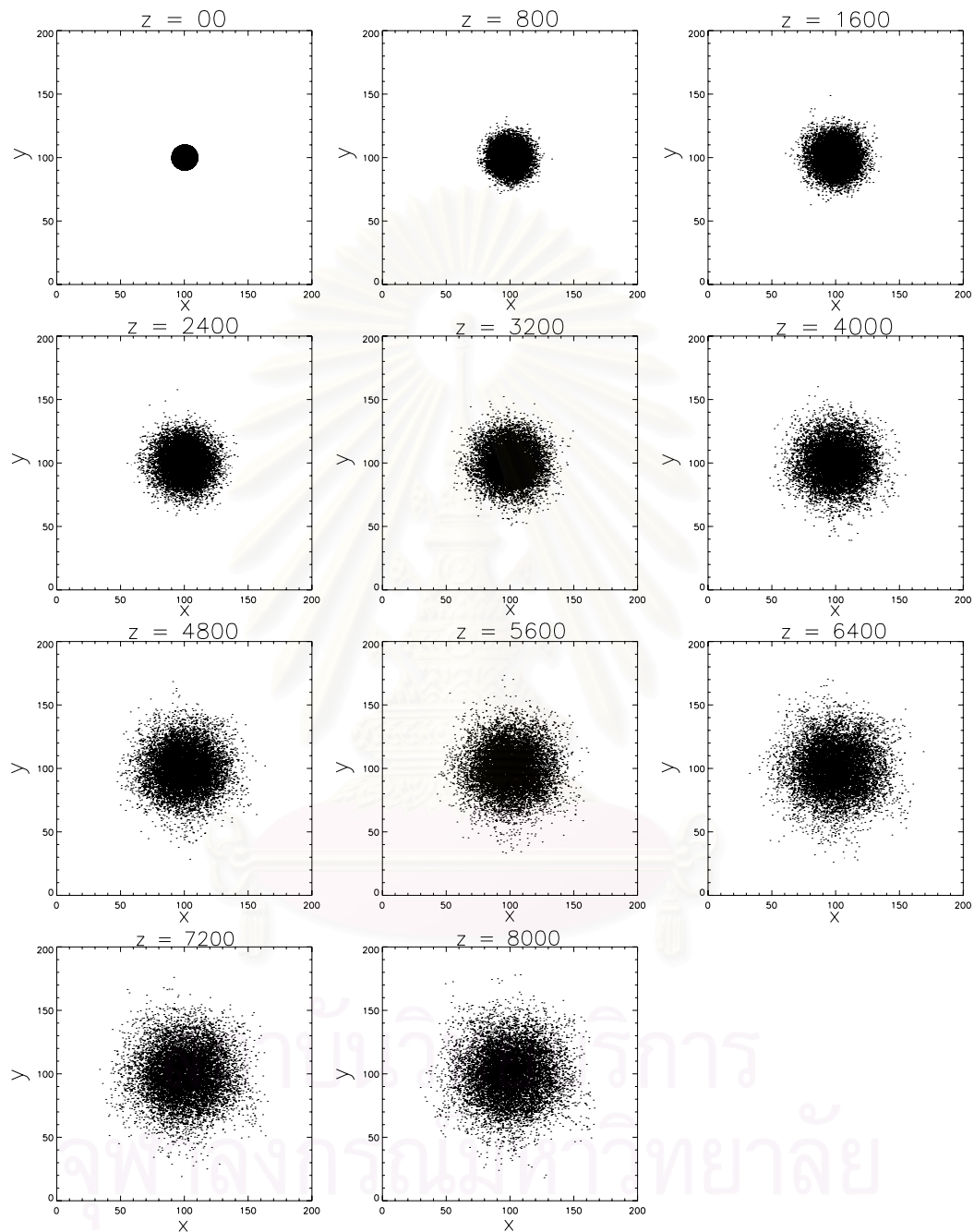


Figure 3.4: Scatter plot of magnetic field lines in pure slab turbulence. The initial positions of these magnetic field lines are in a specific circle in the  $x-y$  plane but at random  $z$  locations.

On the other hand, the distribution of magnetic field lines starting within a certain circle and then subject to slab+2D turbulence can break apart into small groups. Some field lines are trapped in magnetic islands for a while. There are also some sharp boundaries in the distribution in the  $x$ - $y$  plane over a range of  $\Delta z$  (Fig. 3.2). This is because of the 2D field can suppress the magnetic field line motion at some locations in the  $x$ - $y$  plane (Chuychai et al. 2005). We call these locations “Local Trapping Boundaries” or LTBs (Meechai 2003).

Suppose that we are at the edge of a group of magnetic field lines. Then we look over some length and measure the direction vectors of those magnetic field lines. Because we are at the edge of the group of magnetic field lines, we will see the magnetic field lines located a toward one direction in  $x$ - $y$  plane more than the other directions. Therefore, the summation of direction vectors from our location to each field line will point to the group of magnetic field lines. However, if we are inside or outside a group of magnetic field lines by more than the length we set and measure the direction vectors of magnetic field lines in the same way, the summation of direction vectors should be close to zero. Our idea is that if we are outside the group of magnetic field lines, we will not see many magnetic field lines, and if we are inside the group of magnetic field lines, we will see magnetic field lines in all directions in about the same number (Fig. 3.5). We call this phenomenon “anisotropy.” In this work, we consider that if the sum of direction vectors in a box is greater than  $5\lambda_{\perp}$ , that box is at the edge of the group of magnetic field lines. The anisotropy method is analogous to measuring the anisotropy of SEPs by using a spacecraft. If the spacecraft is outside a group of SEPs, the instrument on the spacecraft will not detect any particles. If the spacecraft is at the edge of a group of SEPs, the instrument on the spacecraft

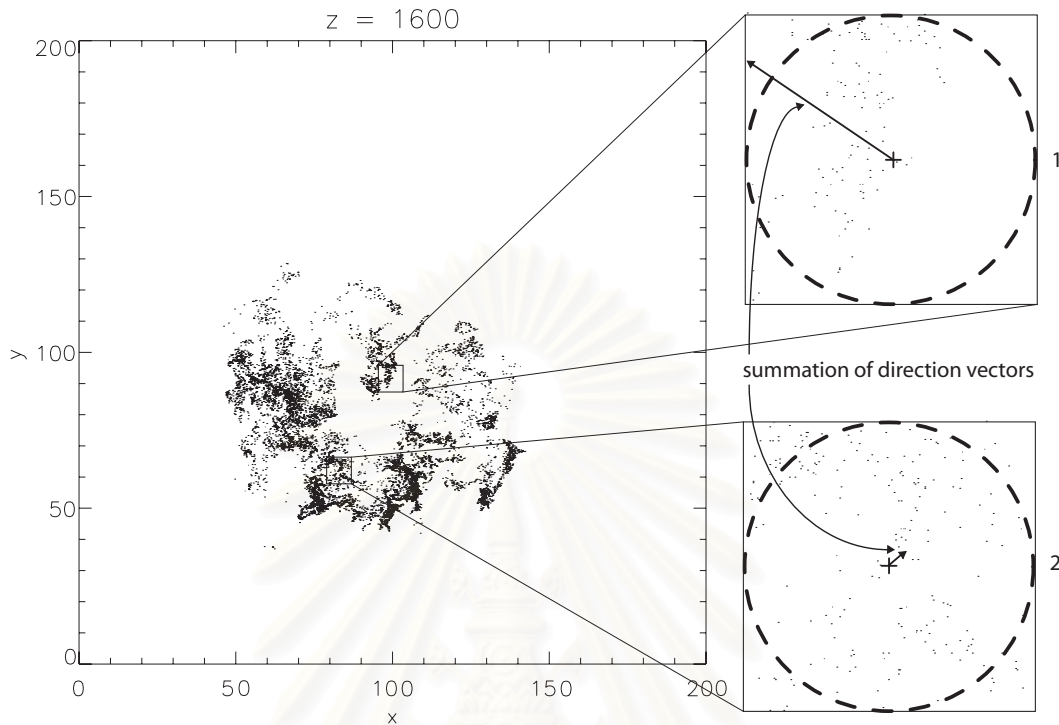


Figure 3.5: Illustration of the summation of direction vectors as a measure of anisotropy. Area 1 is at the edge of a group of magnetic field lines while area 2 is inside a group of magnetic field lines. Direction vectors to point within the dashed circle are summed. We can see that the summation of direction vectors in area 1 is larger than the summation of direction vectors in area 2. The energy ratio between the slab and 2D component in this simulations is 20:80. The initial positions of magnetic field lines are located in a circle with radius equal  $0.5\lambda_{\perp}$  in  $x$ - $y$  plane at  $z = 0$ .

will detect some particles in one direction more than the other directions. If the spacecraft is inside a group of SEPs, the instrument on the spacecraft will detect many particles with a similar intensity in all directions.

Now, let us look back to our turbulent fields and apply our idea about anisotropy to them. As we discussed before, the group of magnetic field lines in a pure slab field does not break apart and does not exhibit boundaries within the group of magnetic field lines, unlike the slab+2D field. That means that if we

set boxes over all space and measure the summation of direction vectors, then we can set a value to decide whether the amplitude of the summation of direction vectors in each box is greater than this value and whether this box is at the edge of a group of magnetic field lines. By plotting the number of boxes that are at the edge of a group of magnetic field lines, or is so-called the “anisotropy number,” vs.  $\Delta z$ , we may see different behaviors of groups of magnetic field lines between pure slab and slab+2D fields and as a function of  $\Delta z$ .

### 3.2.2 Process

- Set a grids and boxes representing areas where we will calculate direction vectors. In this work, the box size is set to be equal to  $\lambda_{\perp}$ .
- For a given  $\Delta z$ , set the length over which to sum direction vectors from the center of the box to each magnetic field line within that length.
- For each box, sum those direction vectors.
- If the summation of direction vectors is greater than value we set, it means this box is at the boundary of a group of magnetic field lines. In this work, we decide that if a box has a summation of direction vectors greater than 5 times  $\lambda_{\perp}$ , that box is at the boundary of a group of magnetic field lines.
- Count the number of boxes which are determined to be at a boundary for each  $\Delta z$  and plot the number of boxes vs.  $\Delta z$ .



## 3.3 Dual Lattice

### 3.3.1 Method

Like the Anisotropy Method, the Dual Lattice Method aims to measure the diffusion and dispersion of a group of magnetic field lines in pure slab and slab+2D turbulence. However, there is difference between the Anisotropy Method and Dual Lattice Method. The Anisotropy Method uses the summation of direction vectors from the center of each box to magnetic field lines in that box to decide which box is at the edge of the group of magnetic field lines. The Dual Lattice Method uses a ratio of the number of magnetic field lines in each box with the neighboring boxes to decide which boxes are at the edge of a group of magnetic field lines.

At the edge of a group of magnetic field lines, if we count the number of magnetic field lines in the boxes, we will see that the number of magnetic field lines in each box will change rapidly along a row. That means the ratio of the number of magnetic field lines between a box at the edge of the group of magnetic field lines and the neighboring box will much higher or lower than one. On the other hand, if we are inside or outside the group of magnetic field lines, the number of magnetic field lines will be rather constant. Therefore, the ratio of number of the magnetic field lines between boxes inside or outside the group of magnetic field lines and their neighbors will be close to one. In the case that some boxes and their neighboring boxes contain zero or very few magnetic field lines, we can consider that this pair of boxes is isolated and can neglect the result of their dual lattice.

For example, in Figure 3.6, the ratio of the number of magnetic field lines in the left box and the central box is 2.64:1, while the ratio of the number of

magnetic field lines in the central box and the right box is 1:0.02. We can decide that the junction between the left box and the central box is inside a group of magnetic field lines. (Actually, this junction may be inside or outside a group of magnetic field lines, but the picture clearly shows that it is inside.) The junction between the central box and the right box is considered to be at the edge of a group of magnetic field lines.

Using this idea, we can consider the distribution of magnetic field lines, if we set boxes over all space and find the ratio of the number of magnetic field lines for every pair of neighboring boxes. Then, by plotting between the number of boundaries between two boxes where the ratio of the number of magnetic field lines between those two boxes is greater than an assigned value, or is so-called the “dual lattice number,” at each  $\Delta z$  versus  $\Delta z$ , we can better understand the behavior of pure slab fields and slab+2D fields (Fig. 3.6).

### 3.3.2 Process

- Set boxes over all  $(x, y)$  space. In this work, the box’s size is set to equal to  $\lambda_{\perp}$ .
- Count the number of magnetic field lines in each box.
- Compare the number of magnetic field lines in each box with those in the neighboring boxes in both  $x$  and  $y$  directions. In this work, we set that if the ratio of the number of magnetic field lines between the current box and the neighboring box is greater than 6 (or less than  $1/6$ ), we will count this boundary as being at the edge of a group of magnetic field lines.
- Plot between the number of boundaries determined to be at the edge of a group of magnetic field lines versus  $\Delta z$ .

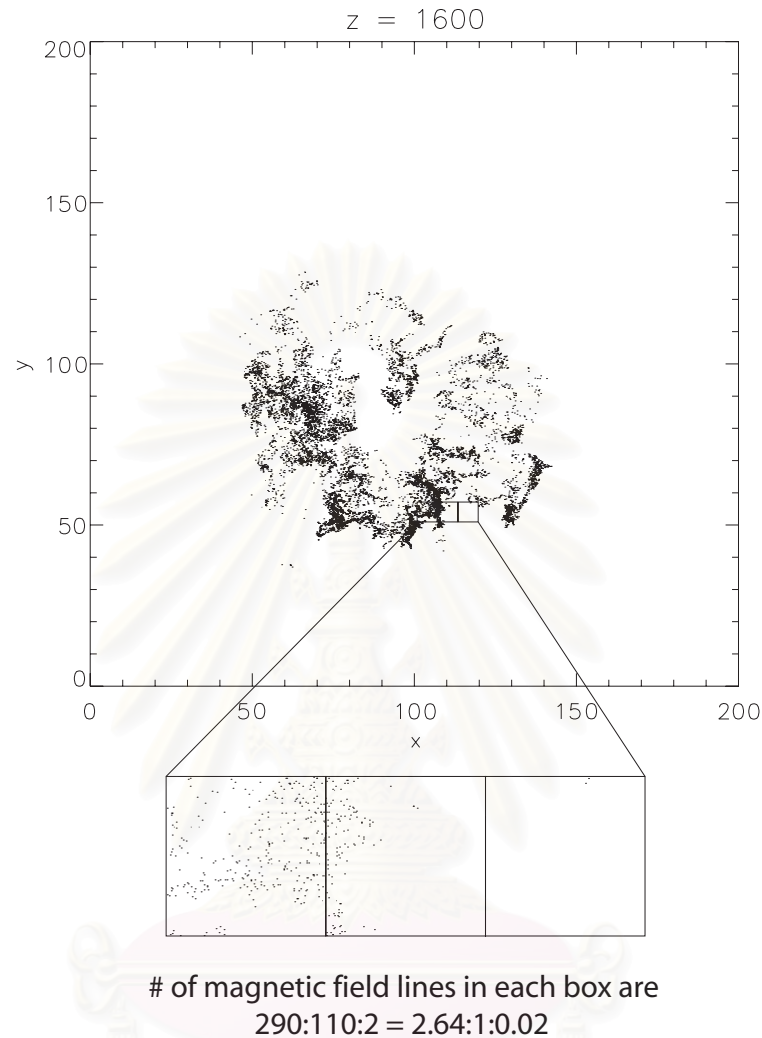


Figure 3.6: Illustration of the Dual Lattice Method. In this work, we define that if the number of magnetic field lines in one box more than 6 times greater or lesser than that in the neighboring box, we will decide that the junction between these boxes is at the edge of a group of magnetic field lines and count it. The junction between the central box and the right box is considered to be at the edge of a group of magnetic field lines, while that between the left box and the central box is not.

## 3.4 Principal Components

### 3.4.1 Method

This method uses a different idea from the previous methods. By looking at the scatter plot of magnetic field lines again, we will see another, different aspect of the behavior of the group of magnetic field lines between pure slab, pure 2D and slab+2D fields.

For a pure slab field with random initial positions of magnetic field lines, the group of magnetic field lines will diffuse with the same rate in all directions in the  $x$ - $y$  plane. This will occur all over  $\Delta z$ .

For a pure 2D field, normally a magnetic field line will follow the equipotential line of the potential function,  $a(x, y)$ . A group of magnetic field lines will also do so. However, because the group of magnetic field lines has two dimensions, it is subject to shearing.

For a slab+2D field, at low  $\Delta z$ , the group of magnetic field lines is sheared along the equipotential line of the potential function like in a pure 2D field. Then, it will diffuse a bit perpendicular to the equipotential line and also break apart at higher  $\Delta z$ . Finally, it will diffuse throughout space like in a pure slab field.

We can use the Principal Component Method to analyse data from the simulations. The Principal Component Method uses the idea of finding axes that characterize the distribution of the data. The new axes, which are called “principal components,” are more related to the dispersion of the data than the original axes. If data spread out with the same rate in every direction in the  $x$ - $y$  plane, like the group of magnetic field lines in a pure slab field with random initial  $z$  positions, the ratio of elongation along principal component will be close to one. On the other hand, if the data spread out in one direction more than

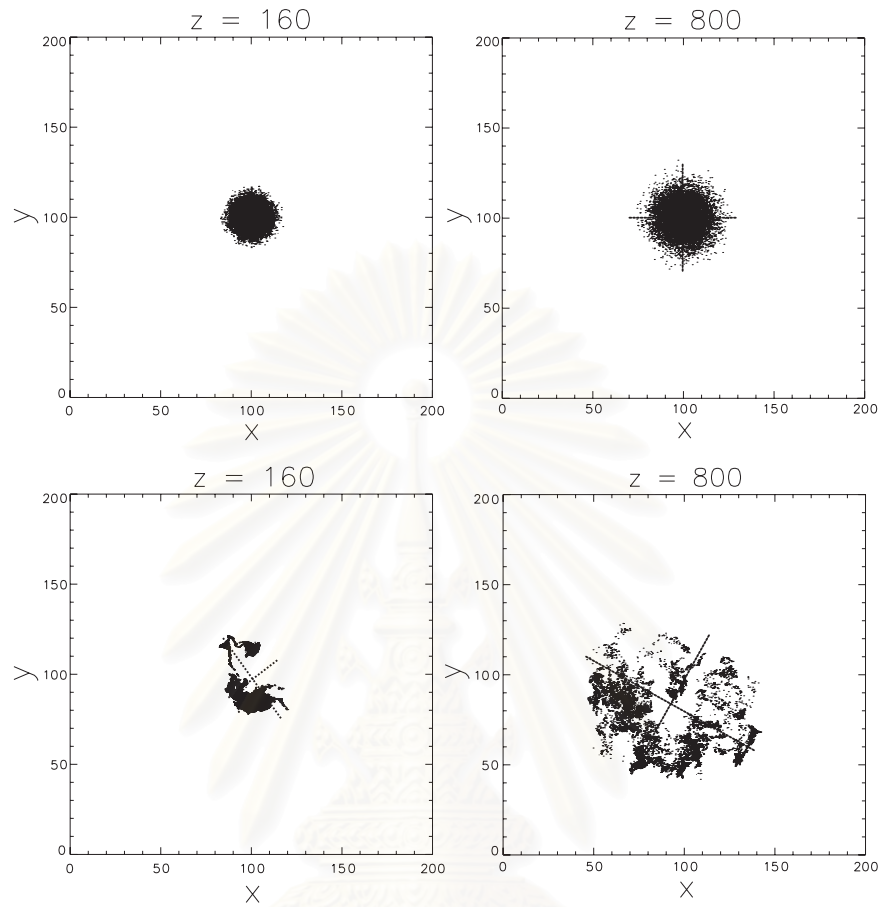


Figure 3.7: Illustration of the principal components. The top figures show the group of magnetic field lines in pure slab turbulence with a random initial position in  $z$ . The principal components of this group of magnetic field lines in both directions have similar lengths. The figures on the bottom show the group of magnetic field lines in a slab+2D field. The principal component of this group of magnetic field lines is longer in one direction than the other one. Furthermore, the ratio of principal components of the group of magnetic field lines in the slab+2D field at low  $z$  is greater than the ratio of principal components at higher  $z$ .

the other direction, like the group of magnetic field lines in a slab+2D field over low  $\Delta z$ , the ratio of data between each principal component will be much higher than one (Fig. 3.7).

In this work, for the Principal Component Method, we would like to

consider the results of the ratio between the principal component and the length of the longest principal component of the group of magnetic field lines along the  $z$  direction to understand the behavior of the group of magnetic field lines. Furthermore, we also consider those results for a varying energy ratio between slab and 2D turbulence. However, we use the results from the diffusion of the magnetic field lines with random initial positions in  $z$  in the pure slab field as the control run.

### 3.4.2 Process

- Find mean values in each dimension ( $x$  and  $y$ ).
- Calculate the Covariance Matrix, defined as

$$C = \begin{pmatrix} cov(x, x) & cov(x, y) \\ cov(y, x) & cov(y, y) \end{pmatrix},$$

where  $cov(x, y)$  is the covariance, which is defined as

$$cov(x, y) = \frac{\sum_{i=1}^n (x_i - \bar{x})(y_i - \bar{y})}{(n - 1)},$$

and so on.

- Calculate eigenvalues and eigenvectors of the Covariance Matrix and use these eigenvectors as new axes of the data.
- Measure the ratio of principal components of the data along each axis.
- Plot the ratio of principal component and the longest principal component of the data at each  $\Delta z$  vs.  $\Delta z$ .



# CHAPTER IV

## RESULTS AND DISCUSSIONS

### 4.1 Box-Counting Dimension

We use the Box-Counting Method to find the fractal dimension of the group of the magnetic field lines at each  $\Delta z$ . We expect a change in the fractal dimension over all  $\Delta z$ . By using the changing fractal dimension data, we hope to indicate over which regions of  $\Delta z$  the magnetic field lines have the dropout behavior and over which regions the magnetic field lines diffuse throughout all space. In this simulation we use the following parameters: the energy ratio between the fluctuations and the mean field is 0.5, the energy ratio of the fluctuations between the slab turbulence and the 2D turbulence is 20:80, the radius of the initial circle is  $0.5\lambda_{\perp}$ , the parallel length scale is  $1.0\lambda_{\perp}$ , and the perpendicular length scale is 10.0. The results show that the fractal dimension values at each  $\Delta z$  are similar (Figures 4.1 to 4.6). We can trace only a finite number of magnetic field lines, as we discussed in Chapter III, and the results depend on that number of the magnetic field lines. However, we have developed other methods, such as the Anisotropy Method and the Dual Lattice Method, from the Box-Counting Method to improve the data analysis.

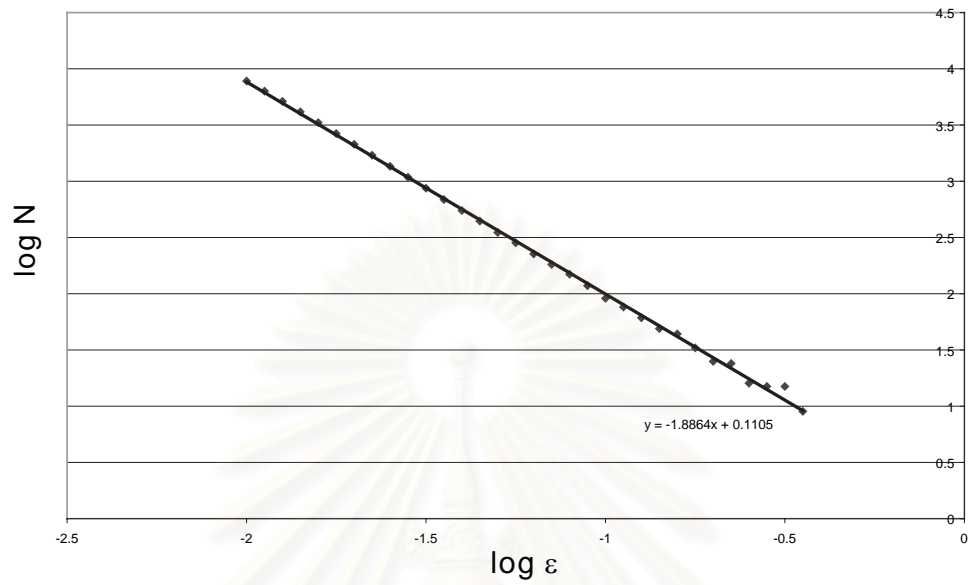


Figure 4.1: The number of boxes containing the magnetic field lines vs. the size of the boxes at  $\Delta z = 0$ .

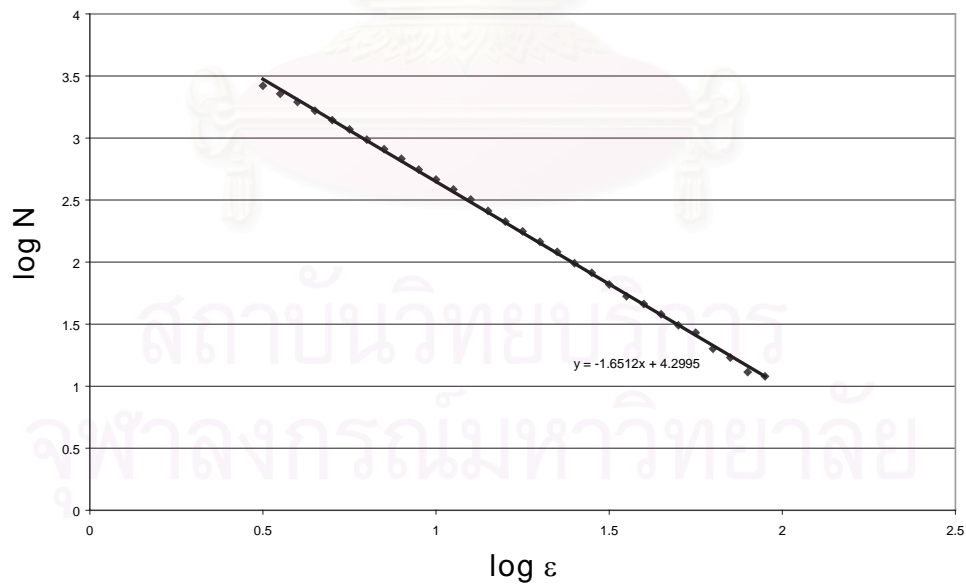


Figure 4.2: The number of boxes containing the magnetic field lines vs. the size of the boxes at  $\Delta z = 20$ .

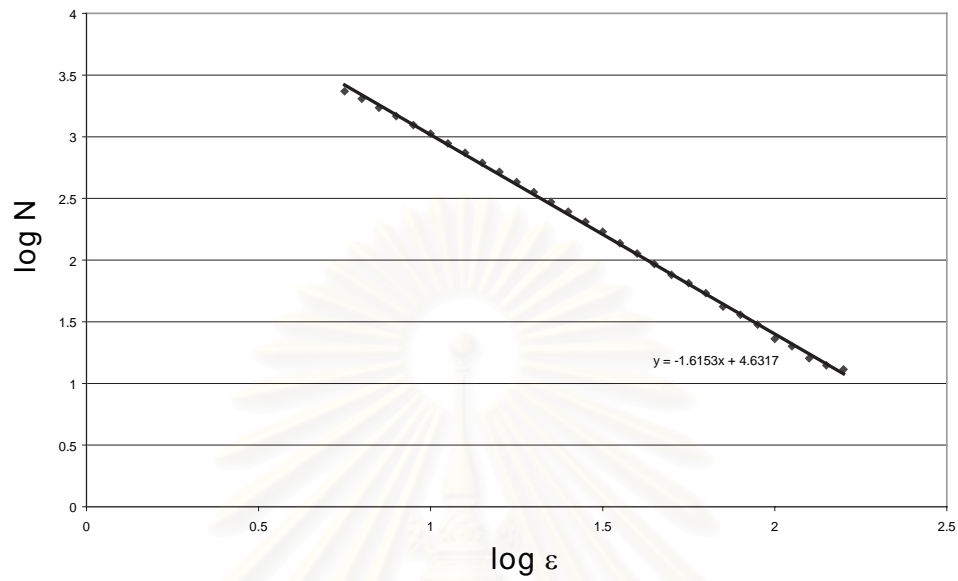


Figure 4.3: The number of boxes containing the magnetic field lines vs. the size of the boxes at  $\Delta z = 40$ .

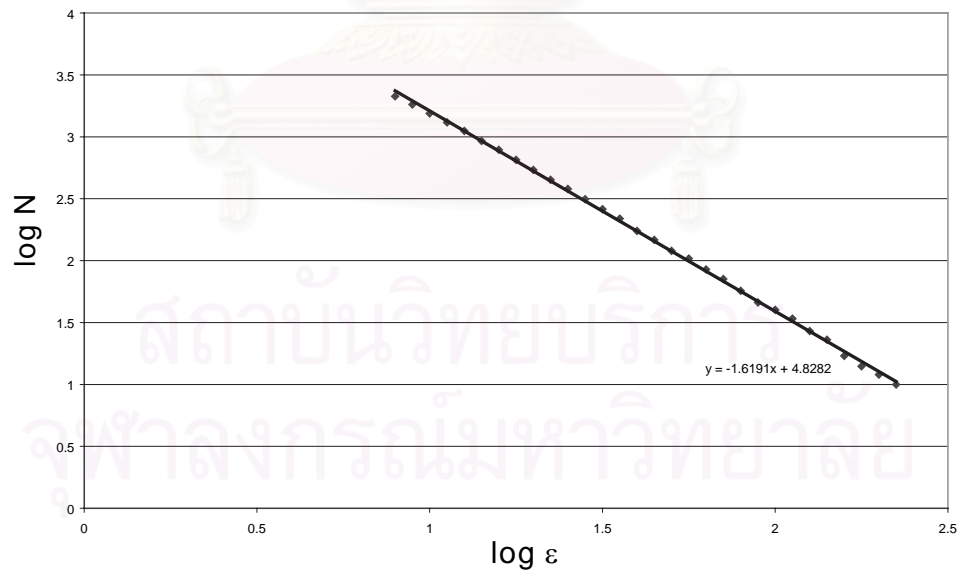


Figure 4.4: The number of boxes containing the magnetic field lines vs. the size of the boxes at  $\Delta z = 60$ .

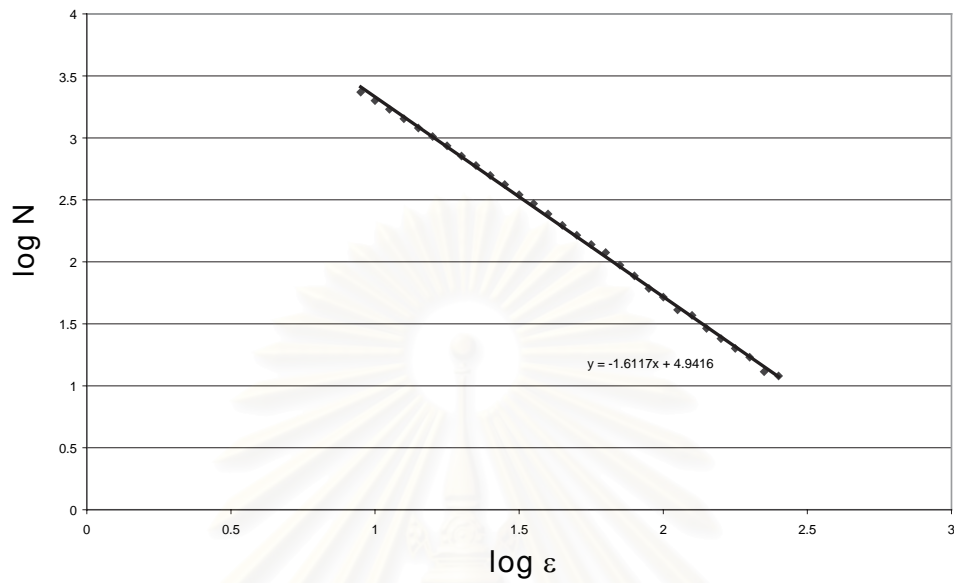


Figure 4.5: The number of boxes containing the magnetic field lines vs. the size of the boxes at  $\Delta z = 80$ .

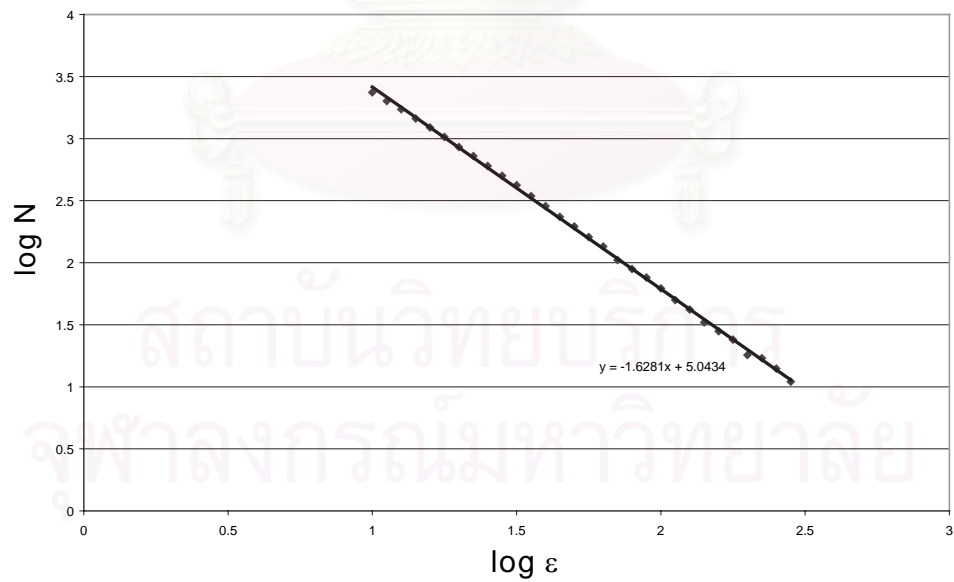


Figure 4.6: The number of boxes containing the magnetic field lines vs. the size of the boxes at  $\Delta z = 99$ .

## 4.2 Anisotropy

For the Anisotropy Method, we vary four parameters: the ratio between the turbulence fluctuations and the mean field ( $b/B_0$ ), the radius of the initial circle ( $\rho$ ), the parallel scale length ( $\lambda_{\parallel}$ ), and the perpendicular scale length ( $\lambda_{\perp}$ ). All of the results in this section (and some in subsequent sections) are displayed in this pattern: the top panel shows the results from the group of magnetic field lines in the pure slab field with random initial positions in  $z$ , the middle panel shows the results from the group of magnetic field lines in a turbulent field where the energy ratio between the slab and 2D components is 99:1 with initial positions at  $z = 0$  within a certain circle in the  $x-y$  plane, and the bottom panel shows the results from the group of magnetic field lines in a turbulent field where the energy ratio between the slab and 2D components is 20:80 with initial positions at  $z = 0$  within a certain circle in the  $x-y$  plane. As a default value, we take the turbulent fluctuation energy to be 0.5 of the mean field energy. By the way, in this work, we vary this parameter to be 0.25, 0.5, 0.75, 1.00, and 2.00. We also change the energy ratio between the slab turbulence and the 2D turbulence between three values: the pure slab field with random initial positions of the magnetic field lines in  $z$ , the turbulent field where the energy ratio between the slab and 2D components is 99:1 with initial positions at  $z = 0$  within a certain circle in the  $x-y$  plane, and the turbulent field where the energy ratio between the slab and 2D components is 20:80 with initial positions at  $z = 0$  within a certain circle in the  $x-y$  plane.

For the pure slab field with random initial positions in  $z$ , when we increase the fluctuation ratio to the mean field, the width of graph will become more narrow and peak of the anisotropy number decreases (Figures 4.7 to 4.11). This

is because increasing the fluctuations makes the field lines separate more quickly. The quick separation rate causes the group of magnetic field lines to spread throughout all space and the edge of the group of magnetic field lines reaches the edge of the simulation box quickly. Thus, we will measure a lower anisotropy number.

When the energy ratio between the slab turbulence and the 2D turbulence is 20:80, the results show that when we increase the energy of fluctuations, the peak of the anisotropy number will appear at lower  $z$ . This because the anisotropy ends when the slab turbulence fuzzes out the distribution of the magnetic field lines. Comparing with the idea of dropouts in SEPs from Ruffolo et al. (2003), the length of  $\Delta z$  at which the anisotropy number is high is analogous with the region between  $z_1 = \rho^2/(4D_{sep})$  and  $z_2 = d^2/(16D_{slab})$ , where  $\rho$  is the radius of the circle where the SEPs are injected,  $D_{sep}$  is the diffusion coefficient of the field line separation,  $d$  is the diameter of the magnetic island, and  $D_{slab}$  is the diffusion coefficient of the slab fluctuations. In the region between  $z_1$  and  $z_2$ , the spacecraft can observe the dropout phenomenon.

By comparing the graphs of the anisotropy number for an energy ratio between the slab and 2D turbulence of 99:1 with 20:80, the results show that reducing the slab fluctuations makes the anisotropy number rise and fall at a shorter  $\Delta z$ . This because  $D_{sep} = 2D_{2D}^2/D_{\perp}$  (Ruffolo et al. 2004). While  $D_{\perp}$  has a similar value,  $D_{2D}^2$  is much larger for the 20:80 ratio. Thus, we can infer that reduced slab the magnetic field lines separate and fuzz out at a shorter  $\Delta z$ .



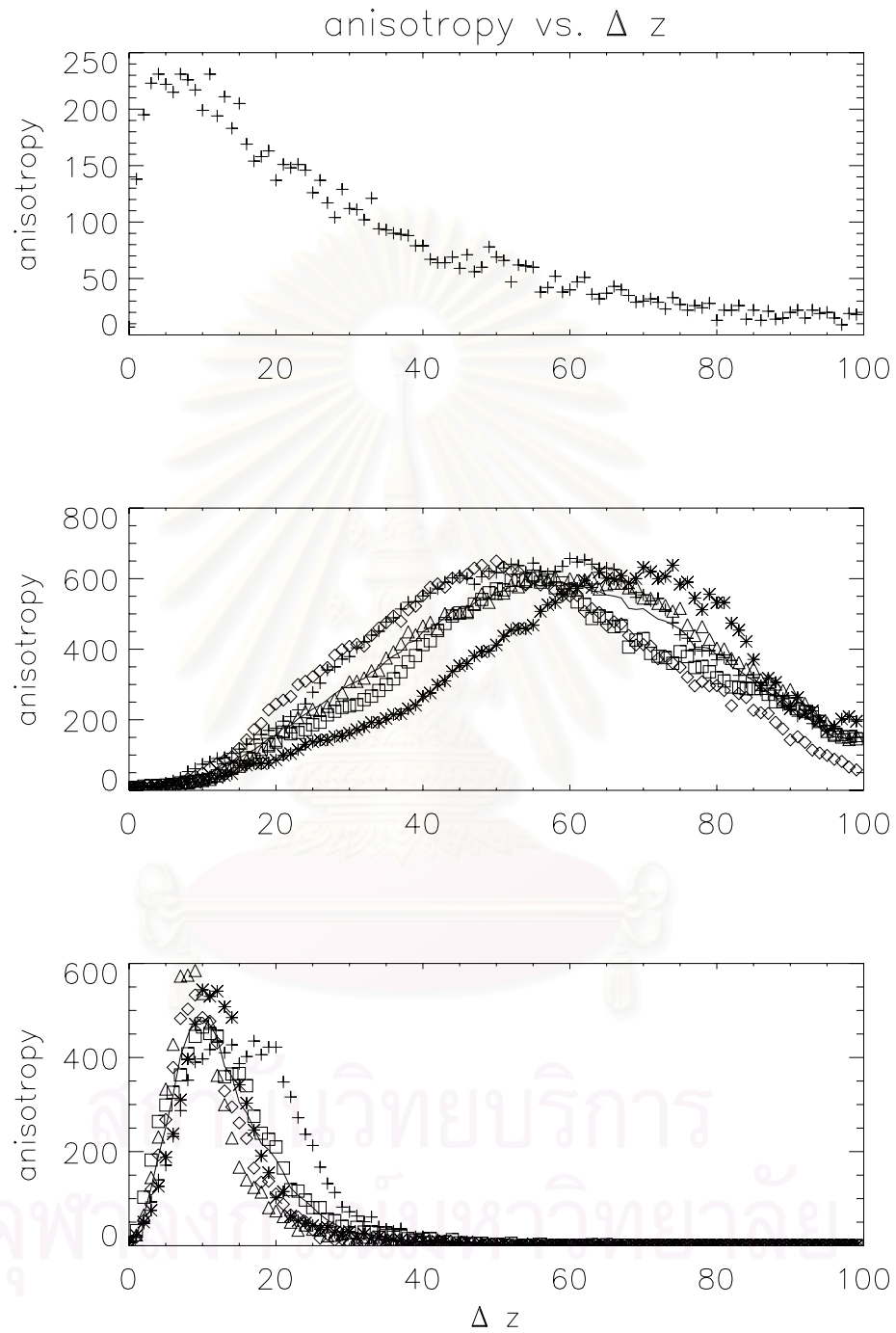


Figure 4.7: Anisotropy number vs.  $\Delta z$  when the turbulence fluctuation to mean field ratio is 0.25.

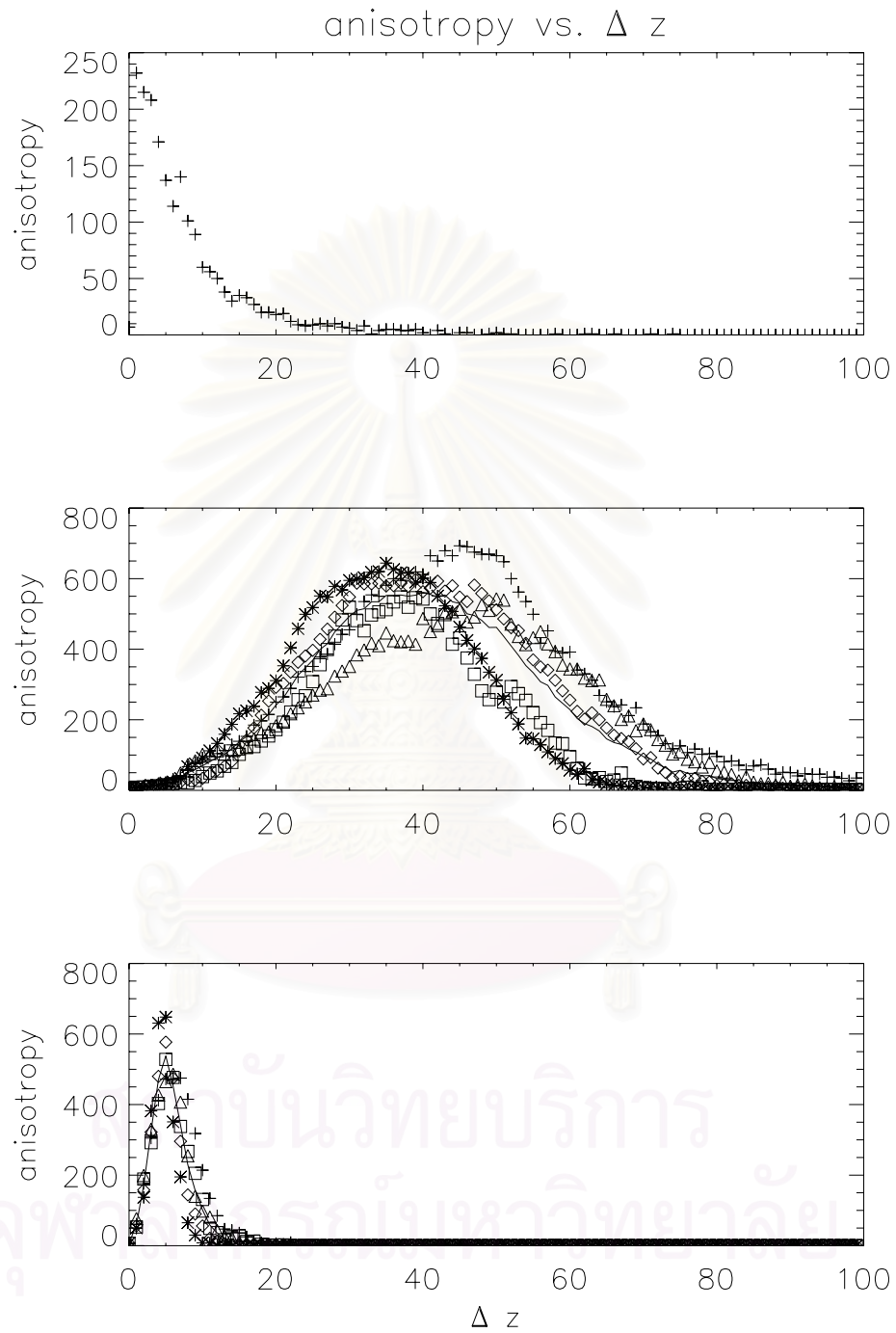


Figure 4.8: Anisotropy number vs.  $\Delta z$  when the turbulence fluctuation to mean field ratio is 0.50.

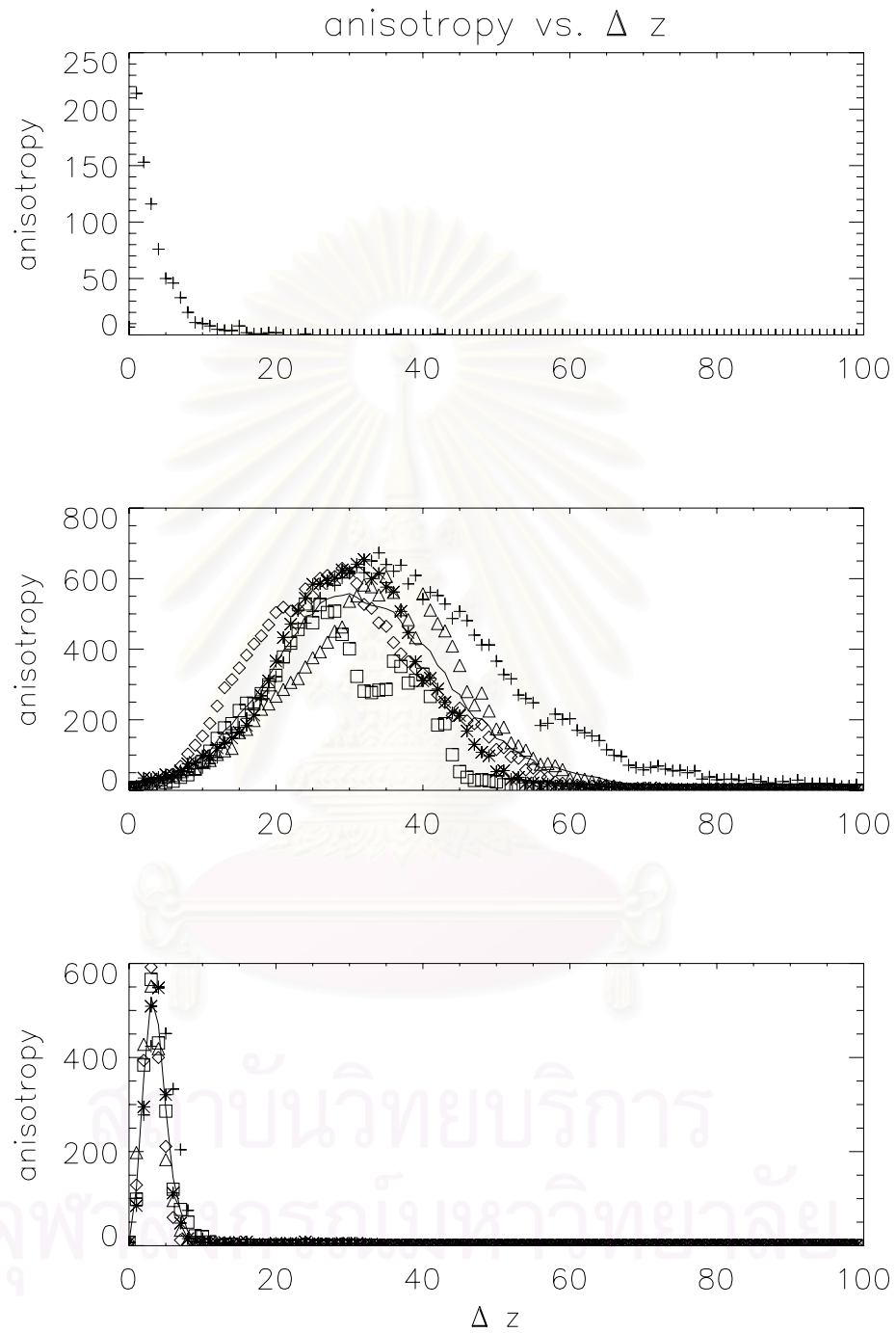


Figure 4.9: Anisotropy number vs.  $\Delta z$  when the turbulence fluctuation to mean field ratio is 0.75.

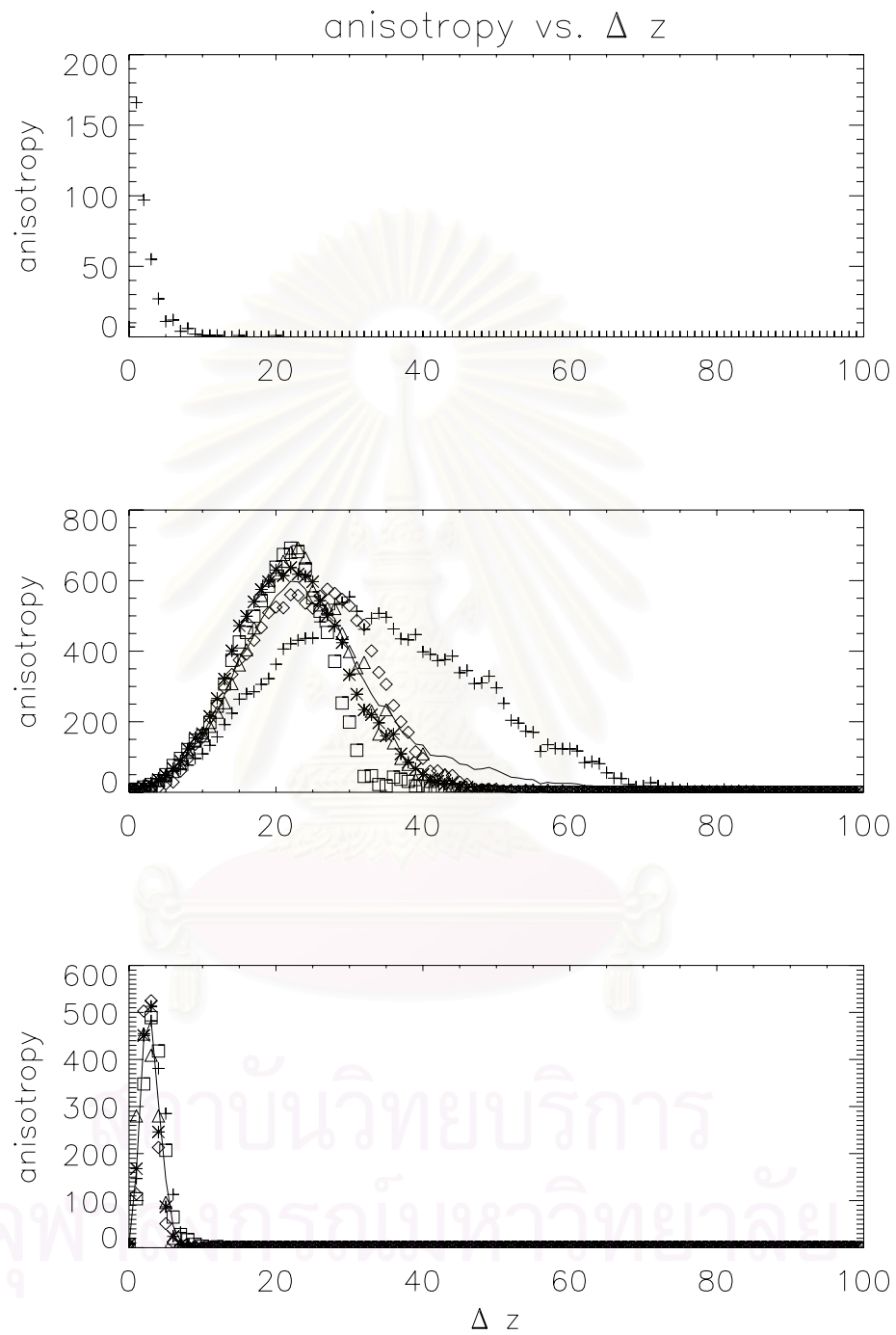


Figure 4.10: Anisotropy number vs.  $\Delta z$  when the turbulence fluctuation to mean field ratio is 1.00.

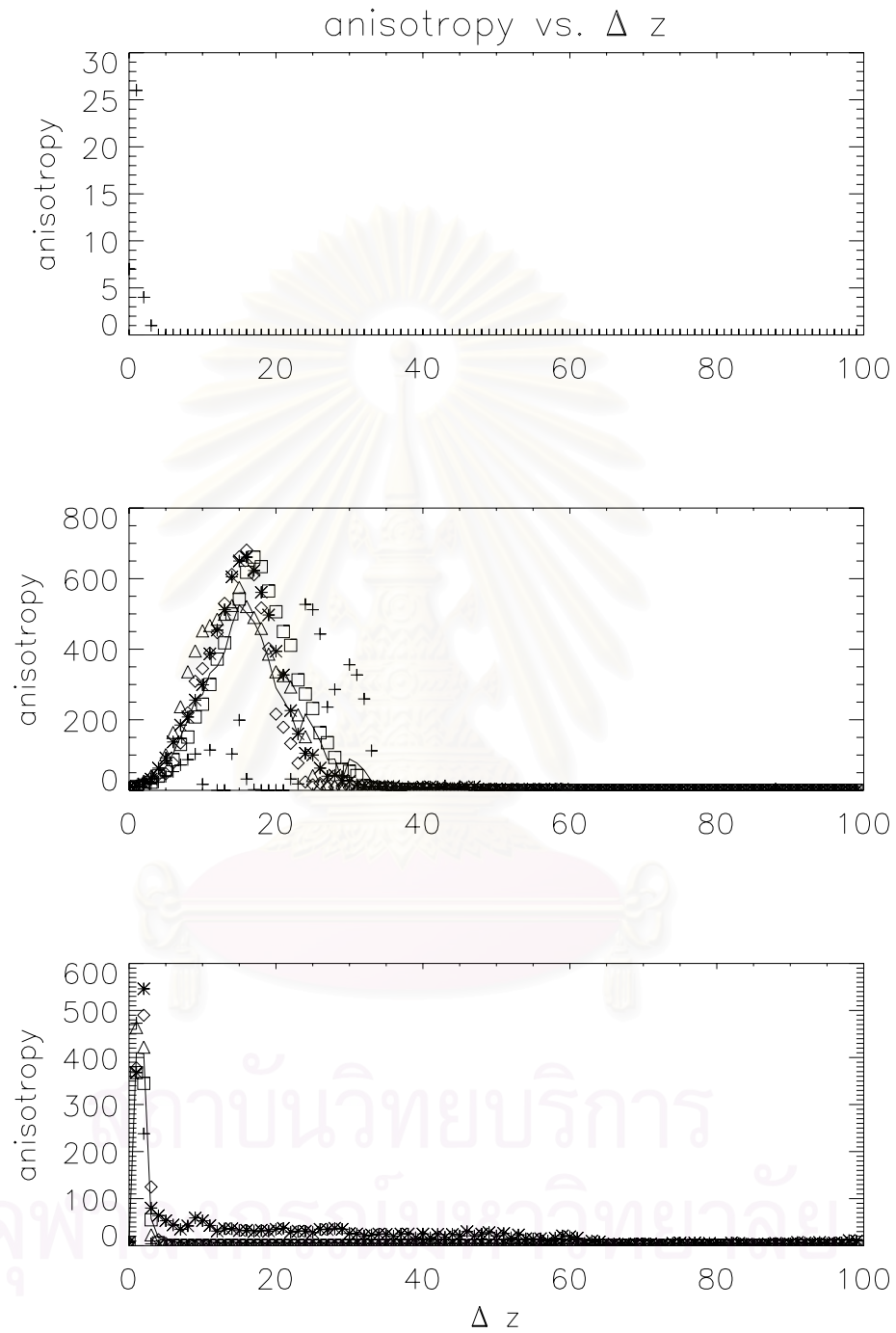


Figure 4.11: Anisotropy number vs.  $\Delta z$  when the turbulence fluctuation to mean field ratio is 2.00.

For the size of the initial circle of magnetic field line locations in the  $x$ - $y$  plane, we use the radius of the initial circle ( $\rho$ ) as 0.5, 1.0, 2.0, 4.0, 8.0, 16.0, and 32.0 in the units of  $\lambda_{\perp}$ . The default value is  $\rho = 0.5\lambda_{\perp}$ . We test the effect of the initial circle size on the separation and the diffusion of the group of magnetic field lines.

Note that the results for  $\rho = 32\lambda_{\perp}$  are different from the others (Fig. 4.18), because in this simulation we trace a finite number (10,000) of magnetic field lines and we set the size of boxes to measure the direction vectors equal to  $\lambda_{\perp}$ , so for  $\rho = 32\lambda_{\perp}$  each box will contain only a few magnetic field lines on average. Thus, the anisotropy number for this  $\rho$  value is much less than for the other  $\rho$  values.

In the pure slab field with random initial positions in  $z$ , at  $\Delta z = 0$ , when we increase  $\rho$  the anisotropy number increases, too. This because the larger initial circle gives the longer length along the boundary of that circle. Then, at higher  $\Delta z$ , the anisotropy number reduces similarly at every  $\rho$  because the turbulence makes the magnetic field lines diffuse throughout space.

When the energy ratio between the slab turbulence and 2D turbulence is 99:1, the graphs of anisotropy number for all radii of the initial circle have a similar amplitude and duration (Figures 4.12 to 4.17). However, the peak of the graph appears at lower  $\Delta z$  when we increase  $\rho$ . Because the group of magnetic field lines with a larger initial circle has the longer edge length at  $\Delta z = 0$ , so the anisotropy number is higher at  $\Delta z = 0$ , too. However, because of the same value of parallel and perpendicular length scales, the rate of field line separation and the duration of trapping is similar. Thus, the graphs of the anisotropy number rise with a similar rate and have a similar width for all  $\rho$ .



When the energy ratio between the slab turbulence and 2D turbulence is 20:80, the peak of the graph of anisotropy number appears at lower  $\Delta z$  for the higher initial circle size while the amplitude and width of the graph are similar. The reason is the same as for the 99:1 ratio. However, comparing the graph between both energy ratios, the graphs of anisotropy number for 20:80 ratio rise faster but have a smaller amplitude and shorter duration. This because the increased 2D turbulence makes the group of magnetic field lines separate and diffuse much more rapidly.



สถาบันวิทยบริการ  
จุฬาลงกรณ์มหาวิทยาลัย

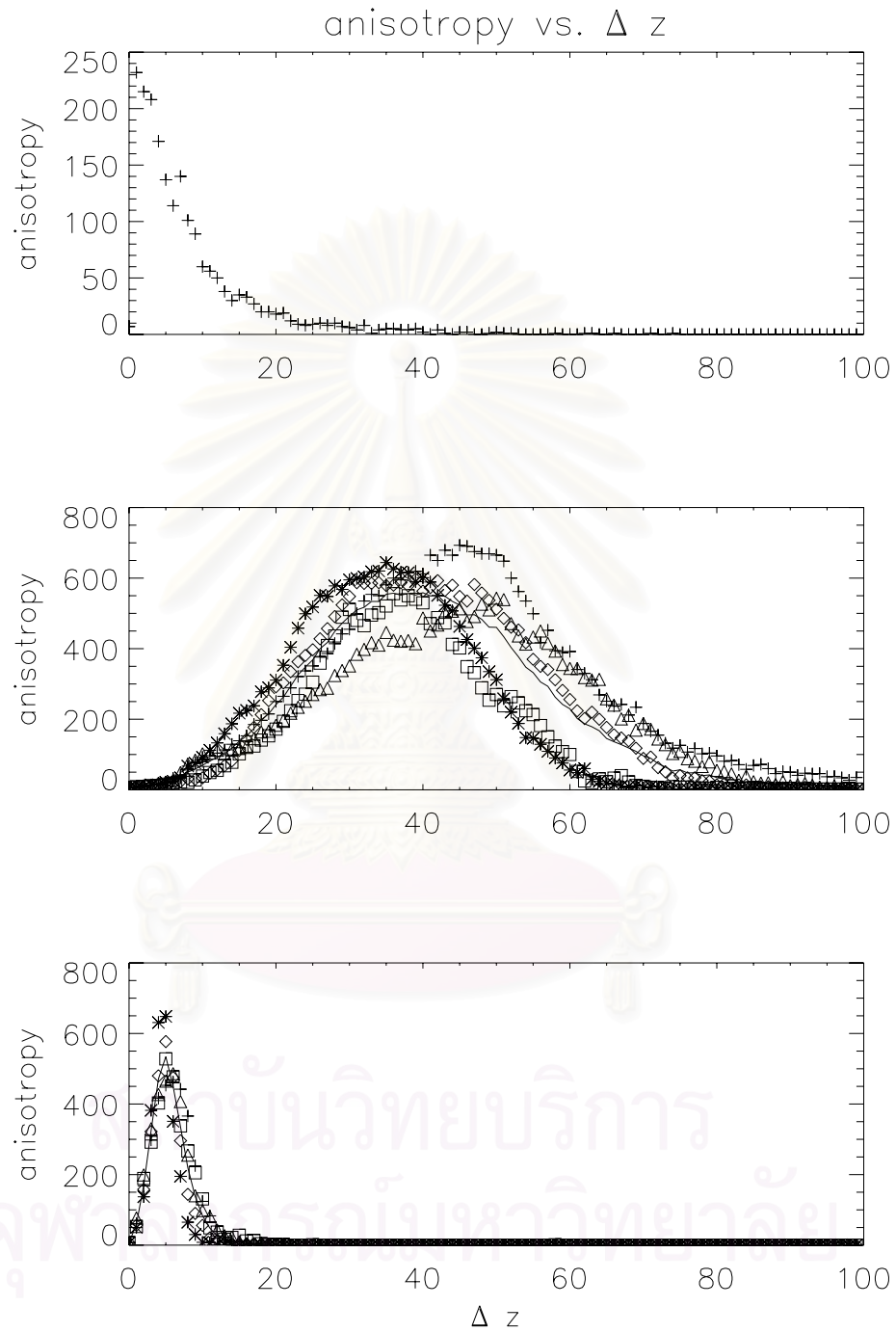


Figure 4.12: Anisotropy number vs.  $\Delta z$  when the radius of the initial circle is  $0.5\lambda_{\perp}$ .

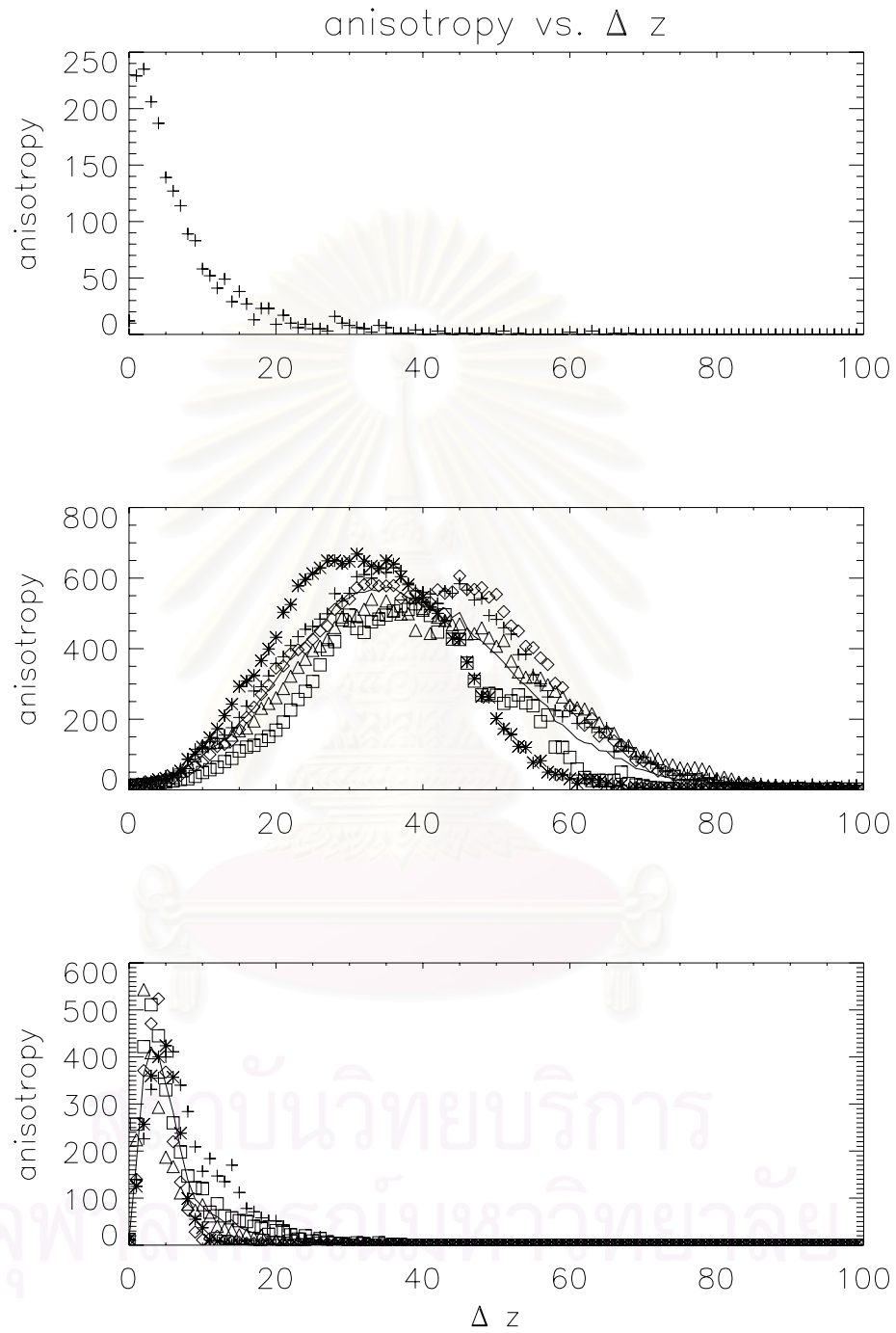


Figure 4.13: Anisotropy number vs.  $\Delta z$  when the radius of the initial circle is  $1.0\lambda_{\perp}$ .

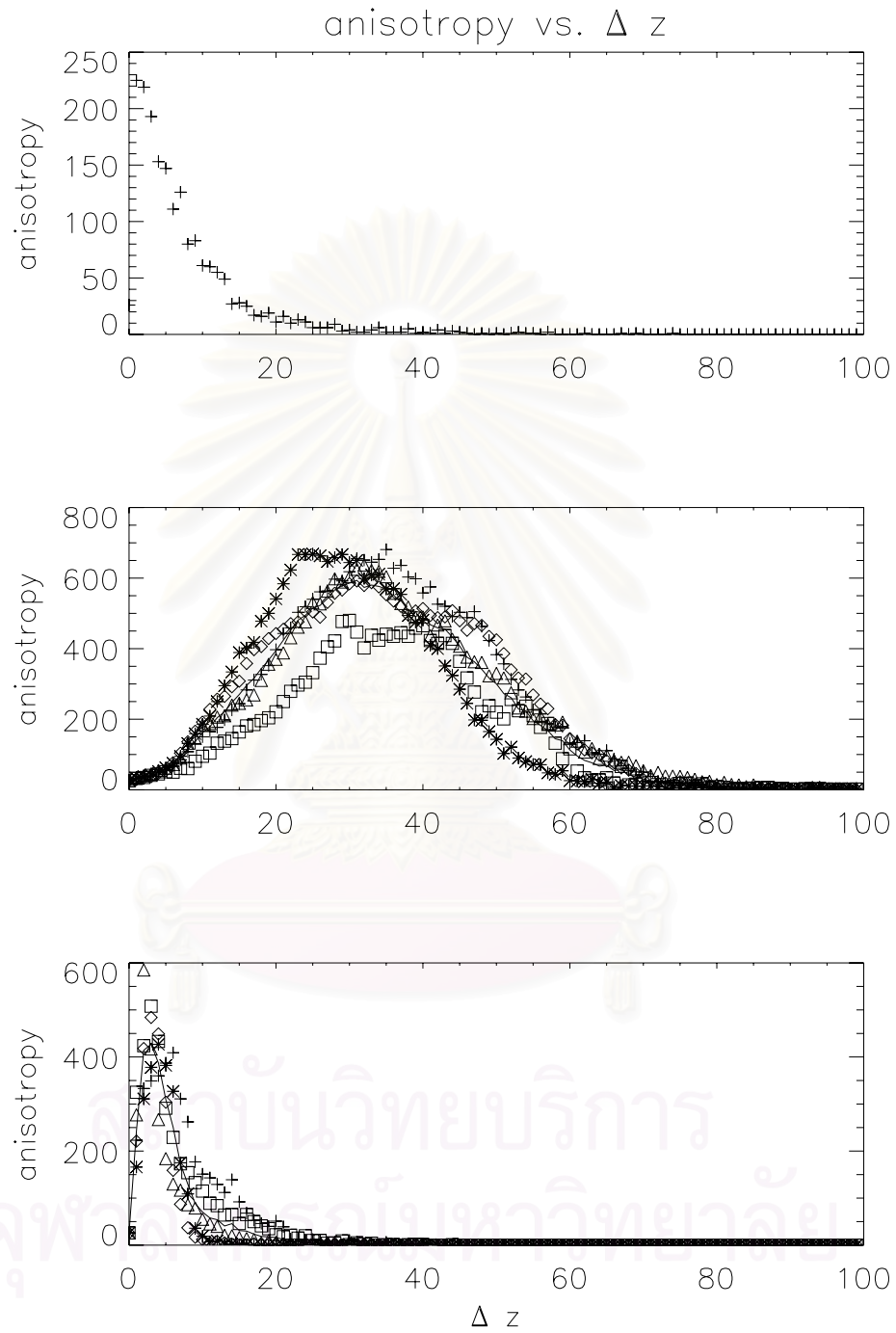


Figure 4.14: Anisotropy number vs.  $\Delta z$  when the radius of the initial circle is  $2.0\lambda_{\perp}$ .

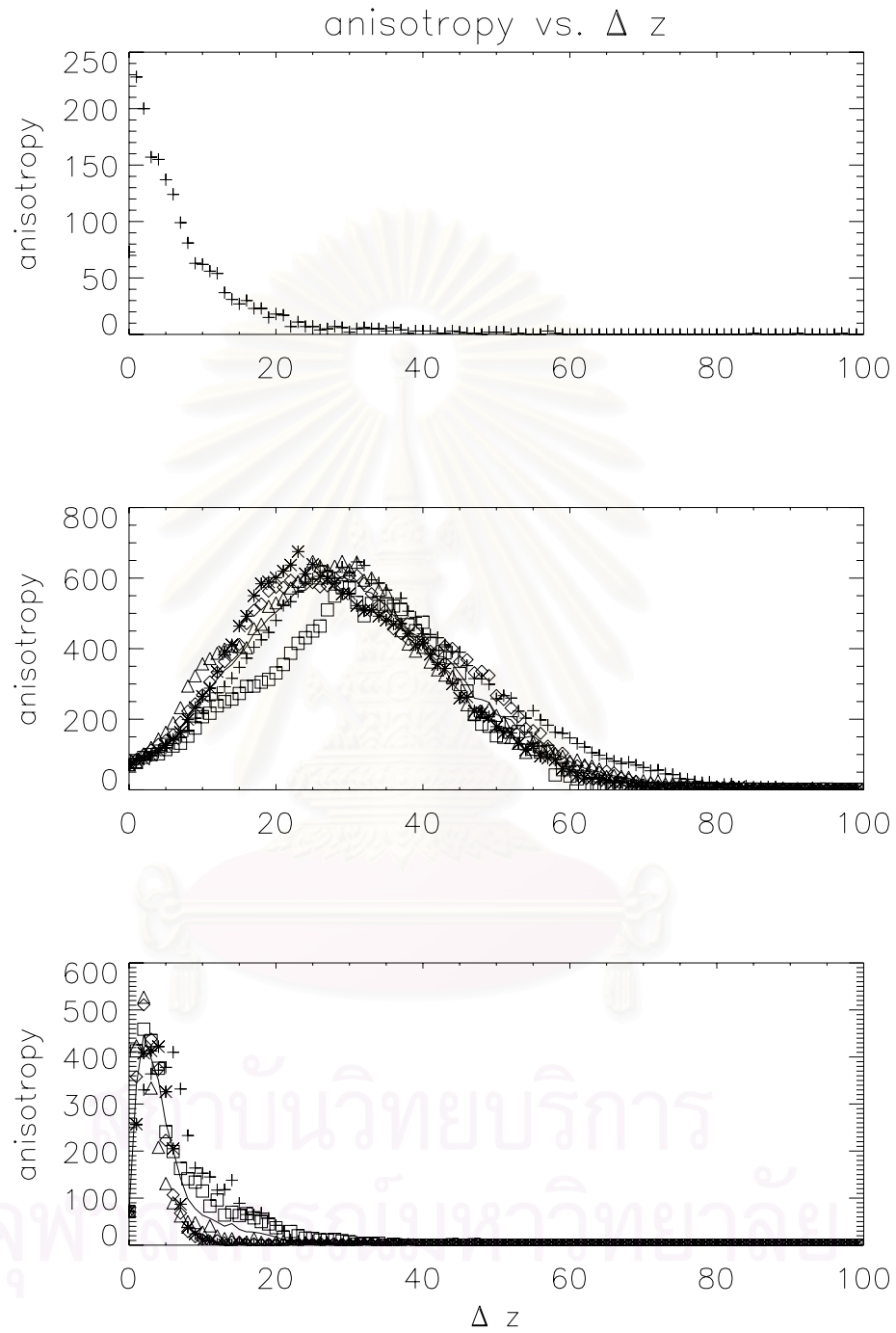


Figure 4.15: Anisotropy number vs.  $\Delta z$  when the radius of the initial circle is  $4.0\lambda_{\perp}$ .

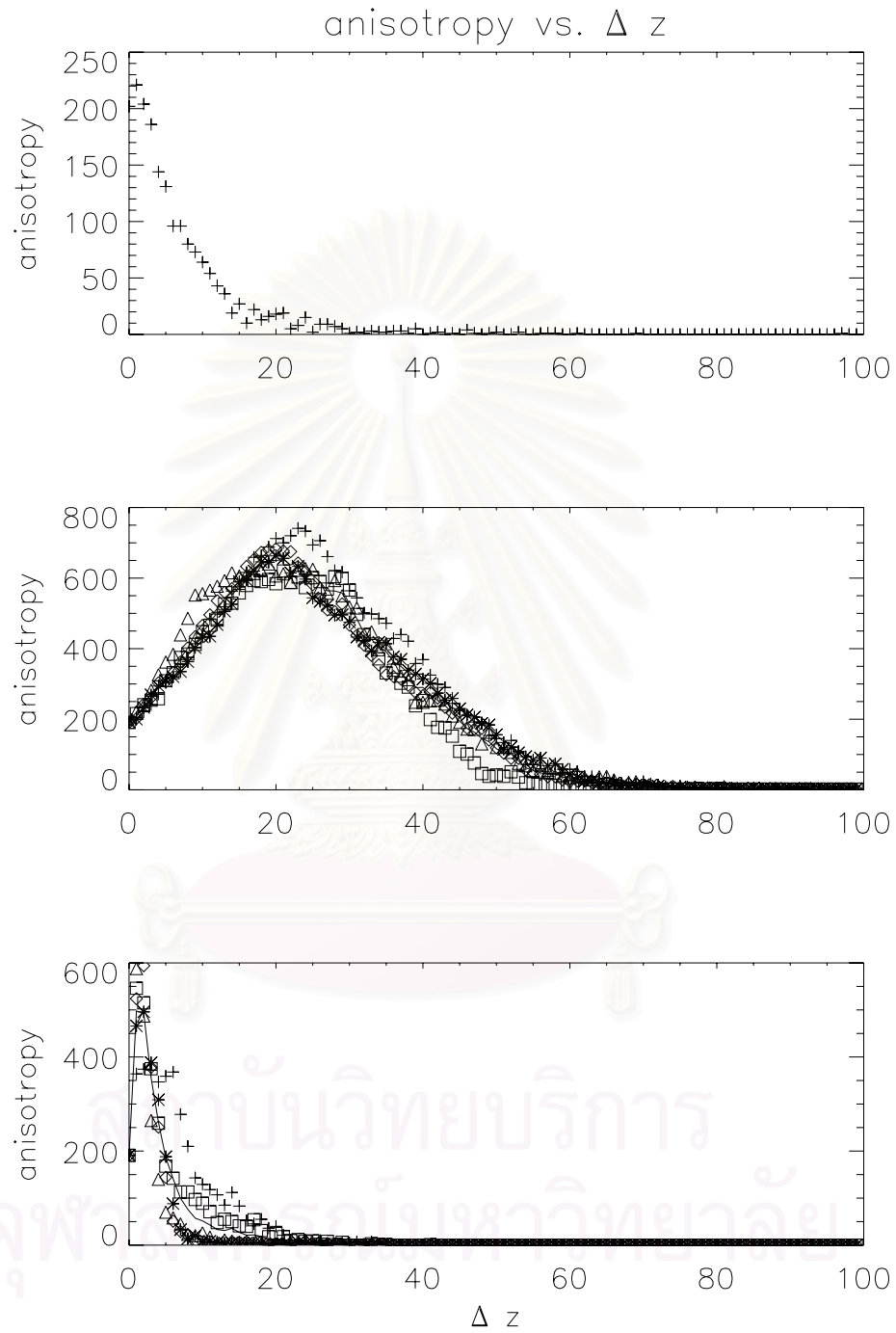


Figure 4.16: Anisotropy number vs.  $\Delta z$  when the radius of the initial circle is  $8.0\lambda_{\perp}$ .



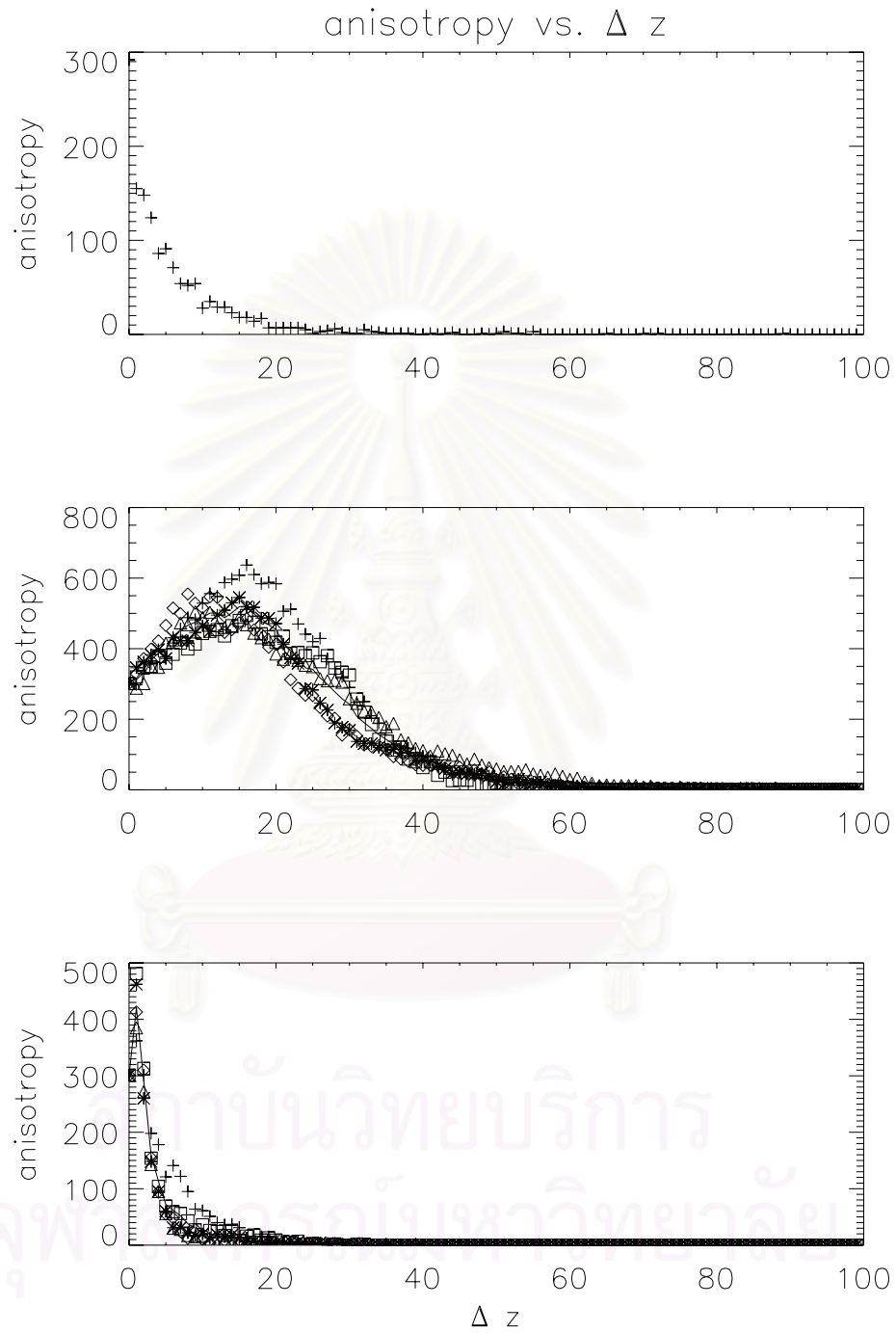


Figure 4.17: Anisotropy number vs.  $\Delta z$  when the radius of the initial circle is  $16.0\lambda_{\perp}$ .

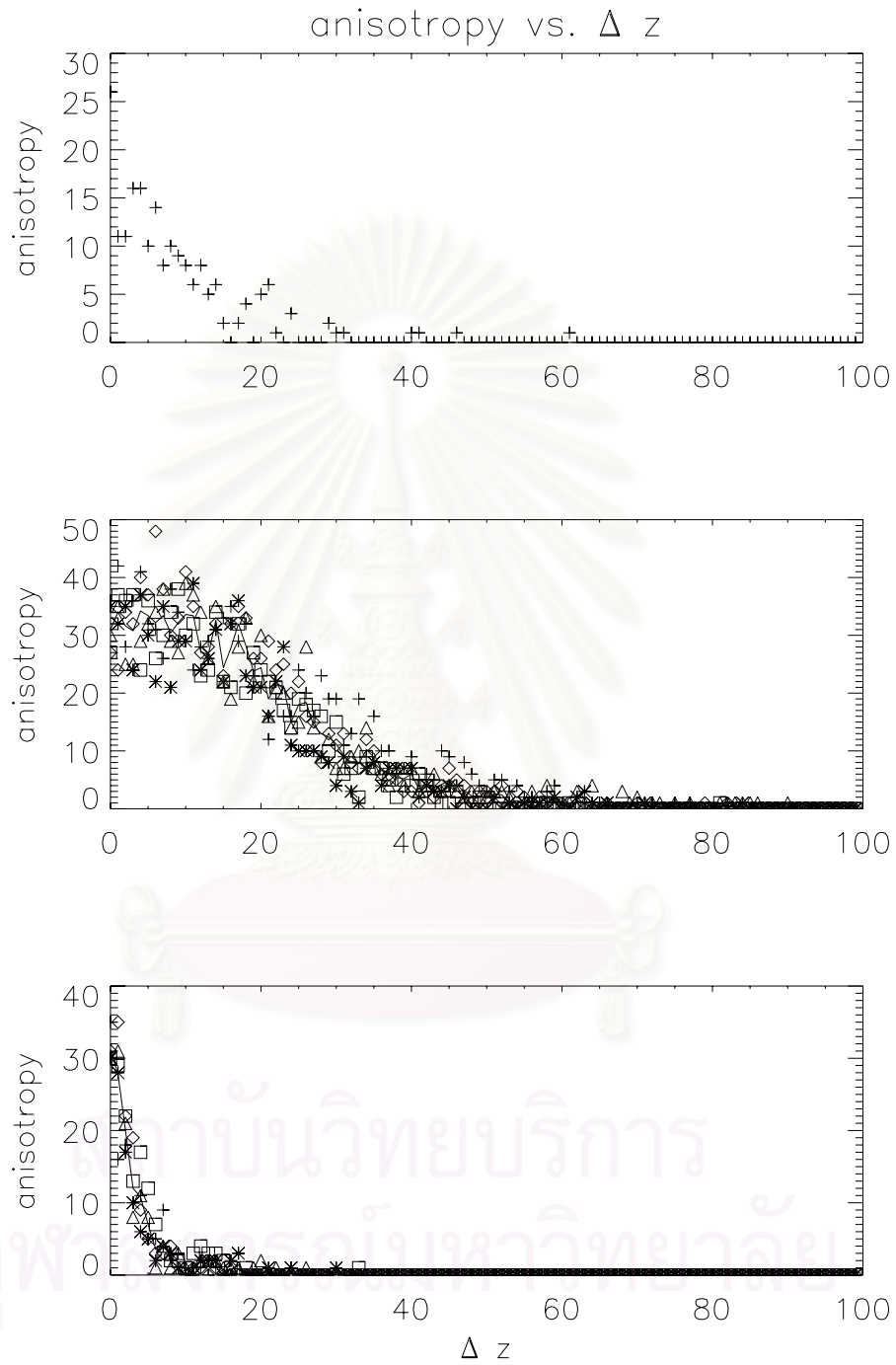


Figure 4.18: Anisotropy number vs.  $\Delta z$  when the radius of the initial circle is  $32.0\lambda_{\perp}$ .

The next parameter we want to test is the parallel length scale ( $\lambda_{\parallel}$ ). As a default we set this parameter to 1.00. In this work, we vary this parameter as 0.25, 0.50, 1.00, 2.00, 5.00, 10.00, and 20.00 in units of  $\lambda_{\perp}$ . The  $\lambda_{\parallel}$  value is related to the correlation length of the magnetic field ( $\ell_c$ ), which affects the separation of the field lines directly or indirectly. In the pure slab turbulence with random initial  $z$  values, when  $\lambda_{\parallel}$  increases, the peak of the anisotropy number appears at lower  $\Delta z$  (Figures 4.19 to 4.25). In that case  $D_{sep} = 2D_{slab}$ , where  $D_{slab} \propto \lambda_{\parallel}$ . Therefore, when  $\lambda_{\parallel}$  increases,  $D_{sep}$  increases, too. Thus any changes occur at lower  $\Delta z$ . On the other hand, if we add the 2D turbulence and start tracing the magnetic field lines at  $z = 0$ ,  $D_{sep}$  becomes  $D_{sep} = 2D_{2D}^2/D_{\perp}$  (Ruffolo et al. 2004). Here  $D_{\perp}$  depends on  $D_{slab}$  weakly for the case of 20% slab energy and strongly for 99% slab energy. In the latter case,  $D_{sep}$  depends on  $1/\lambda_{\parallel}$ . Thus, when we increase  $\lambda_{\parallel}$ , the anisotropy number will rise more slowly. Note that at high  $\Delta z$  for  $\lambda_{\parallel} = 5$  to 20, the group of magnetic field lines reaches the edge of the simulation box. This makes the anisotropy number become zero suddenly.

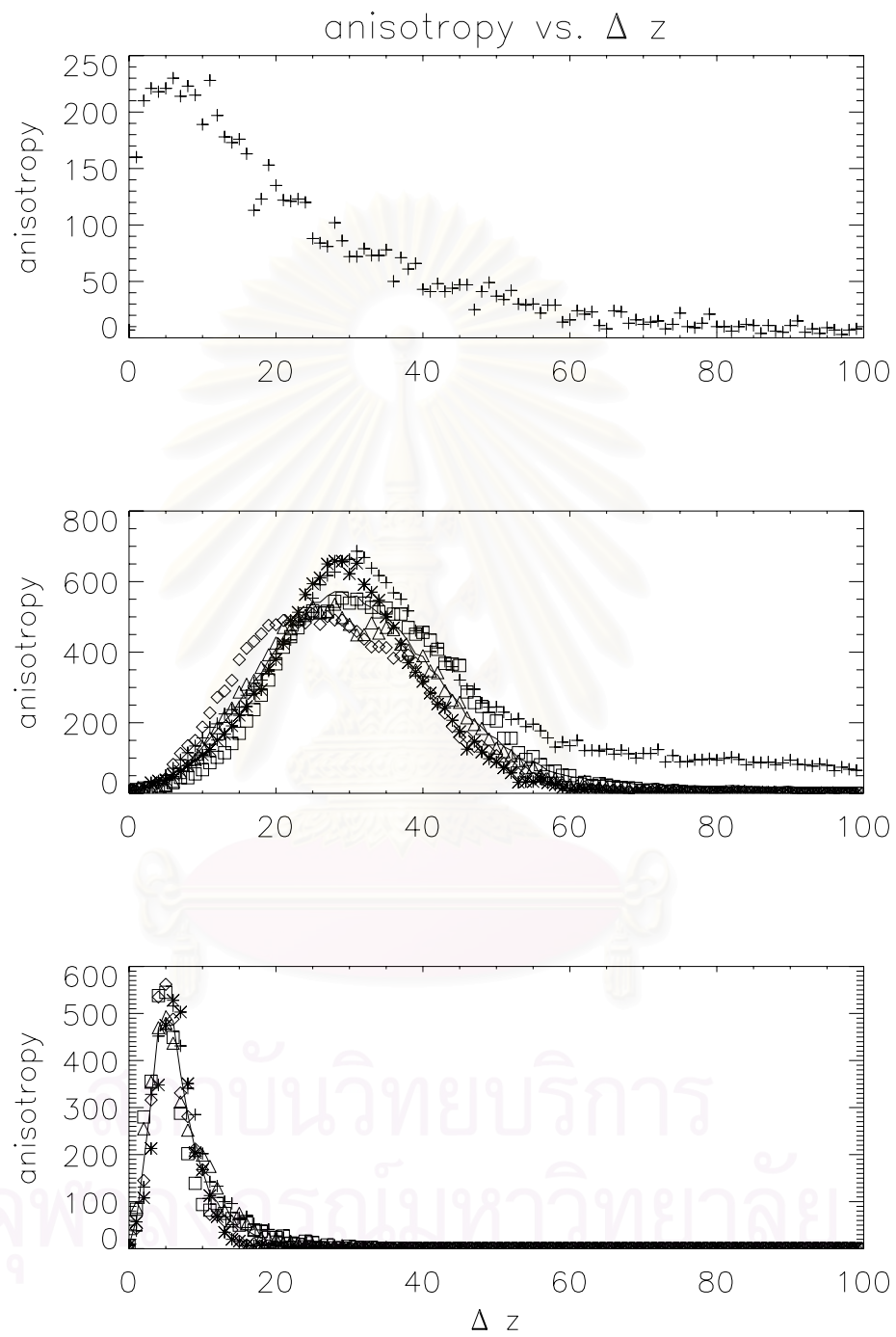


Figure 4.19: Anisotropy number vs.  $\Delta z$  when the parallel length scale is  $0.25\lambda_{\perp}$ .

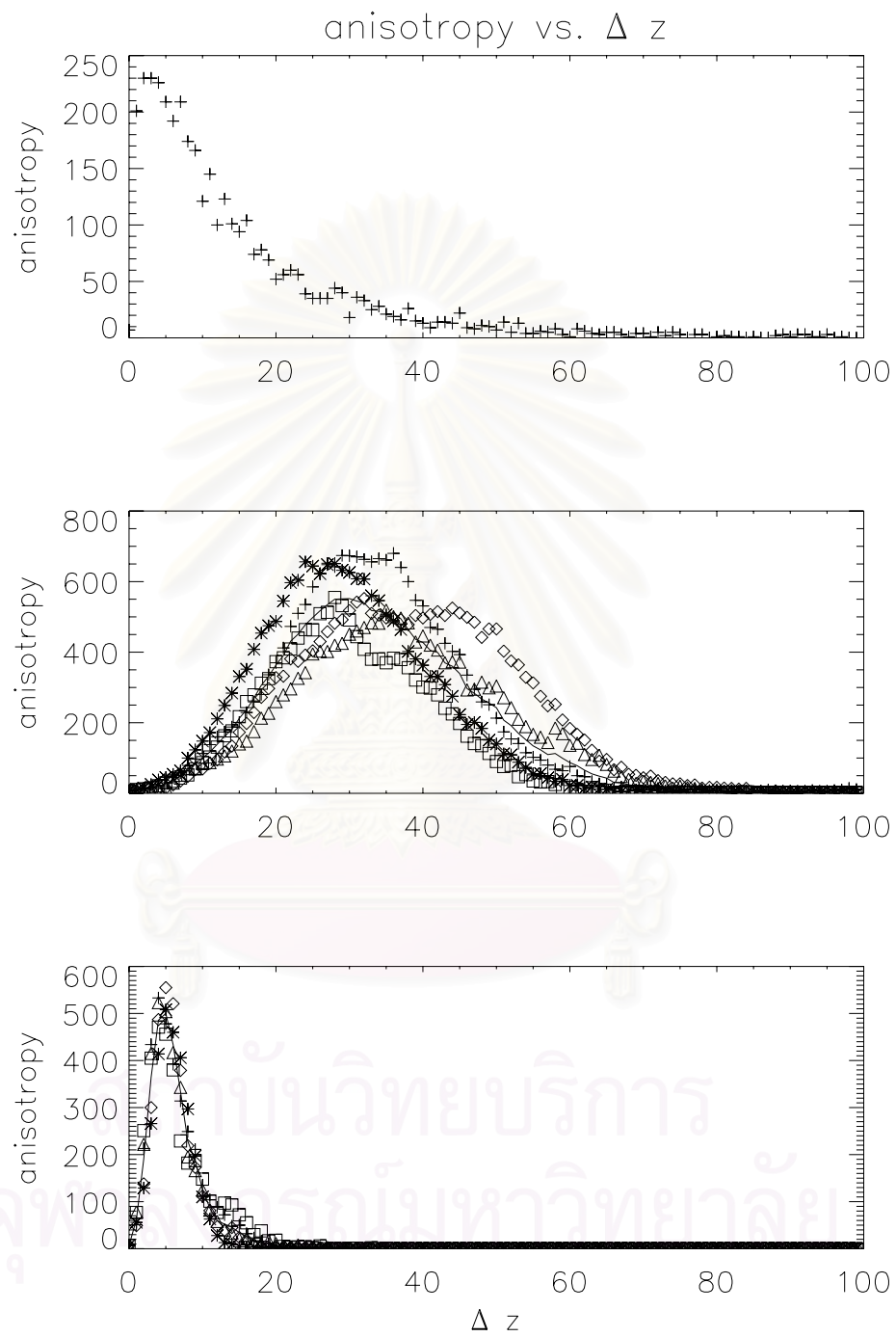


Figure 4.20: Anisotropy number vs.  $\Delta z$  when the parallel length scale is  $0.5\lambda_{\perp}$ .

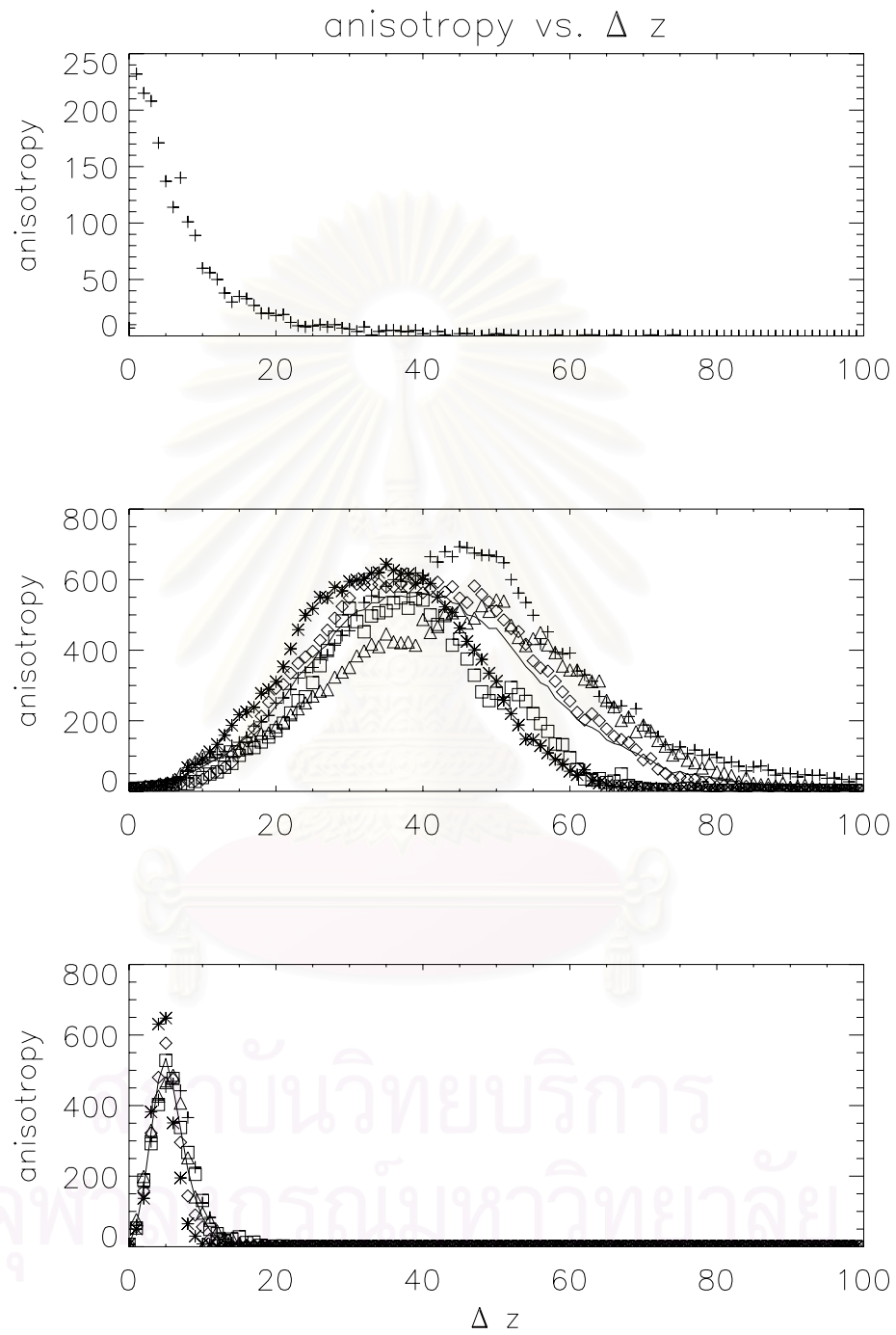


Figure 4.21: Anisotropy number vs.  $\Delta z$  when the parallel length scale is  $1.0\lambda_{\perp}$ .



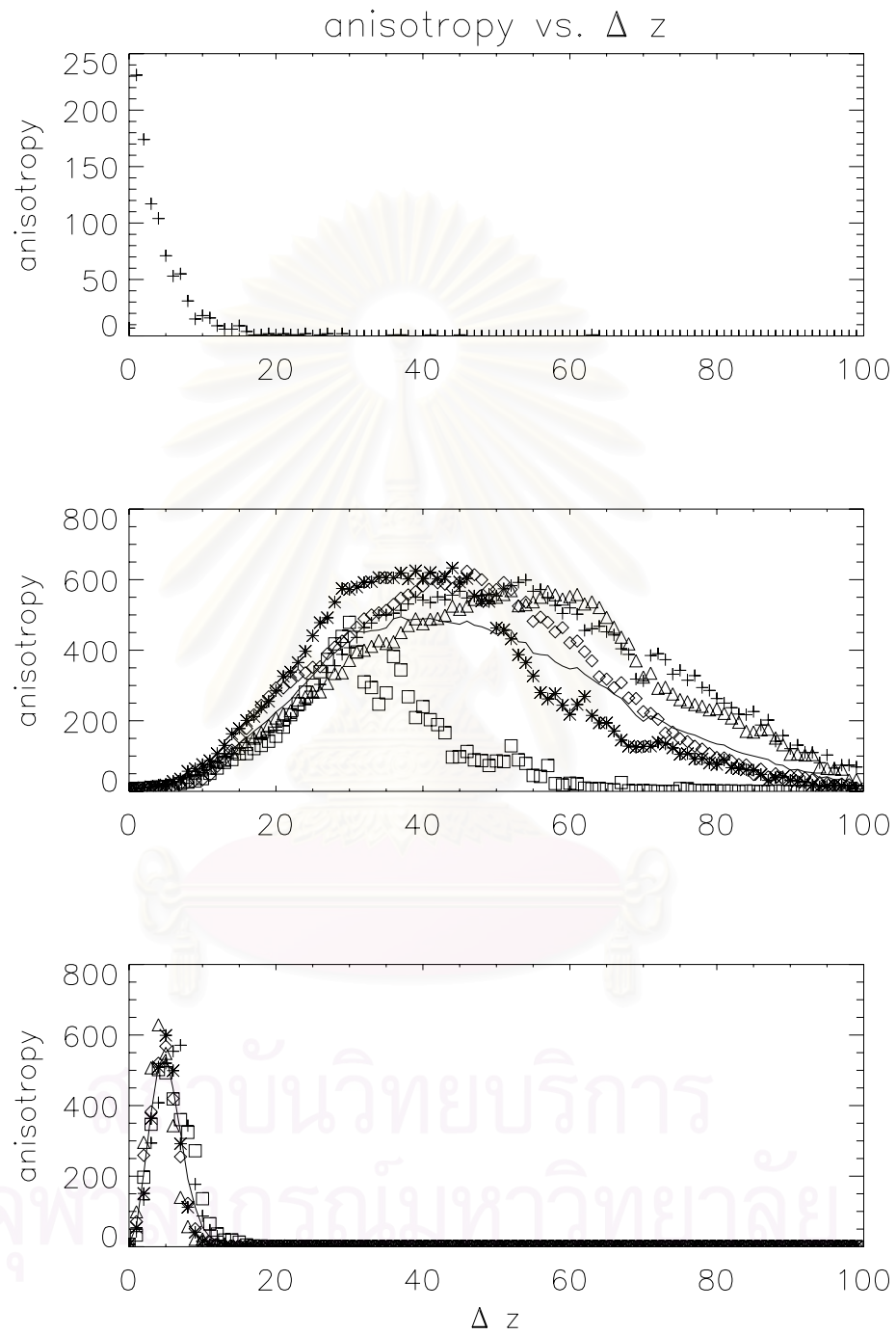


Figure 4.22: Anisotropy number vs.  $\Delta z$  when the parallel length scale is  $2.0\lambda_{\perp}$ .

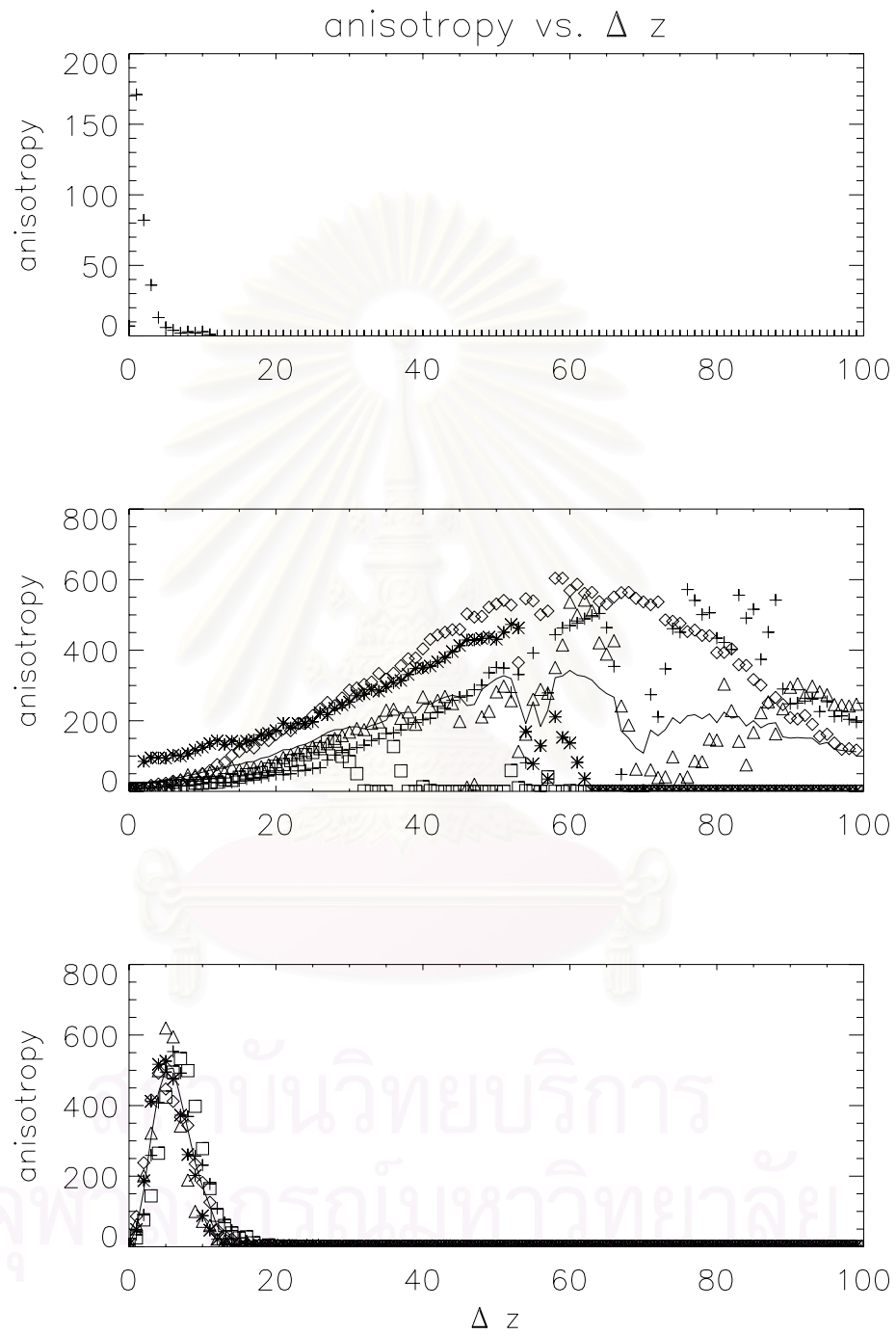


Figure 4.23: Anisotropy number vs.  $\Delta z$  when the parallel length scale is  $5.0\lambda_{\perp}$ .

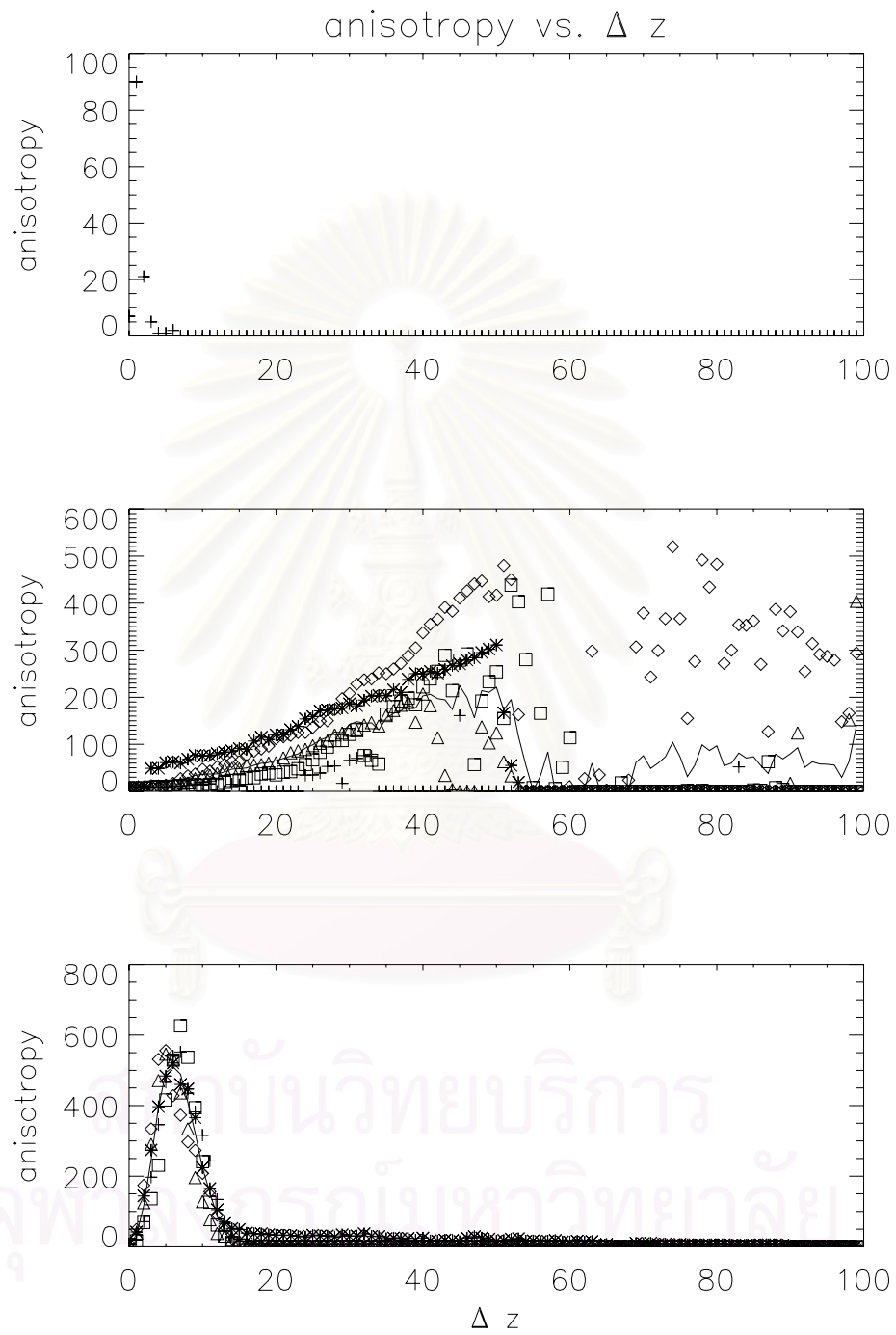


Figure 4.24: Anisotropy number vs.  $\Delta z$  when the parallel length scale is  $10.0\lambda_{\perp}$ .

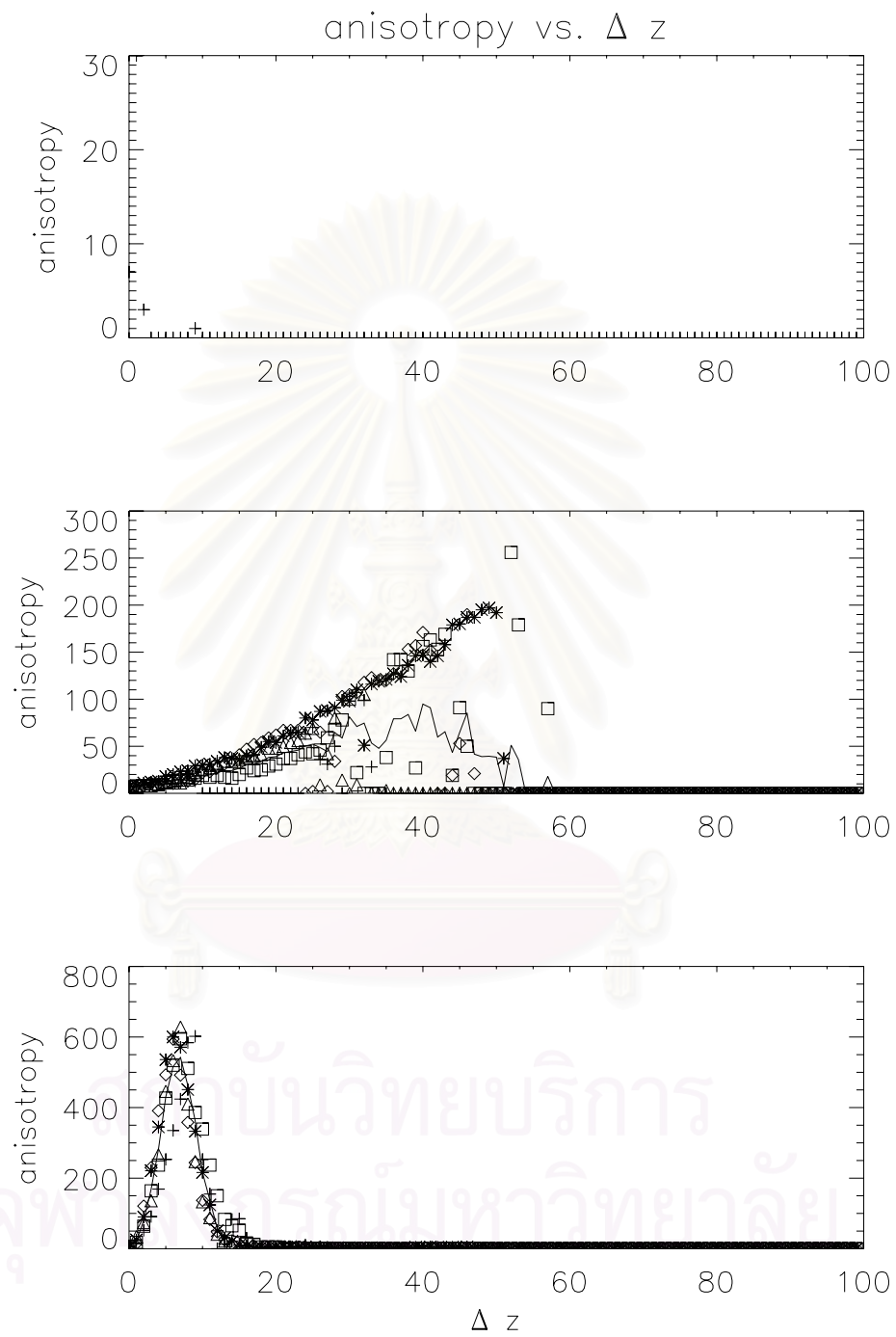


Figure 4.25: Anisotropy number vs.  $\Delta z$  when the parallel length scale is  $20.0\lambda_{\perp}$ .

The last parameter we use to measure the anisotropy is the perpendicular length scale ( $\lambda_{\perp}$ ). As a default value, we set this parameter to 10.0. For the test, we vary this parameter to be 2.0, 5.0, 10.0, 20.0, and 40.0. Because  $\lambda_{\perp}$  is related to the “ultrascale” introduced in Chapter III and the size of the magnetic islands, the group of magnetic field lines generated in the pure slab field with random initial positions in  $z$  is not affected by  $\lambda_{\perp}$  (Figures 4.26 to 4.30).

For the slab+2D field, the larger  $\lambda_{\perp}$  makes the graph of anisotropy have a higher peak, shorter duration, and longer delay to peak. This because if the island is small, the magnetic field lines can spread out easily. Thus, the boundary of the groups of magnetic field lines will not be sharp enough to measure with the Anisotropy Method, so the peak of the graph is lower than for the large islands but with a shorter delay to peak. However, the small magnetic islands can better trap the magnetic field lines, so the peak of anisotropy has a longer duration than for the large magnetic islands. These results are analogous with the SEPs from the gradual flares (and CMEs), where the SEPs are ejected from a wide region on the surface of the Sun. This is confirmed by the control run from Ruffolo et al. (2003).

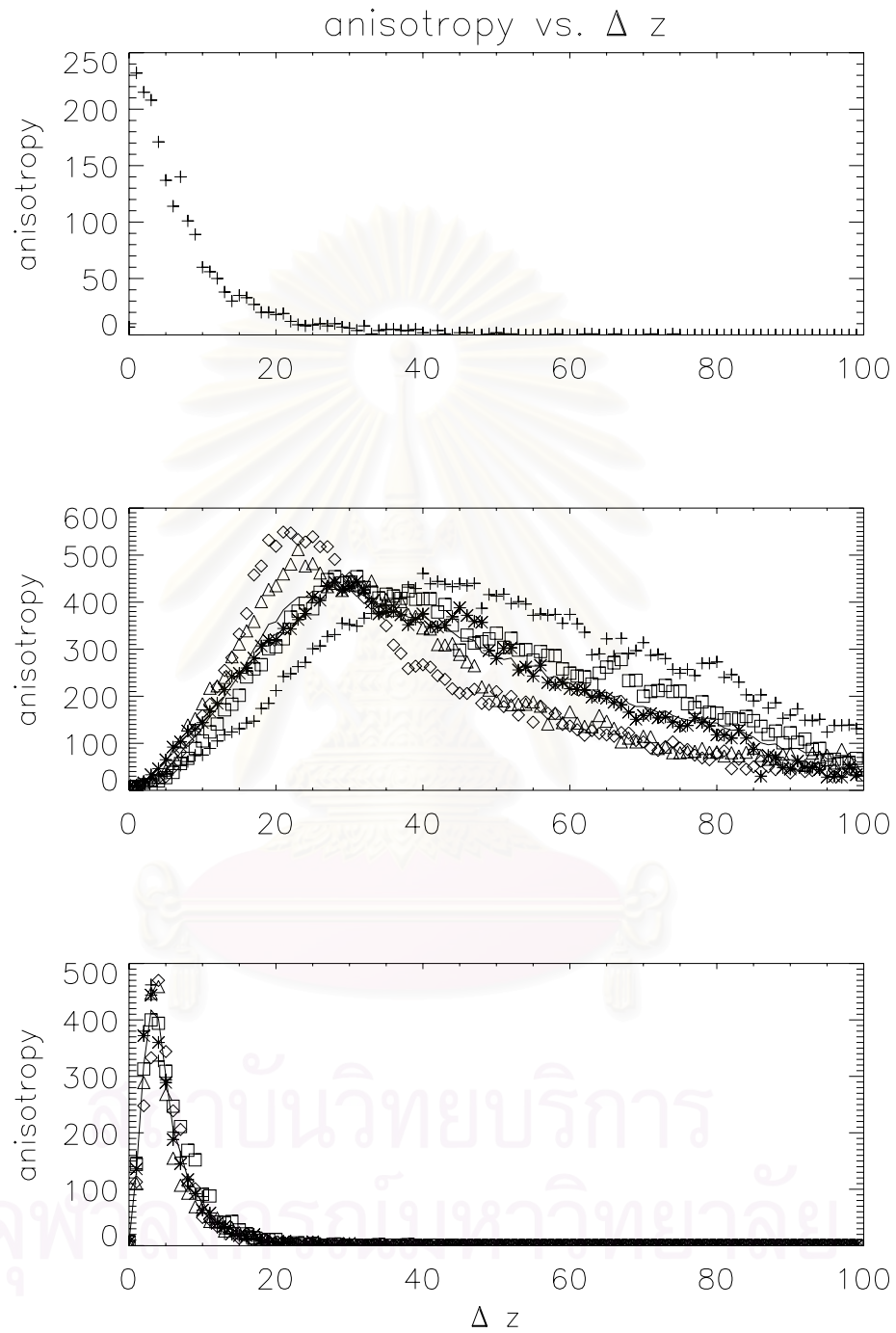


Figure 4.26: Anisotropy number vs.  $\Delta z$  when the perpendicular length scale is 2.0.



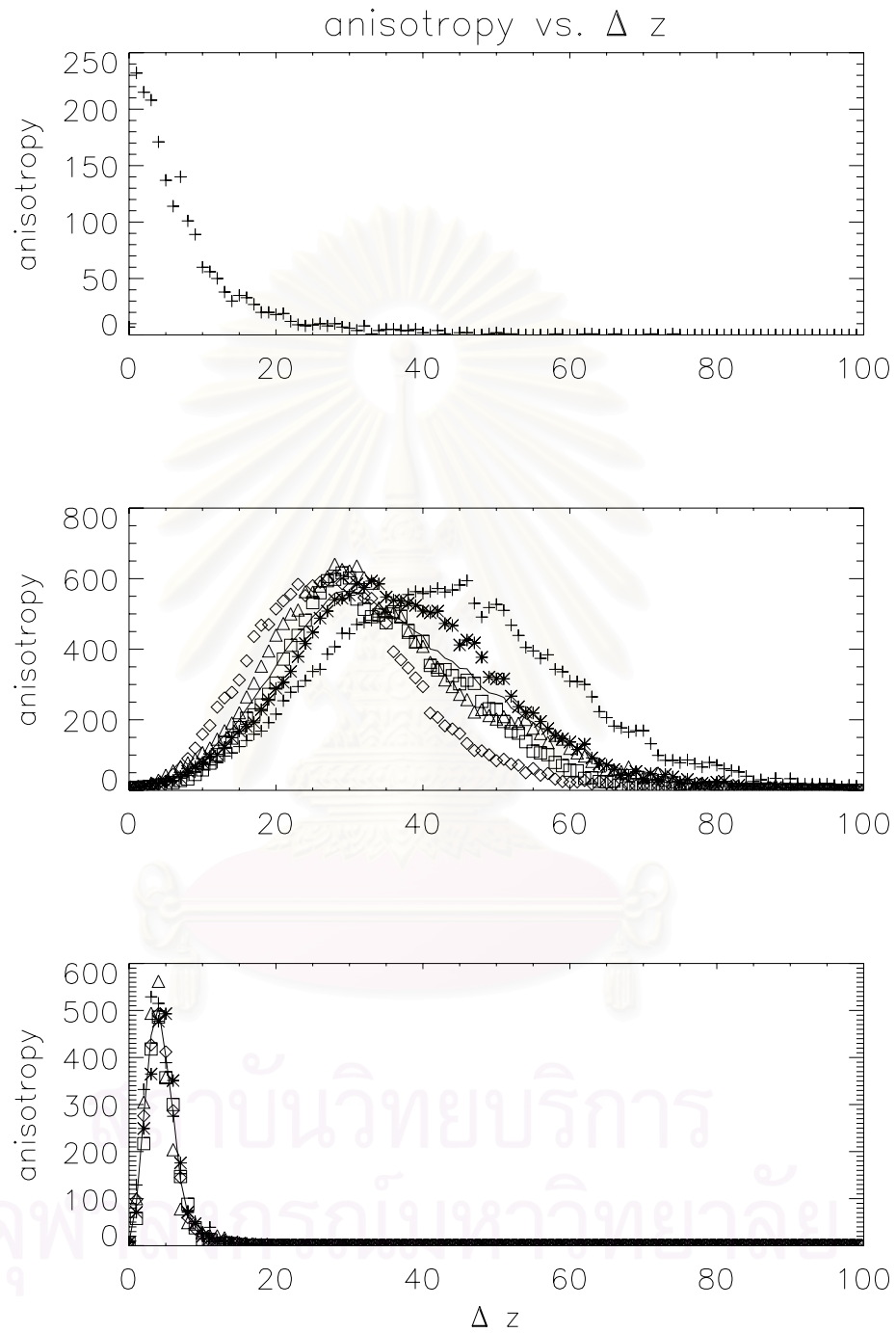


Figure 4.27: Anisotropy number vs.  $\Delta z$  when the perpendicular length scale is 5.0.

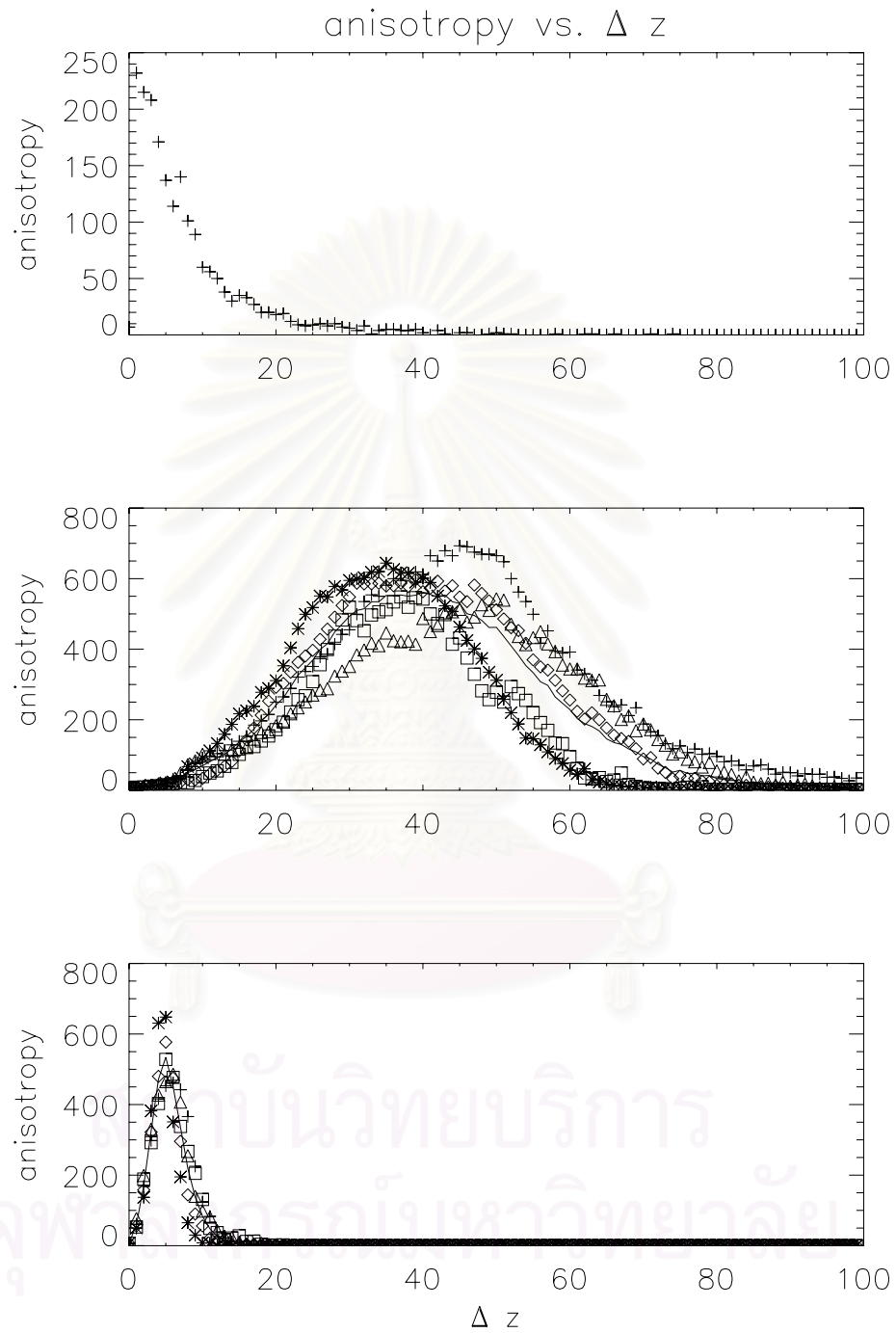


Figure 4.28: Anisotropy number vs.  $\Delta z$  when the perpendicular length scale is 10.0.

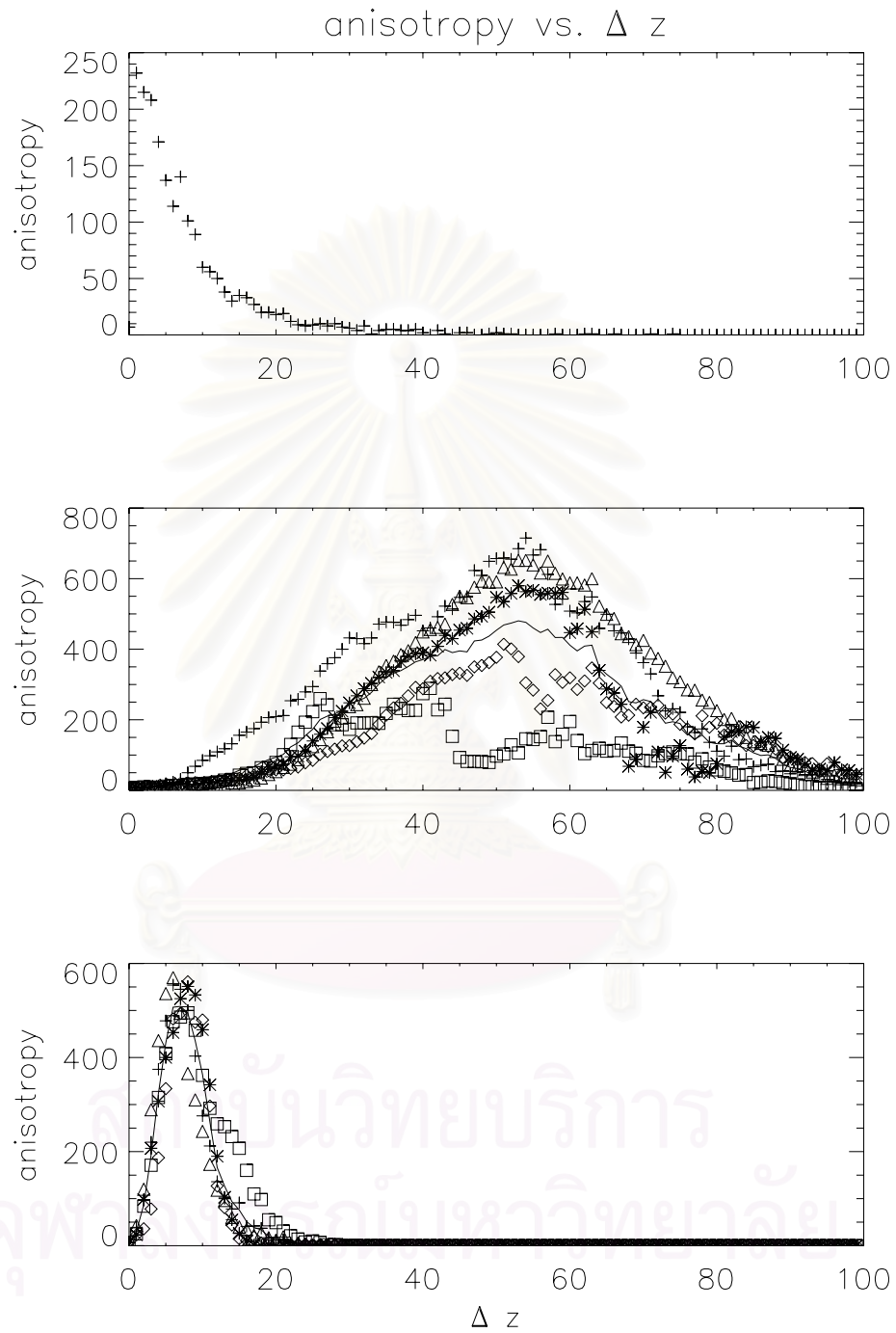


Figure 4.29: Anisotropy number vs.  $\Delta z$  when the perpendicular length scale is 20.0.

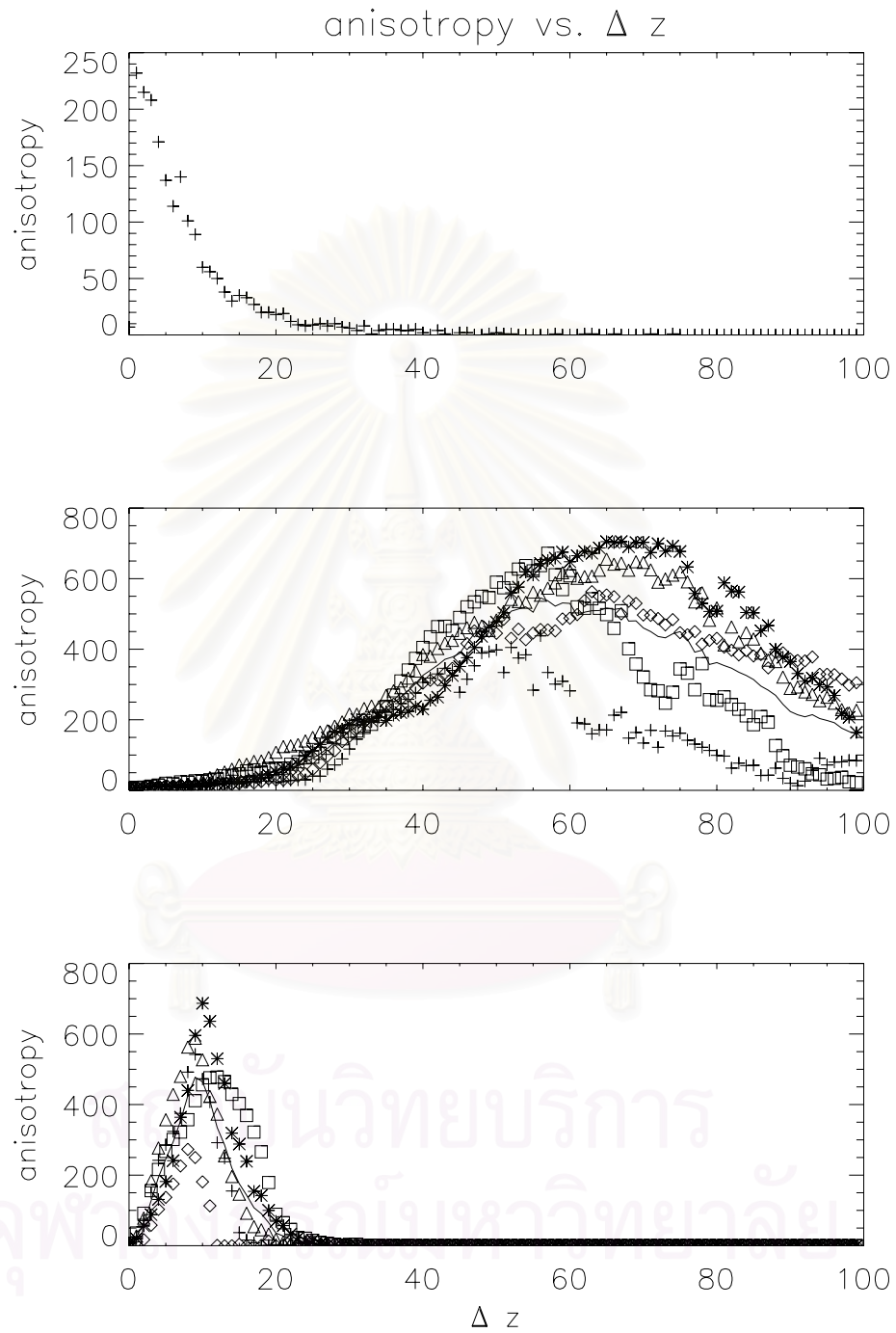


Figure 4.30: Anisotropy number vs.  $\Delta z$  when the perpendicular length scale is 40.0.

### 4.3 Dual Lattice

For the Dual Lattice Method, we also change four variables like in the Anisotropy Method: the ratio between the turbulence fluctuations and the mean field ( $b/B_0$ ), the radius of the initial circle ( $\rho$ ), the parallel scale length ( $\lambda_{\parallel}$ ), and the perpendicular scale length ( $\lambda_{\perp}$ ).

For the fluctuations to the mean field ratio ( $b/B_0$ ), we use the values of this parameter as 0.25, 0.50, 0.75, 1.00, and 2.00. Normally, in the solar wind, the fluctuations to the mean field ratio is  $\approx 0.50$ . The results from the Dual Lattice Method (Figures 4.31 to 4.35) show that if the fluctuations to the mean field ratio increases, we will see the peak of the graph of the dual lattice number vs.  $\Delta z$  at the lower  $\Delta z$ . When the fluctuations increase, the groups of the magnetic field lines separate and diffuse more quickly. Because the separation and diffusion of the groups of magnetic field lines is analogous with the dropouts of the SEPs, we may summarize that the higher fluctuations to the mean field ratio makes the dropouts occur more quickly.

The reason why we show results for 5 different runs is because we want to study whether the average behavior (solid line in the Figures) accurately reflects the behavior of individual runs. In some cases (e.g., in Figure 3.34), we see that results for one run (one set of symbols) is very different from the other. This could be because the initial circle of the group of magnetic field lines was located near an O-point. This makes the group of magnetic field lines expand more than separate at low  $\Delta z$ , so the dual lattice number rises more slowly than the other runs. However, the average can still reflect the behavior of the individual runs.

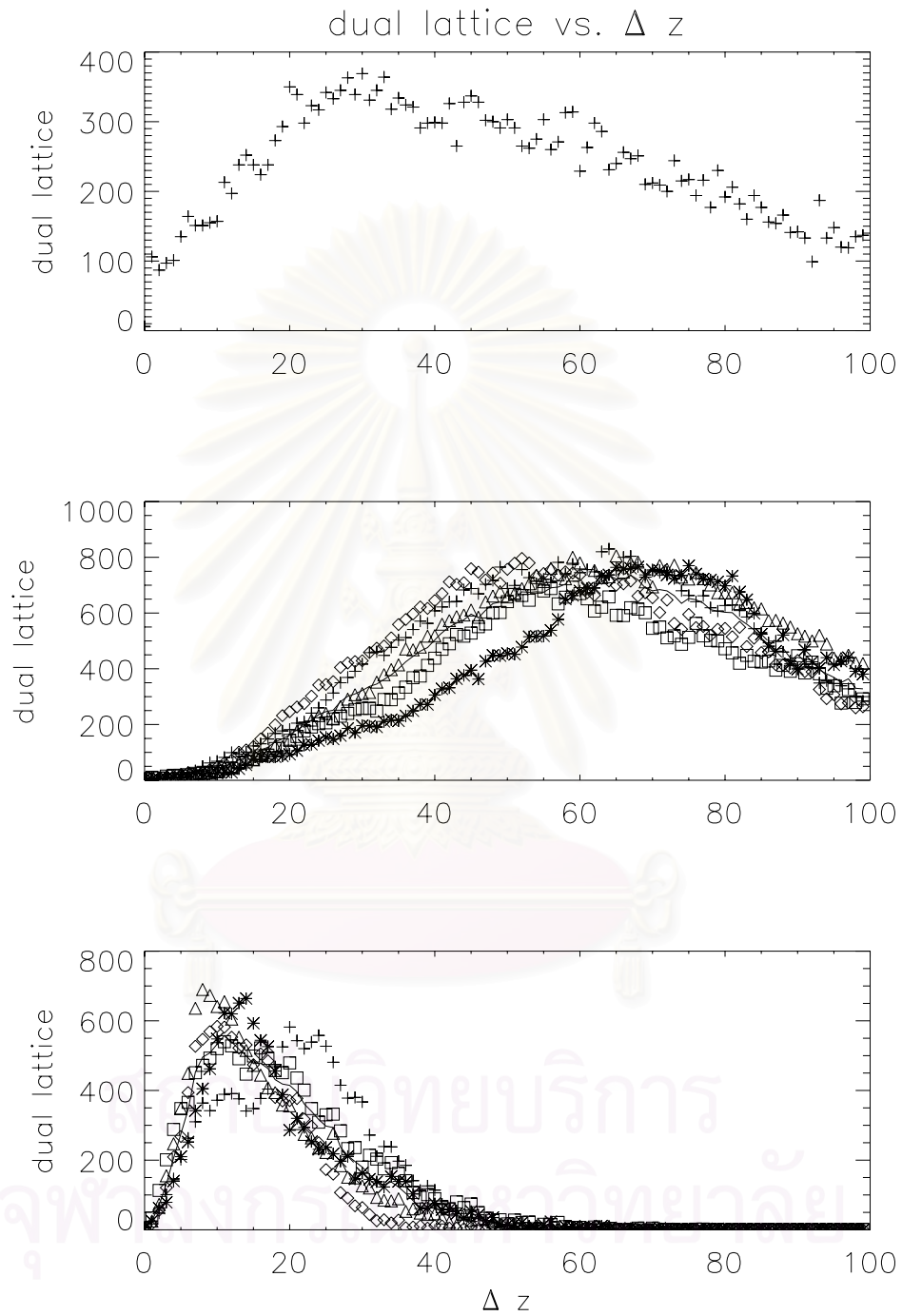


Figure 4.31: Dual lattice number vs.  $\Delta z$  when the turbulence fluctuation to mean field ratio is 0.25.



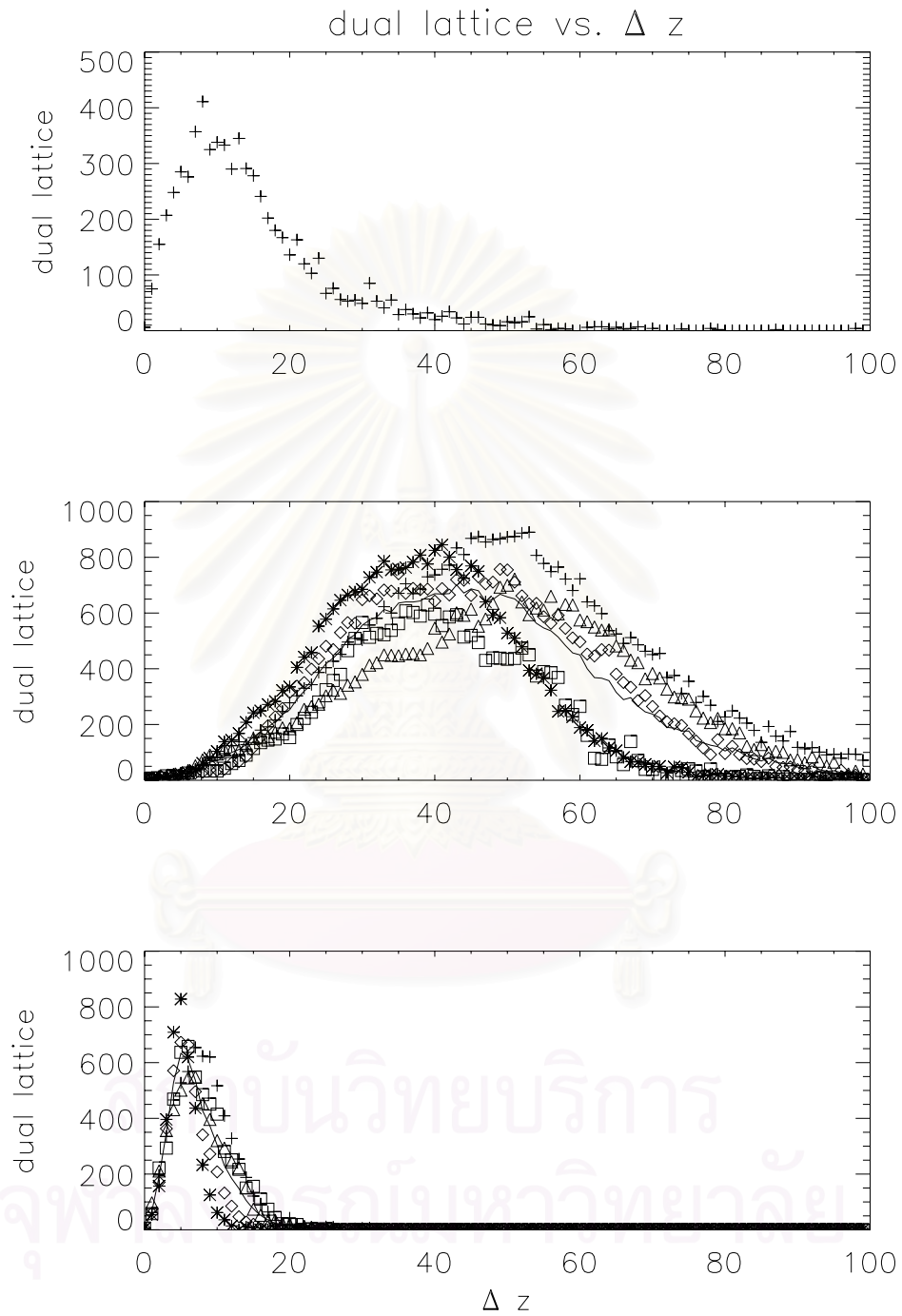


Figure 4.32: Dual lattice number vs.  $\Delta z$  when the turbulence fluctuation to mean field ratio is 0.50.

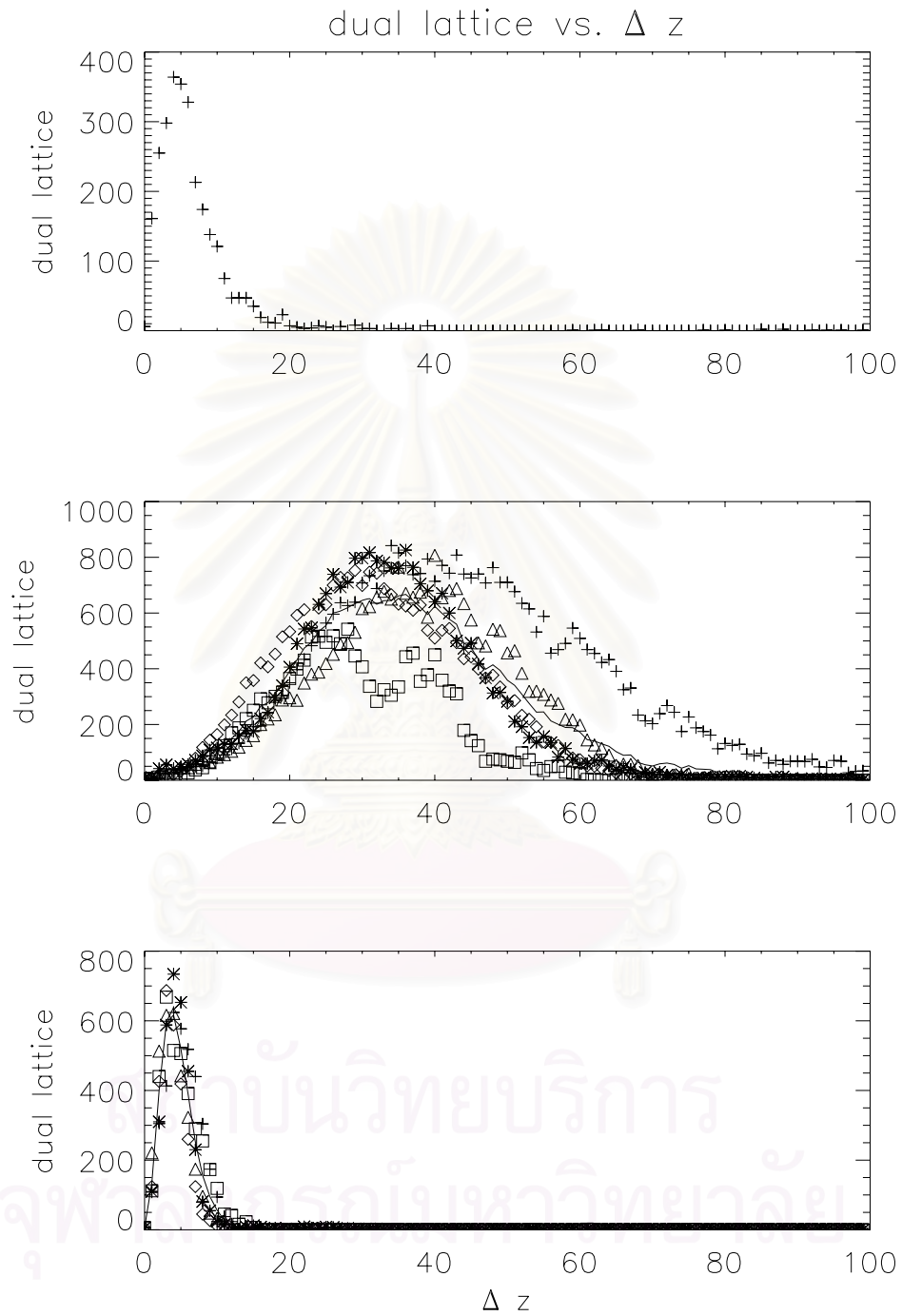


Figure 4.33: Dual lattice number vs.  $\Delta z$  when the turbulence fluctuation to mean field ratio is 0.75.

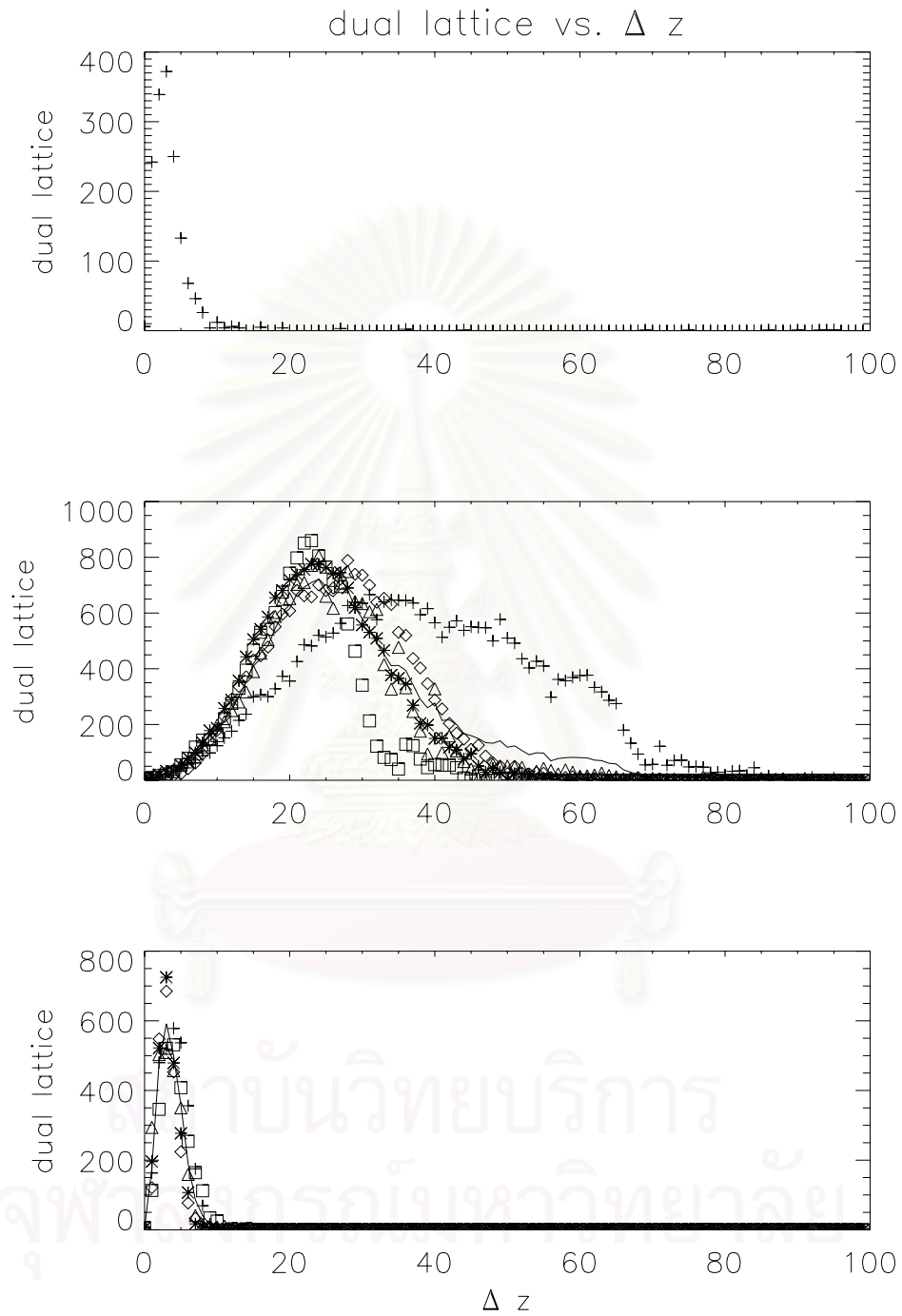


Figure 4.34: Dual lattice number vs.  $\Delta z$  when the turbulence fluctuation to mean field ratio is 1.00.

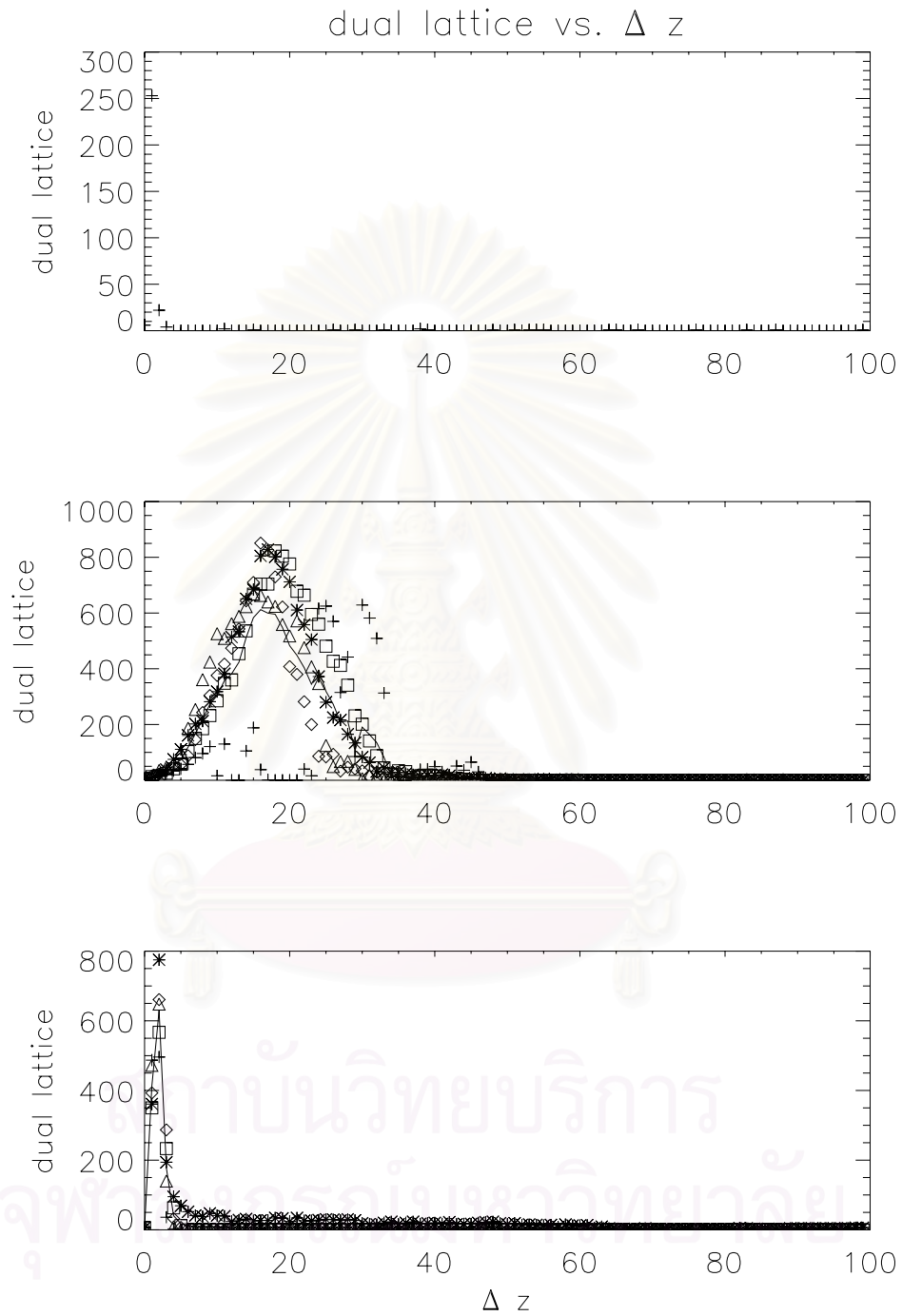


Figure 4.35: Dual lattice number vs.  $\Delta z$  when the turbulence fluctuation to mean field ratio is 2.00.

For the size of the initial circle, we use the radius ( $\rho$ ) of the initial circle as 0.5, 1.0, 2.0, 4.0, 8.0, 16.0, and 32.0 in units of  $\lambda_{\perp}$ . The results from  $\rho = 32\lambda_{\perp}$  are different from the other  $\rho$  values. For  $\rho = 32\lambda_{\perp}$ , the dual lattice number does not rise but rather falls immediately (Fig. 4.42). Because of the large initial circle, the group of magnetic field lines can spread throughout space easily. Thus, the behavior of the magnetic field lines from the large initial circle is like the control run in Ruffolo et al. (2003).

Now we consider the other values of the initial circle size. For the pure slab turbulence with random initial positions in  $z$ , by considering the dual lattice number at  $\Delta z = 0$ , we found that when  $\rho$  increases the dual lattice number increases, too (Figures 4.36 to 4.41). Over higher  $\Delta z$ , the dual lattice number rises until peak and falls with the same characteristics for all initial circle sizes. In this case, the dual lattice number rises because the field line separation makes the group of magnetic field lines expand and the dual lattice number falls because the magnetic field lines spread throughout space.

When the energy ratio between the slab and 2D turbulence is 99:1 and 20:80 with the initial positions of the magnetic field lines at  $z = 0$ , the graphs of the dual lattice number for all of the initial circle sizes have a similar amplitude and width for each energy ratio. However, when increasing the radius of the initial circle, the dual lattice number rises more quickly, because the rate of the separation of the magnetic field line depends on  $\lambda_{\parallel}$  and  $\lambda_{\perp}$ . Thus, for the same value of  $\lambda_{\parallel}$  and  $\lambda_{\perp}$ , the field line separation rate and the trapping duration are similar for small  $\rho$ . By the way, the graphs of the dual lattice number for the energy ratio between the slab and 2D turbulence of 20:80 rise faster but have a smaller amplitude than the graphs of the dual lattice number for the energy ratio

between the slab and 2D turbulence of 99:1. This is because when 2D turbulence increases a group of magnetic field lines separates and diffuses with a higher rate.



สถาบันวิทยบริการ  
จุฬาลงกรณ์มหาวิทยาลัย

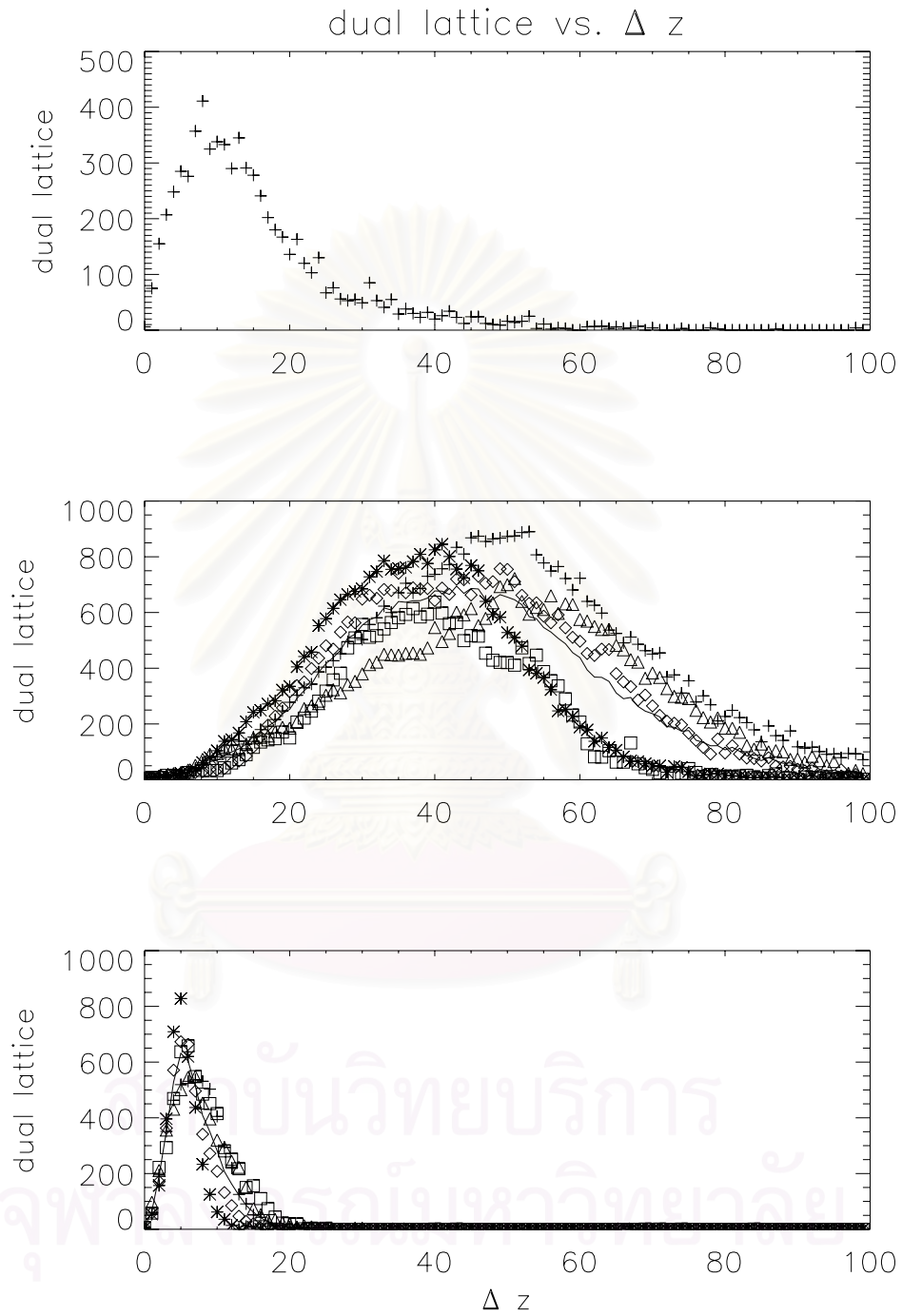


Figure 4.36: Dual lattice number vs.  $\Delta z$  when the radius of the initial circle is  $0.5\lambda_{\perp}$ .



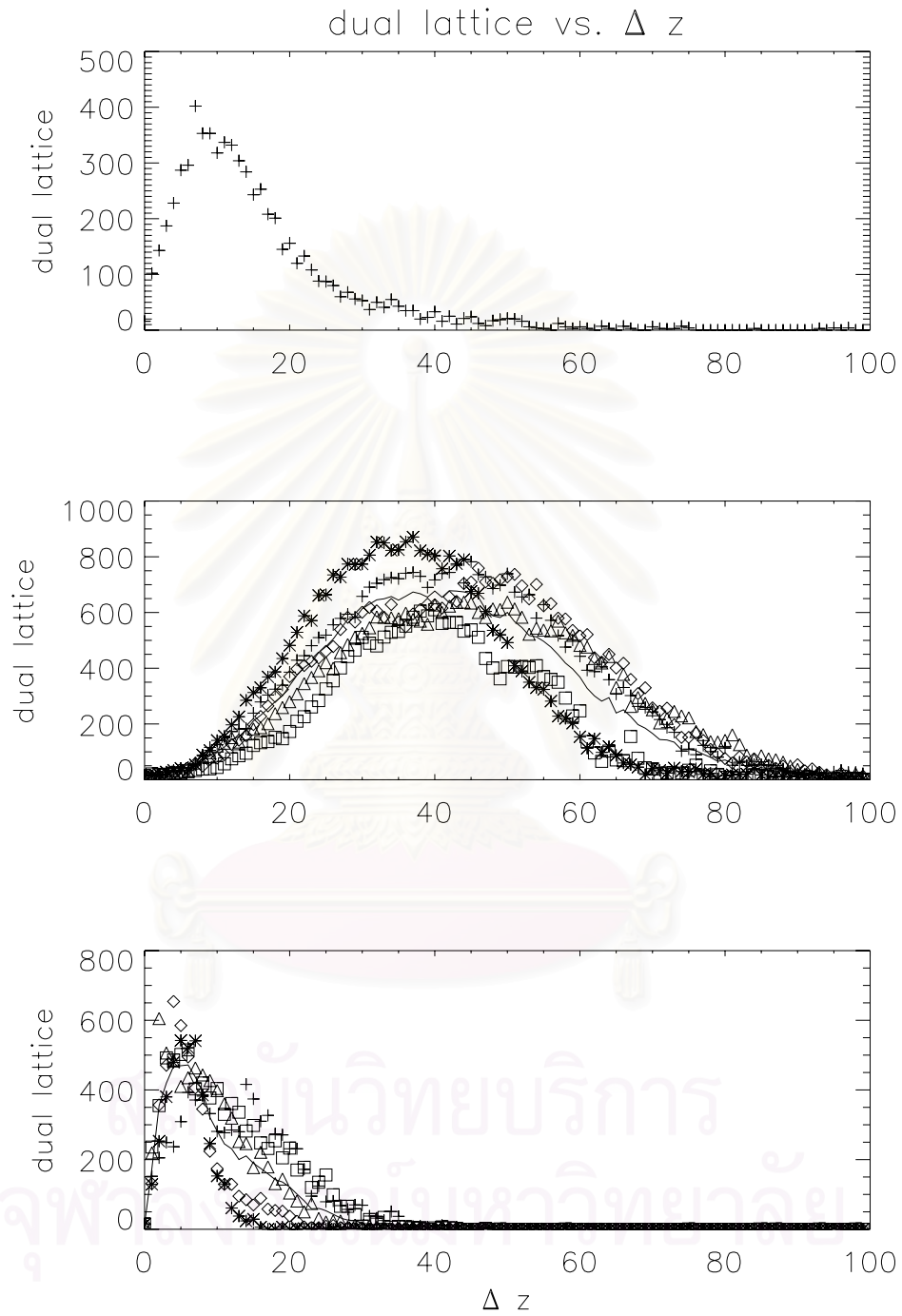


Figure 4.37: Dual lattice number vs.  $\Delta z$  when the radius of the initial circle is  $1.0\lambda_{\perp}$ .

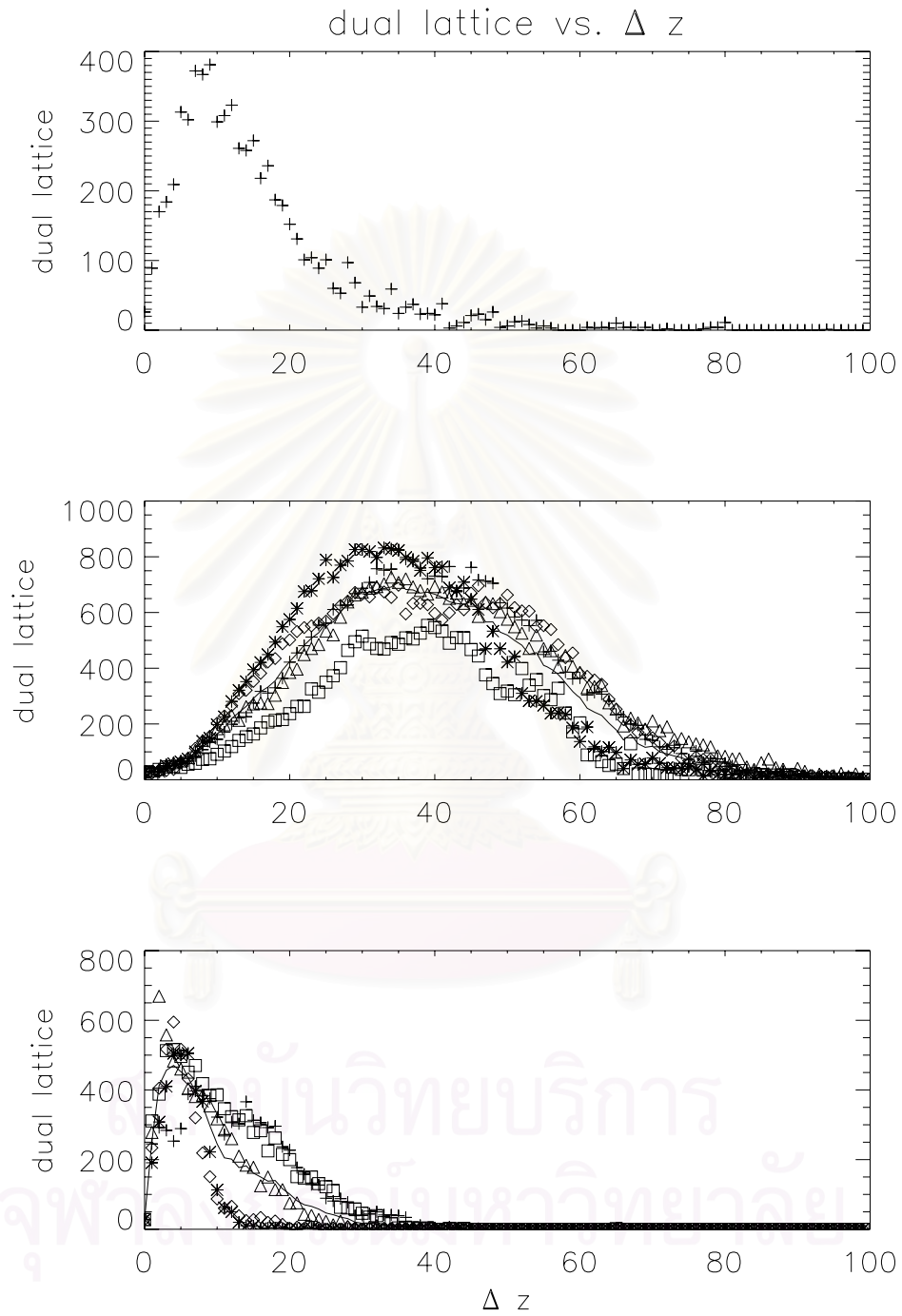


Figure 4.38: Dual lattice number vs.  $\Delta z$  when the radius of the initial circle is  $2.0\lambda_{\perp}$ .

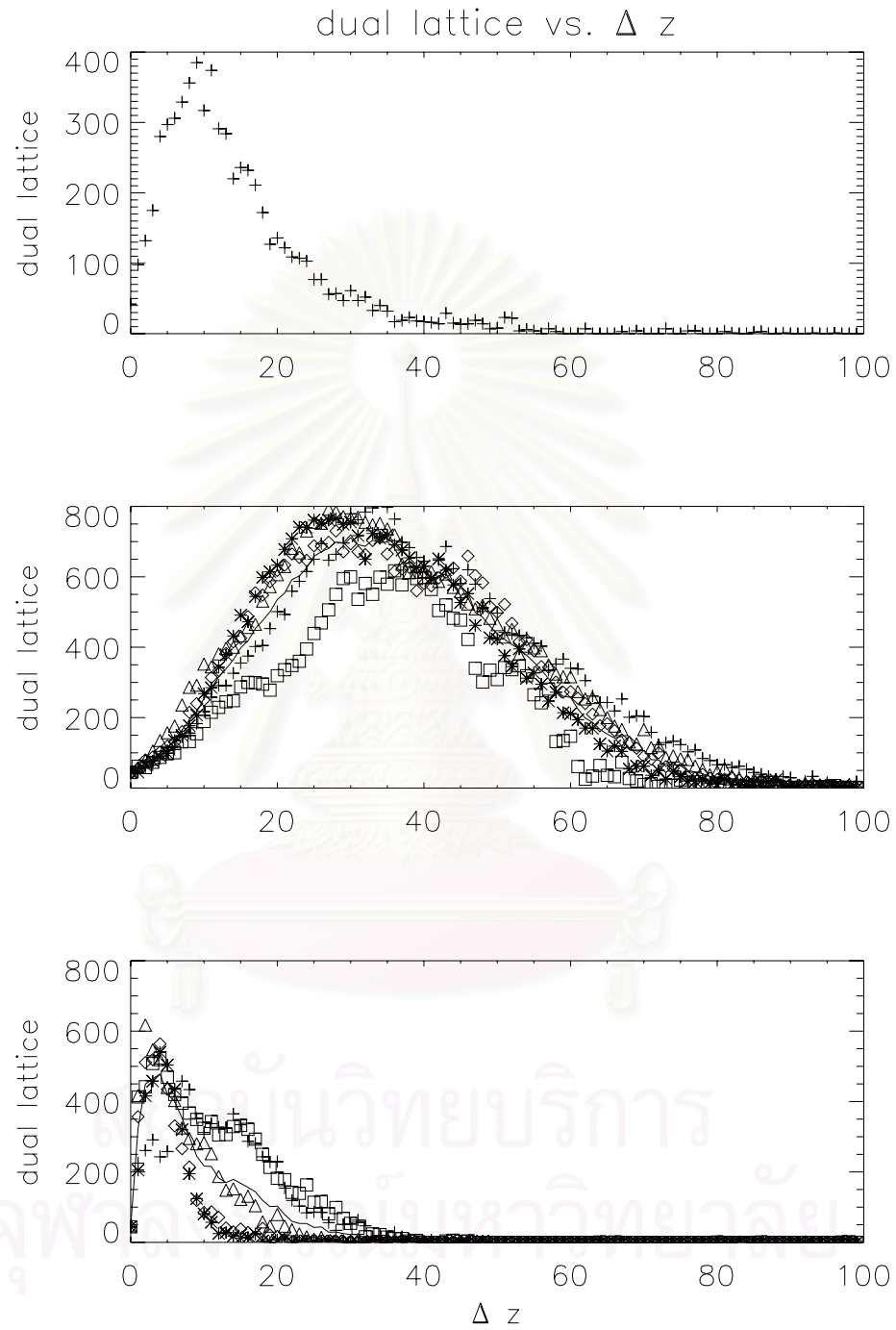


Figure 4.39: Dual lattice number vs.  $\Delta z$  when the radius of the initial circle is  $4.0\lambda_{\perp}$ .

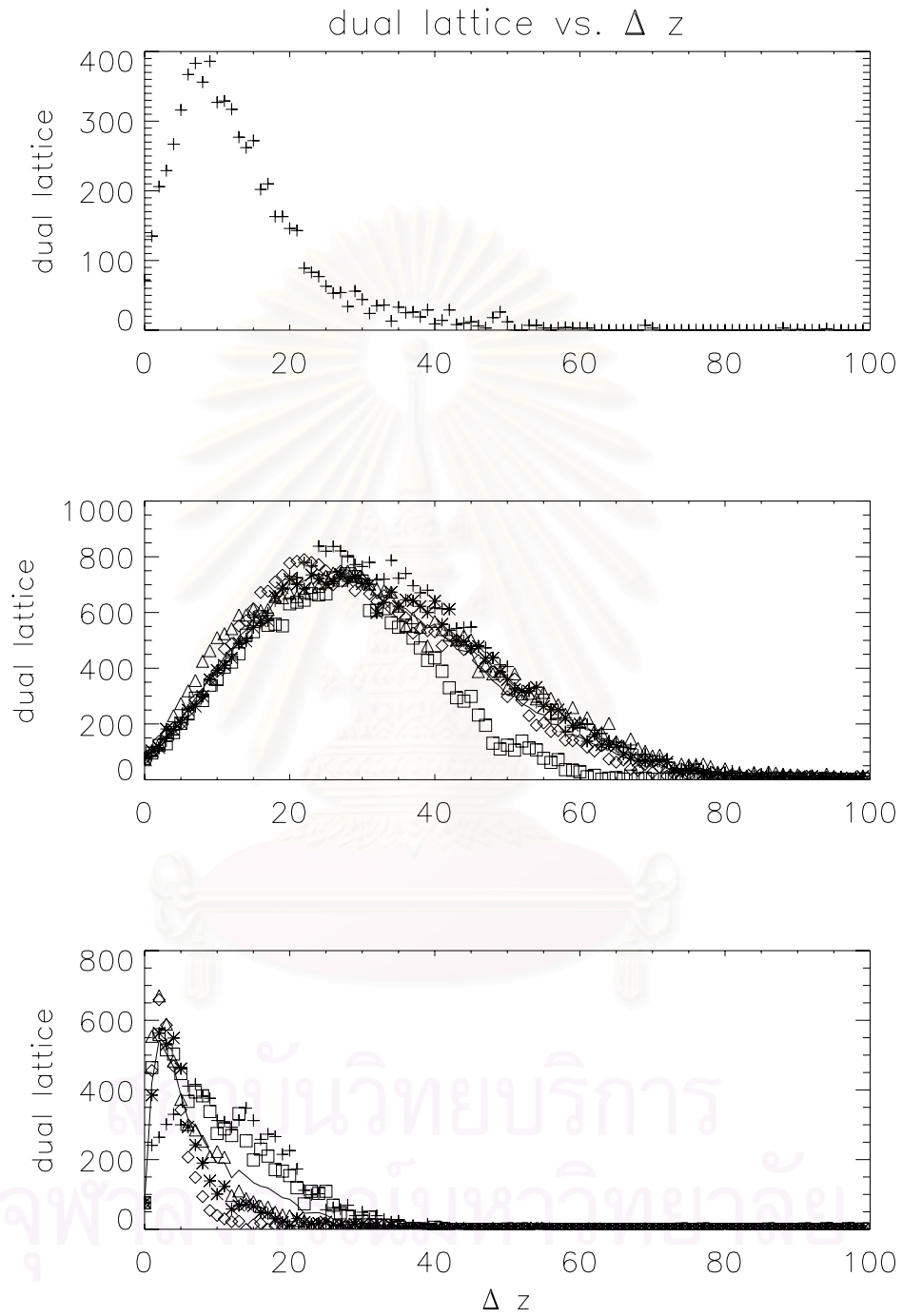


Figure 4.40: Dual lattice number vs.  $\Delta z$  when the radius of the initial circle is  $8.0\lambda_{\perp}$ .

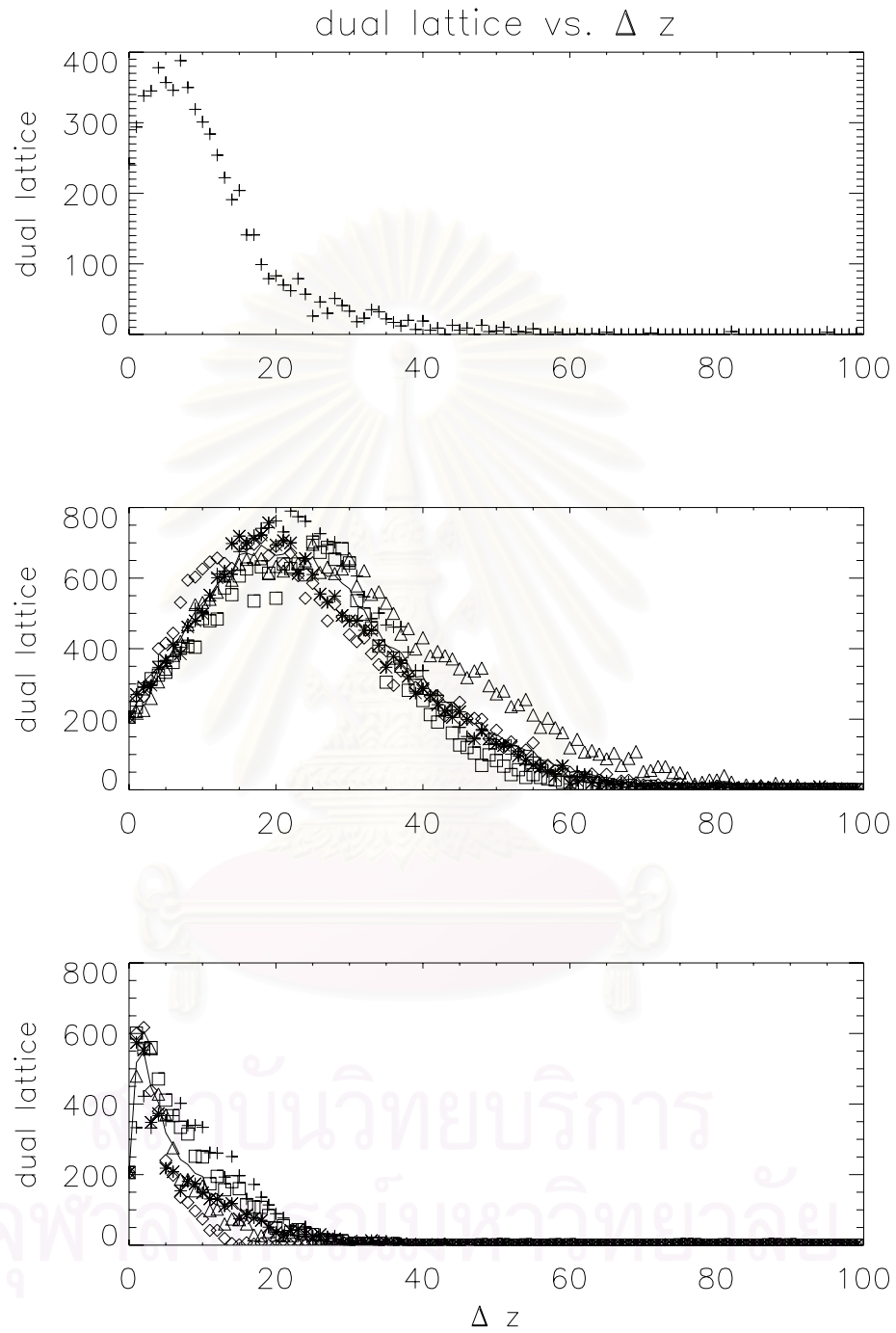


Figure 4.41: Dual lattice number vs.  $\Delta z$  when the radius of the initial circle is  $16.0\lambda_{\perp}$ .

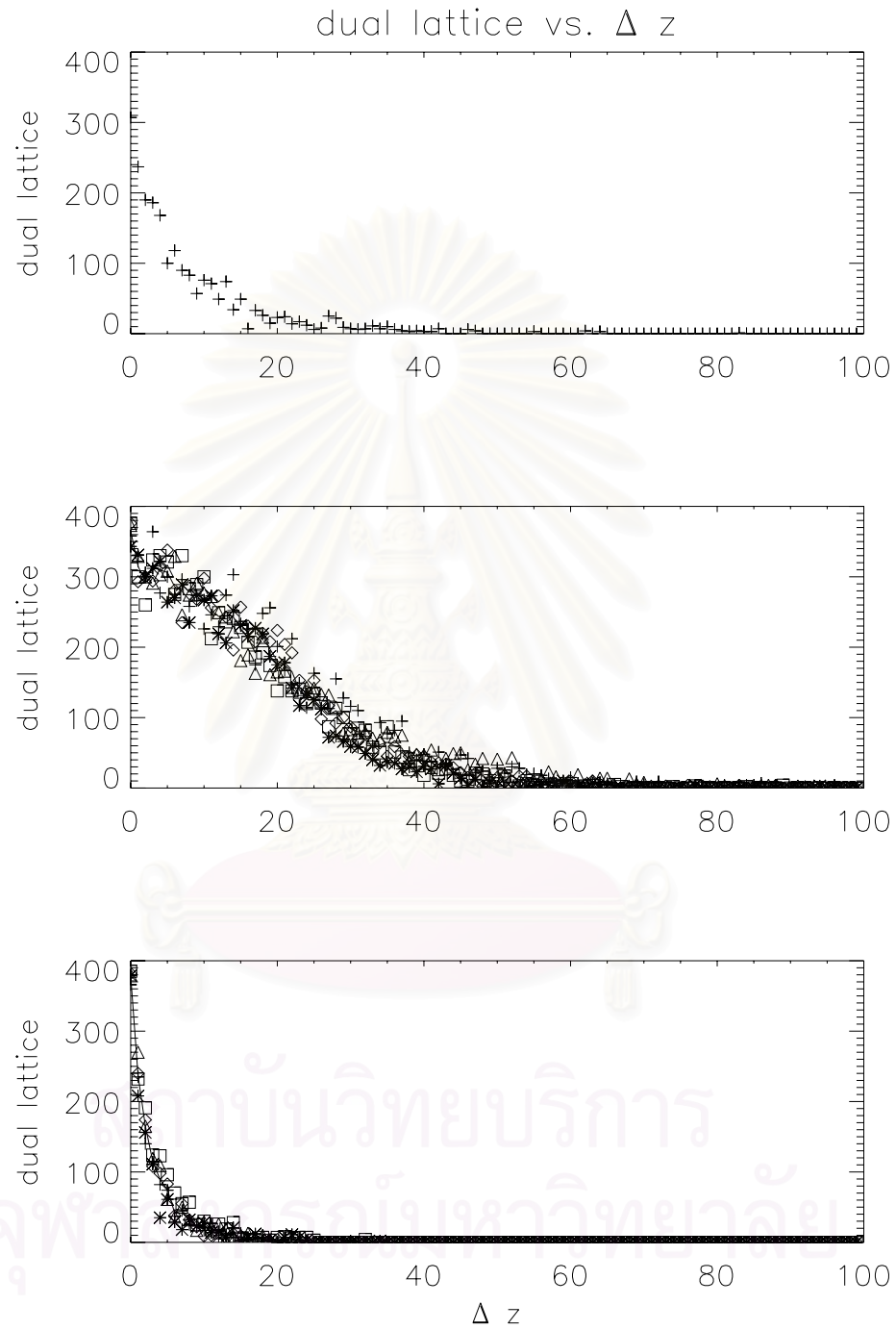


Figure 4.42: Dual lattice number vs.  $\Delta z$  when the radius of the initial circle is  $32.0\lambda_{\perp}$ .

For the parallel length scale ( $\lambda_{\parallel}$ ), we use the values of this parameter as 0.25, 0.50, 1.00, 2.00, 5.00, 10.00, and 20.00 in units of  $\lambda_{\perp}$ . This parameter is related to the slab correlation length  $\ell_c$  by  $\ell_c = 0.747\lambda_{\parallel}$  (Chuychai 2005). A high  $\lambda_{\parallel}$  makes the magnetic field lines separate at a long distance from the initial position while the low  $\lambda_{\parallel}$  makes the magnetic field lines separate at a shorter distance from the initial position. From the graphs of the dual lattice number (Figures 4.43 to 4.49), for the pure slab field with random initial  $z$ , the diffusion coefficient of field line separation ( $D_{sep}$ ) depends on  $\lambda_{\parallel}$  because  $D_{sep} = 2D_{slab}$  and  $D_{slab} \propto \lambda_{\parallel}$ . In the case when the energy ratio of slab:2D turbulence is 20:80,  $D_{sep}$  does not depend much on  $\lambda_{\parallel}$ . For a ratio of 99:1  $D_{sep} \propto 1/\lambda_{\parallel}$  because  $D_{sep} = 2D_{2D}^2/D_{\perp}$  and  $D_{\perp} \propto D_{slab}$  (Ruffolo et al. 2004).

Note that when the energy ratio of the slab turbulence to the 2D turbulence is 99:1, for a high parallel length scale ( $\lambda_{\parallel} = 5.0, 10.0, 20.0$ ), and at high  $\Delta z$ , some magnetic field lines reach the limit of the simulation box size, so the dual lattice number is case dependent and often becomes zero.



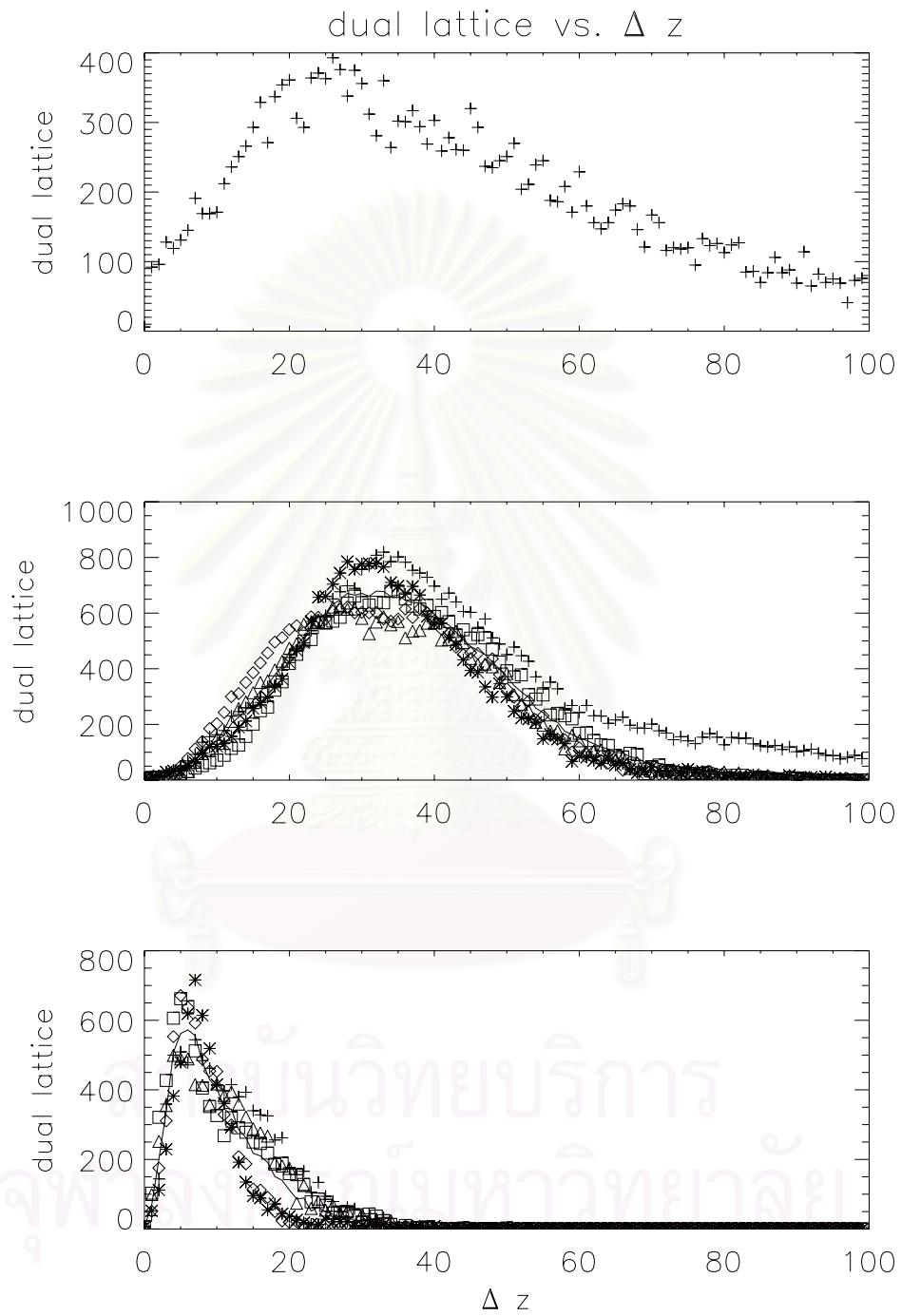


Figure 4.43: Dual lattice number vs.  $\Delta z$  when the parallel length scale is  $0.25\lambda_{\perp}$ .

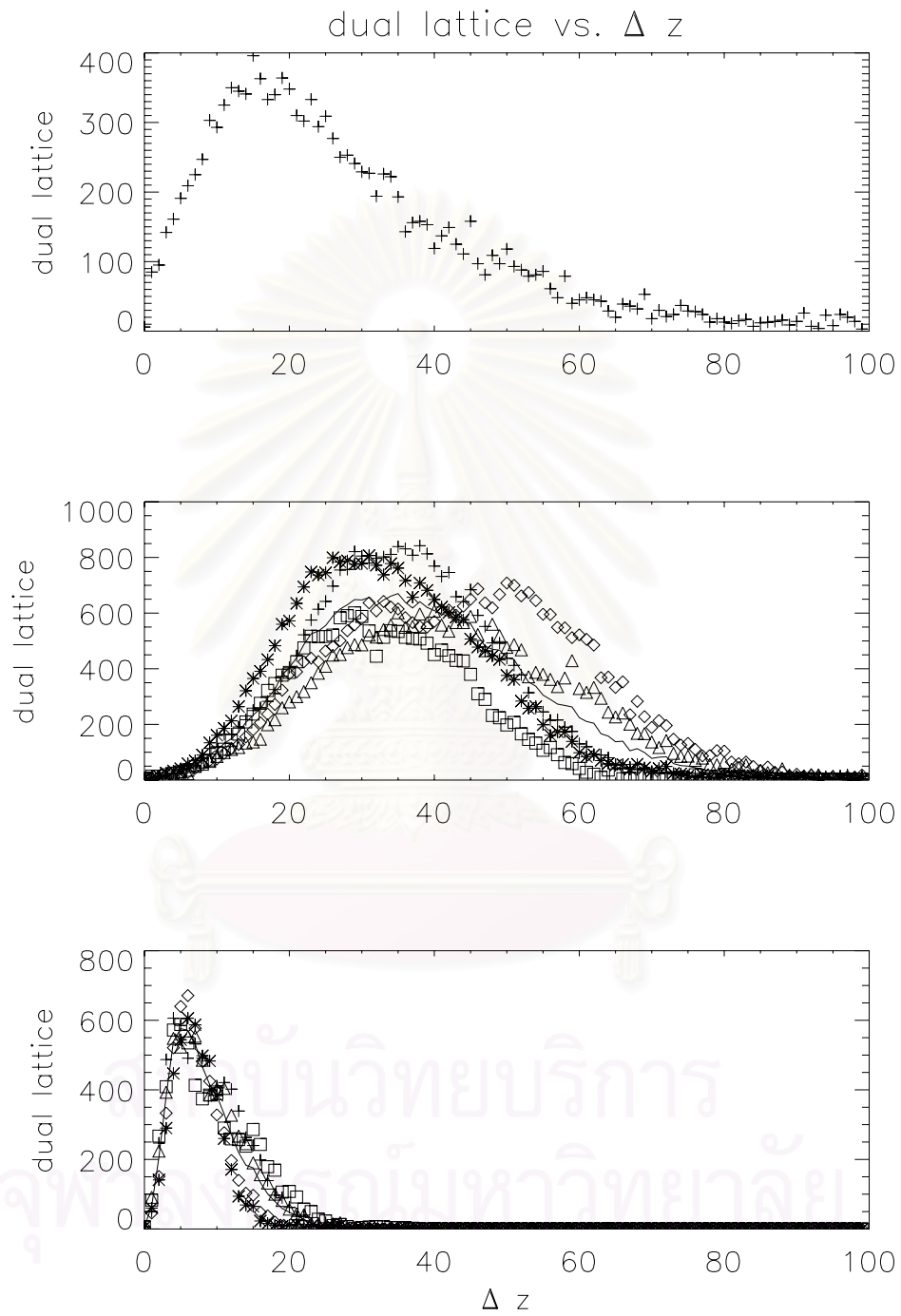


Figure 4.44: Dual lattice number vs.  $\Delta z$  when the parallel length scale is  $0.5\lambda_{\perp}$ .

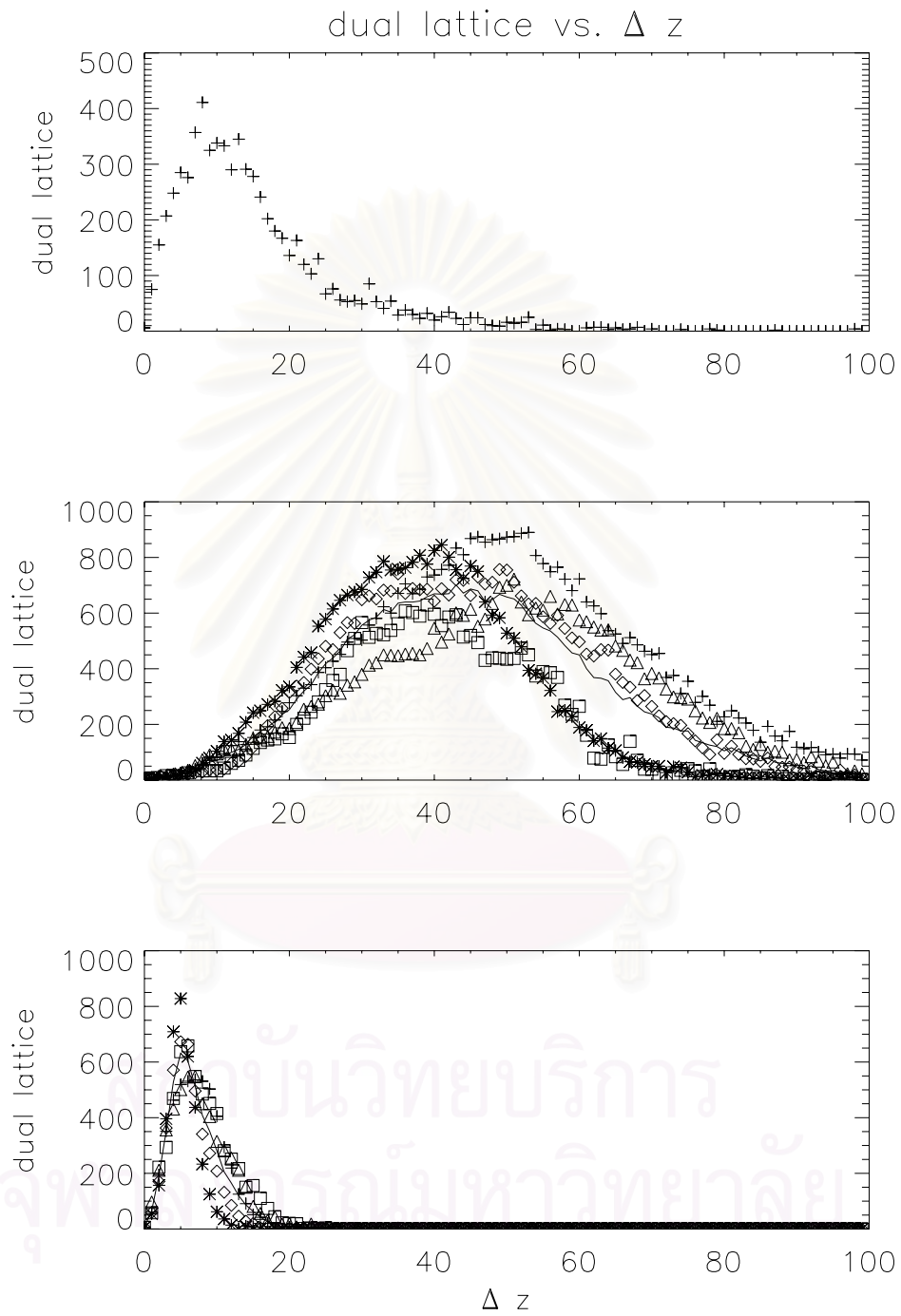


Figure 4.45: Dual lattice number vs.  $\Delta z$  when the parallel length scale is  $1.0\lambda_{\perp}$ .

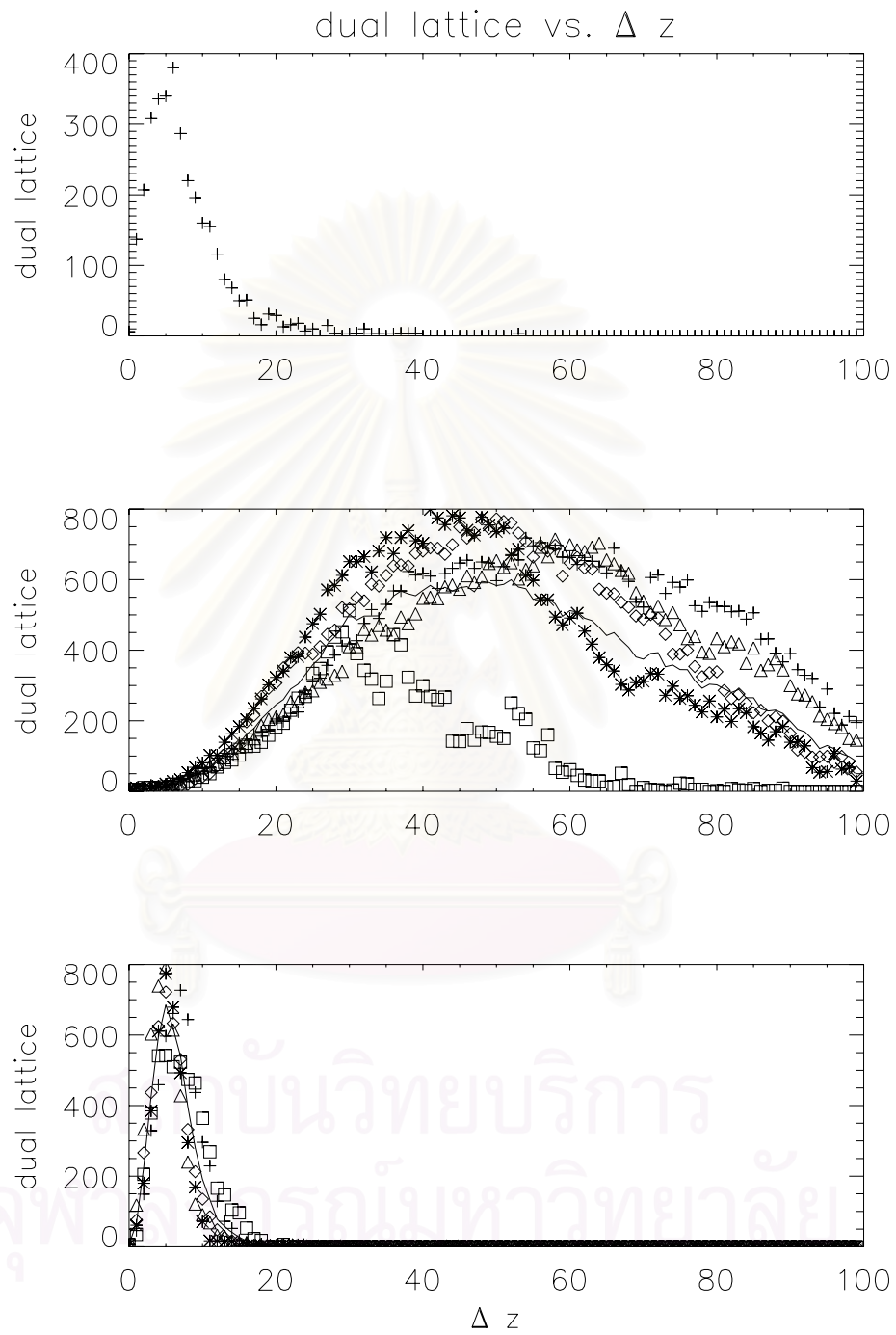


Figure 4.46: Dual lattice number vs.  $\Delta z$  when the parallel length scale is  $2.0\lambda_{\perp}$ .

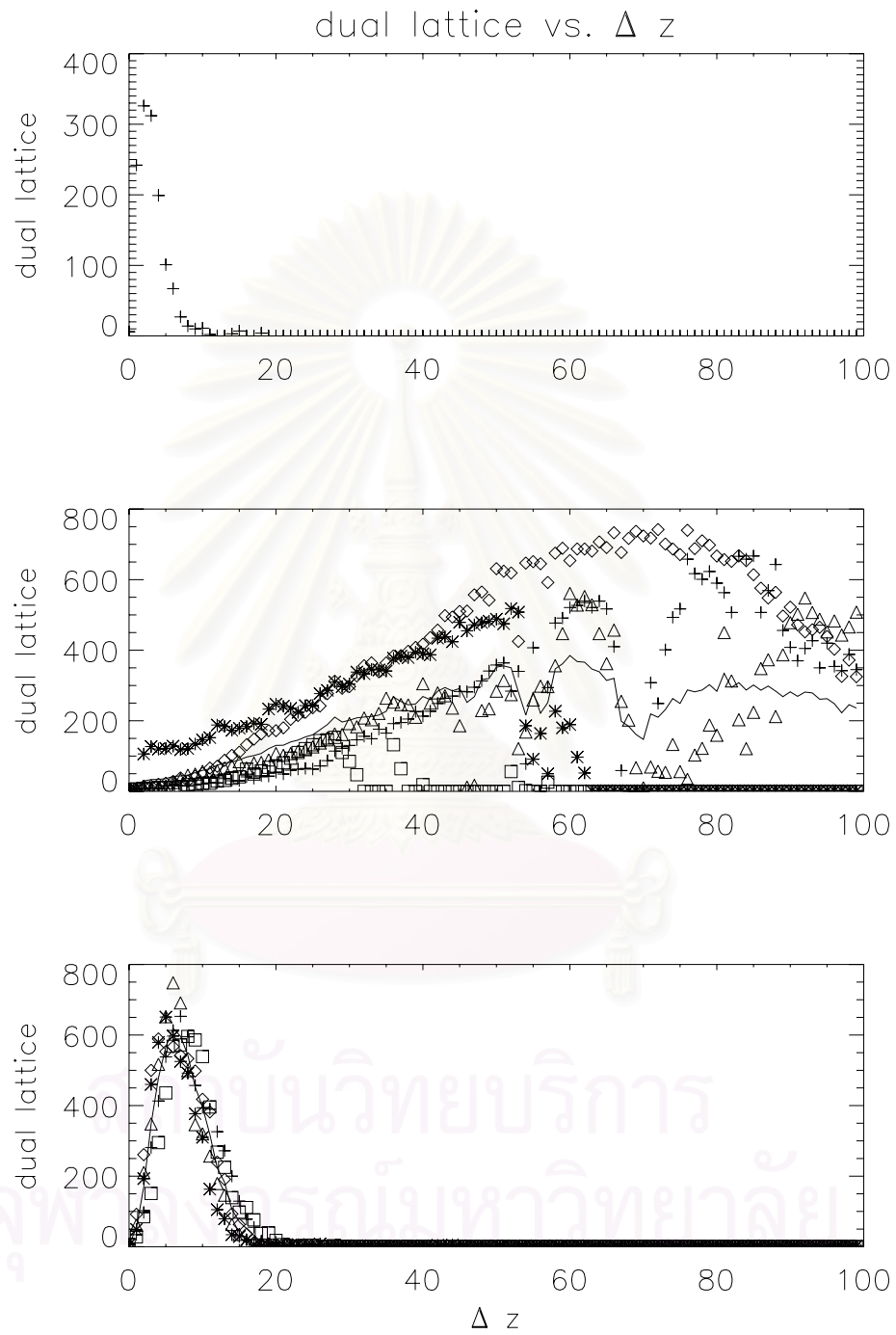


Figure 4.47: Dual lattice number vs.  $\Delta z$  when the parallel length scale is  $5.0\lambda_{\perp}$ .

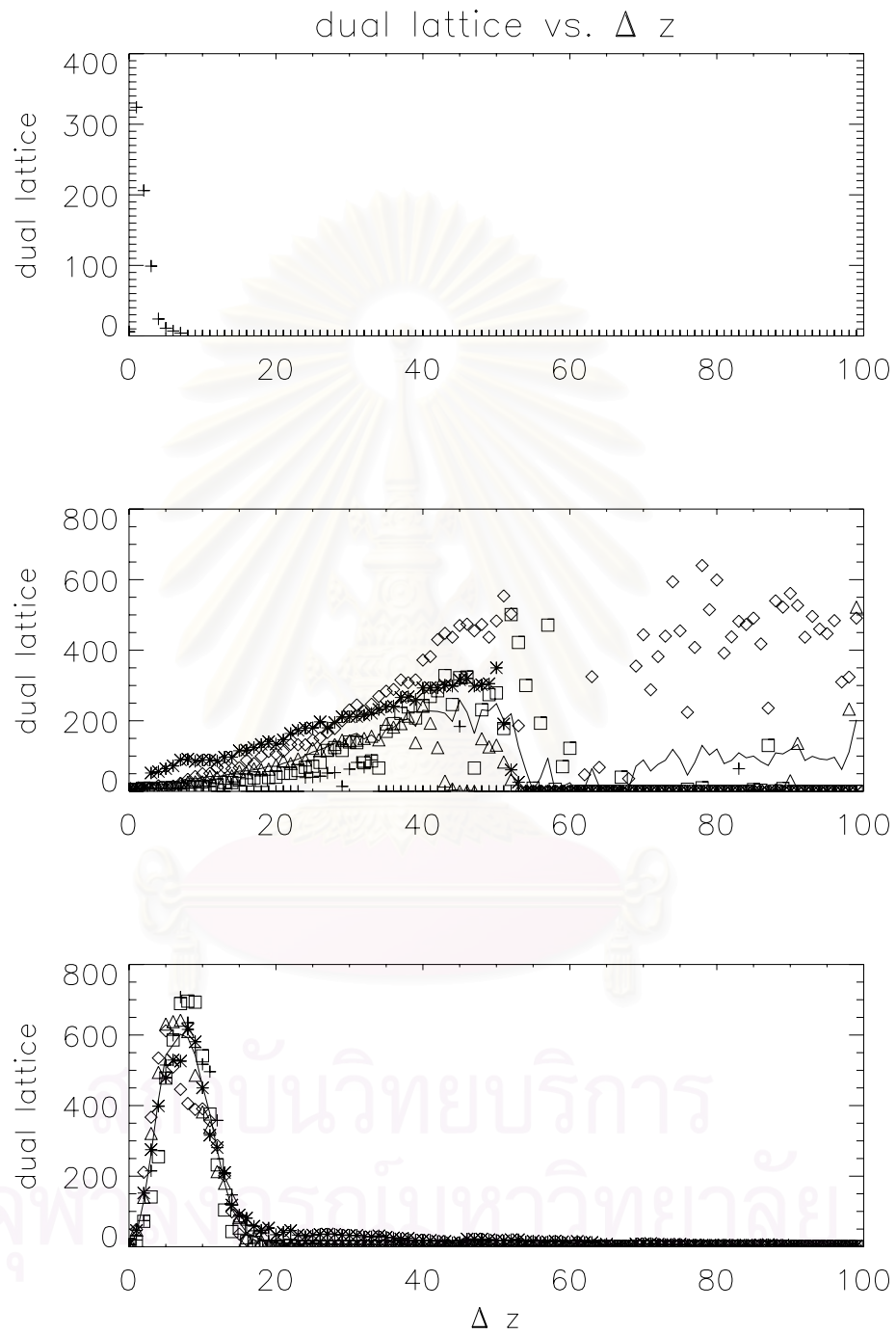


Figure 4.48: Dual lattice number vs.  $\Delta z$  when the parallel length scale is  $10.0\lambda_{\perp}$ .

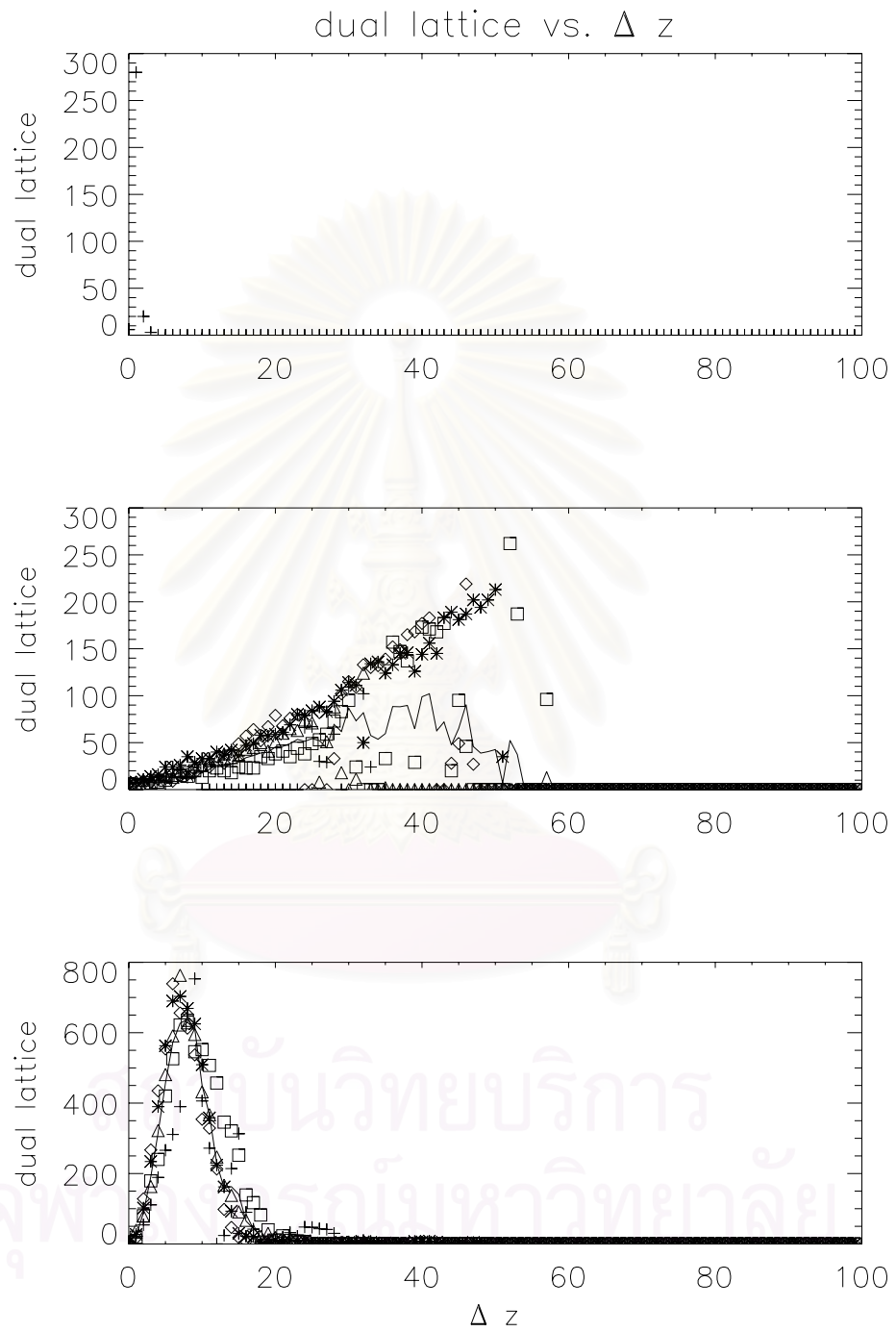


Figure 4.49: Dual lattice number vs.  $\Delta z$  when the parallel length scale is  $20.0\lambda_{\perp}$ .



For the perpendicular scale length ( $\lambda_{\perp}$ ), we use the values of this variable as 2.0, 5.0, 10.0, 20.0, and 40.0. This parameter is related to the ultrascale ( $\tilde{\lambda}$ ) and the sizes of the magnetic islands in the 2D turbulence. Thus,  $\lambda_{\perp}$  has no effect on the group of magnetic field lines in the pure slab field with random initial  $z$  (Figures 4.50 to 4.54).

When the energy ratio between the slab and 2D turbulence is 99:1, as  $\lambda_{\perp}$  increases, the  $\Delta z$  range of the peak width decreases and the peak appears at higher  $\Delta z$ . This because of the small value of  $\lambda_{\perp}$  (small magnetic island size), for which the group of magnetic field lines can break apart easily and can be trapped over a small perpendicular scale. Thus, the graph of the dual lattice number rises quickly and has a long width in  $\Delta z$ . On the other hand, if  $\lambda_{\perp}$  is large (large magnetic islands), the group of magnetic field lines is trapped over a large perpendicular scale. Therefore, the graph of the dual lattice number rises more slowly and has a shorter width in  $\Delta z$ .

When the ratio of the energy between the slab and 2D turbulence is 20:80, the graph of the dual lattice number shows that the starting location (near an O-point or an X-point) has an effect on the rate of separation or the diffusion of the group of magnetic field lines.

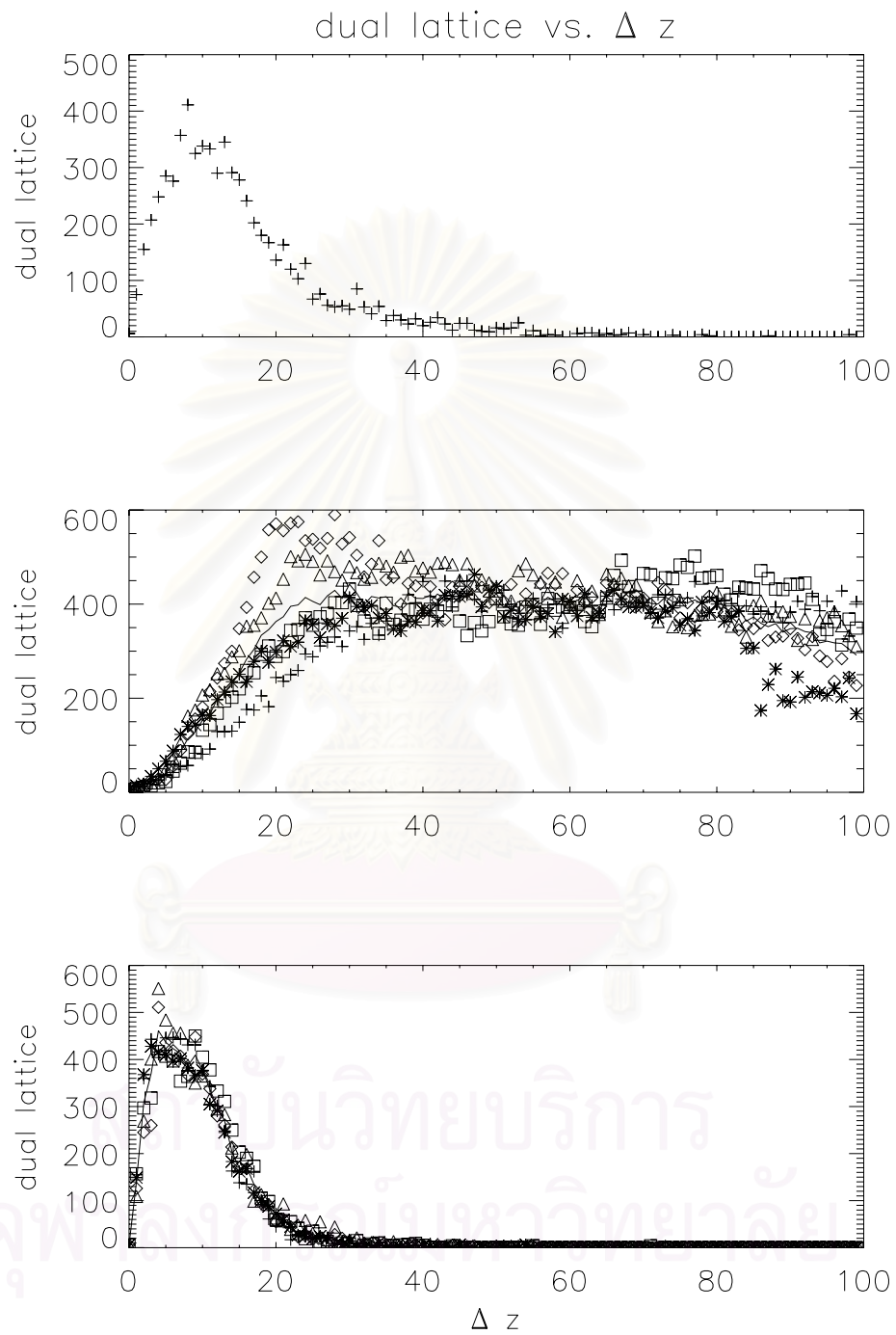


Figure 4.50: Dual lattice number vs.  $\Delta z$  when the perpendicular length scale is 2.0.

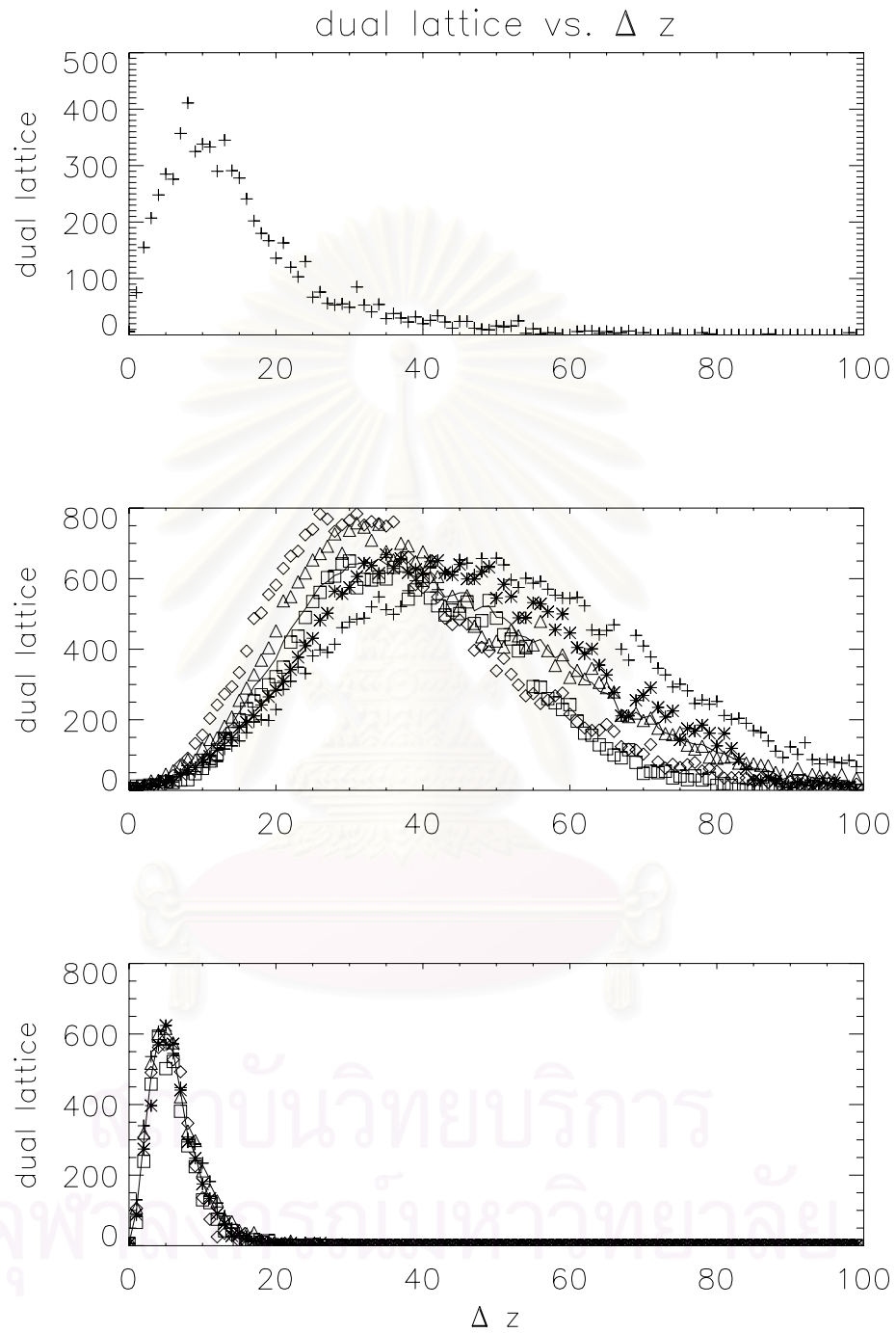


Figure 4.51: Dual lattice number vs.  $\Delta z$  when the perpendicular length scale is 5.0.

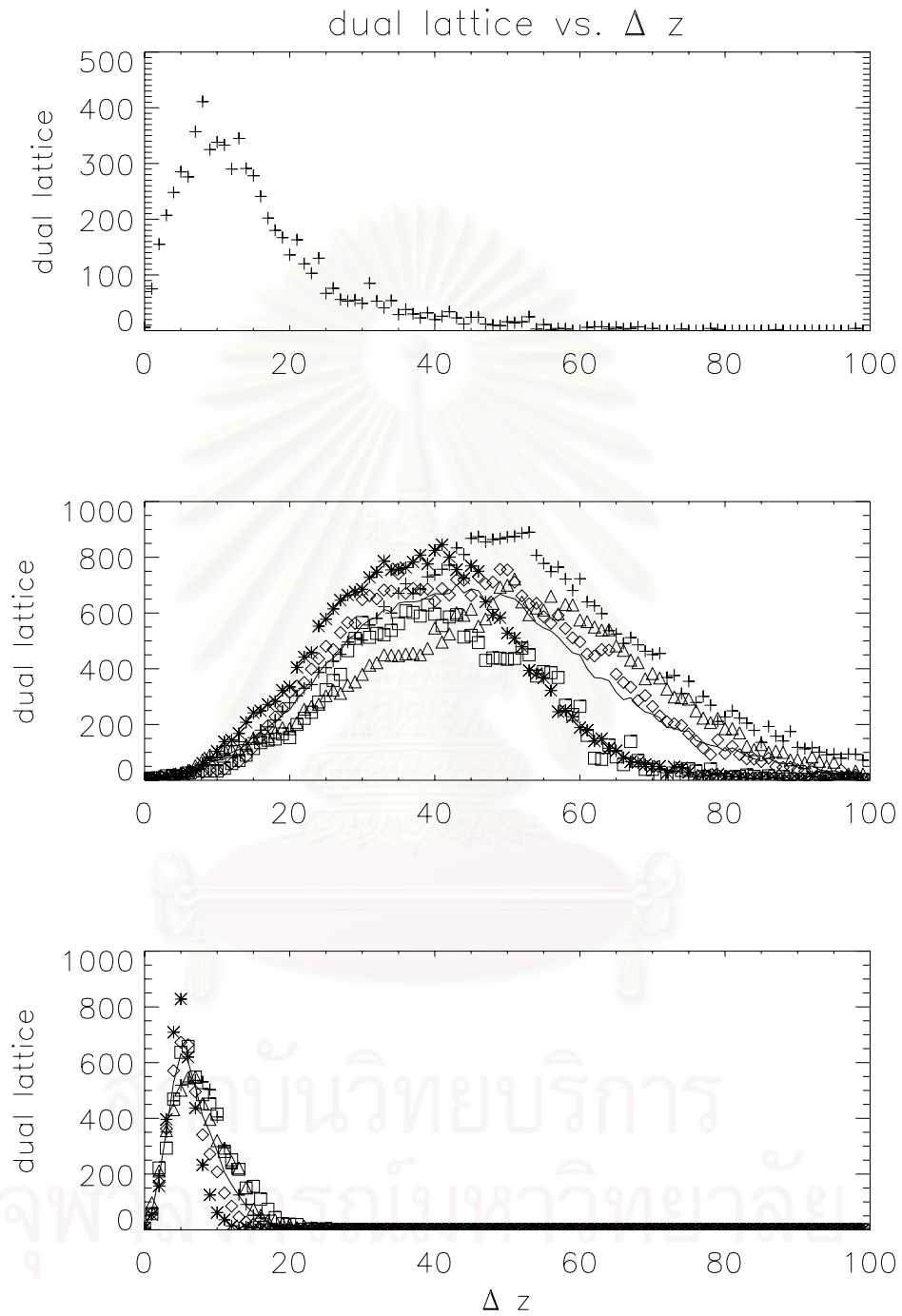


Figure 4.52: Dual lattice number vs.  $\Delta z$  when the perpendicular length scale is 10.0.

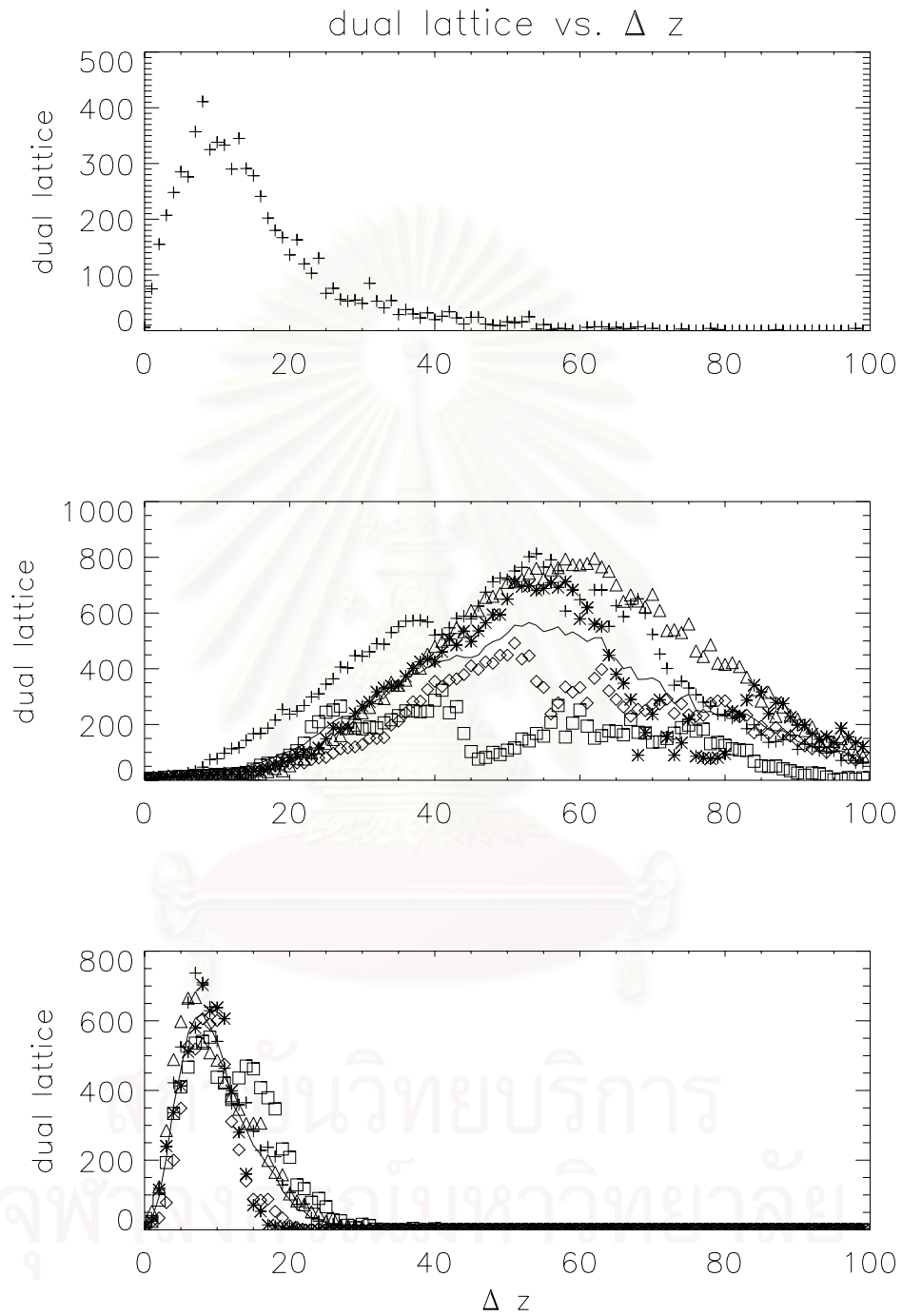


Figure 4.53: Dual lattice number vs.  $\Delta z$  when the perpendicular length scale is 20.0.

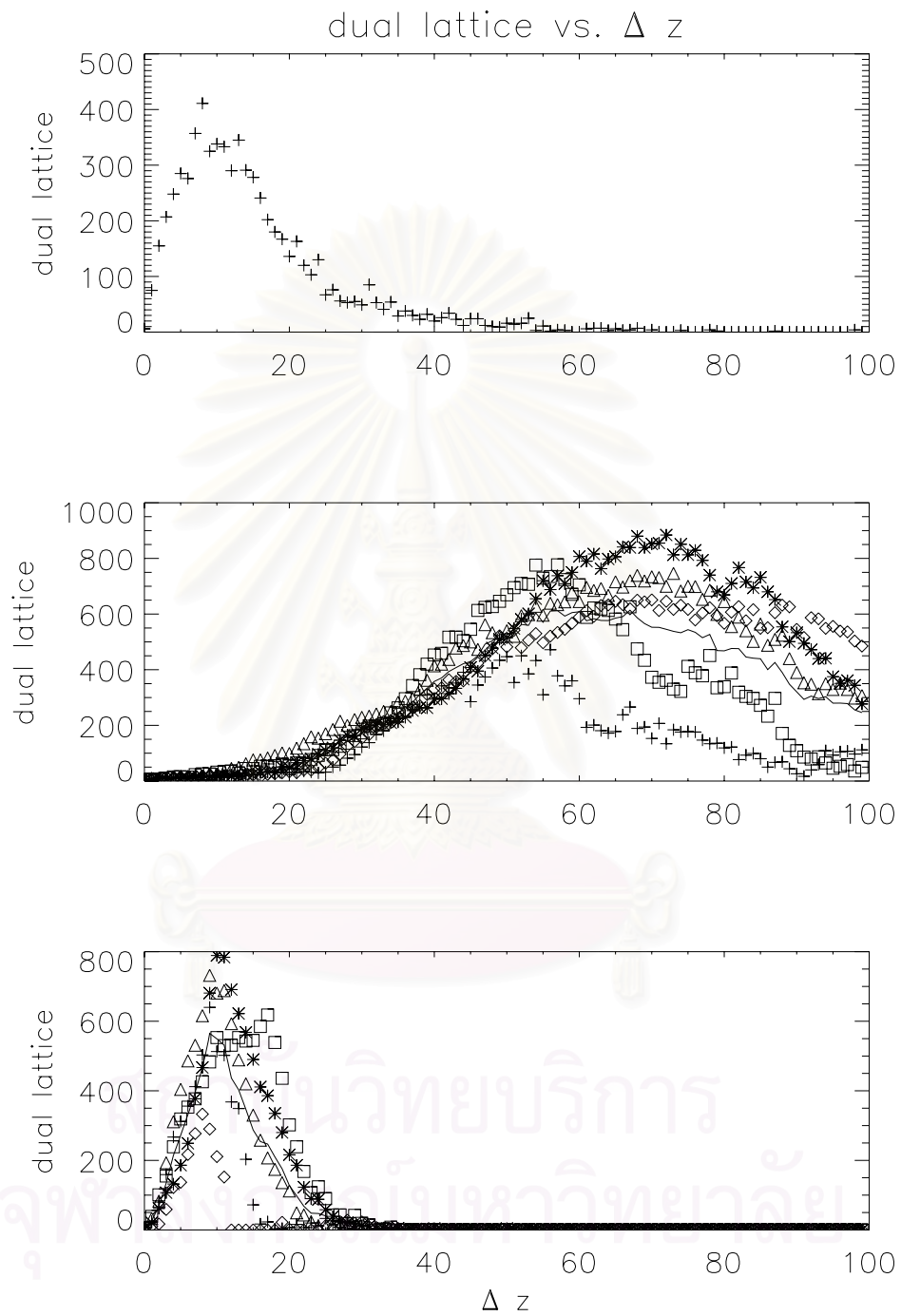


Figure 4.54: Dual lattice number vs.  $\Delta z$  when the perpendicular length scale is 40.0.

## 4.4 Principal Component

For the Principal Component Method, we measure two variables: the length of the longer principal component and the ratio between the principal components. We vary the energy ratio between slab turbulence and 2D turbulence as 99:1, 90:10, 50:50, and 20:80 by starting all of the magnetic field lines at the same initial  $z$  but at random locations in a finite circle in the  $x$ - $y$  plane. The magnetic field lines in the pure slab field with random initial positions are used to be the control run.

First, we consider the length of the longer principal axis. For the pure slab case, the results show that the magnetic field lines with random initial  $z$  are diffusive (Fig. 4.60). The increasing rate depends on  $z^{1/2}$ , which implies that the group of the magnetic field lines is diffusive. Thus, the simulation of magnetic field lines with random initial  $z$  in the pure slab turbulence is a good control run. For the slab+2D field with all of the magnetic field lines starting at the same  $z$ , the length of the longer principal axis increases continually for all energy ratios between the slab and 2D turbulence (Figure 4.61 to 4.64). However, the rate of increase is not equal for each energy ratio. The ordering is 20:80 > 50:50 > 90:10 > 99:1. Thus, the group of the magnetic field lines expands because of the separation of magnetic field lines. For the separation of magnetic field lines, the slab turbulence does not contribute directly (Ruffolo et al. 2004). Moreover, when the energy ratio between the slab and 2D turbulence is 99:1, at low  $\Delta z$ , the graph of the longer principal axis vs.  $\Delta z$  is a straight line. In this region, the behavior of the group of magnetic field lines is free streaming because the 2D motion is not yet diffusive.



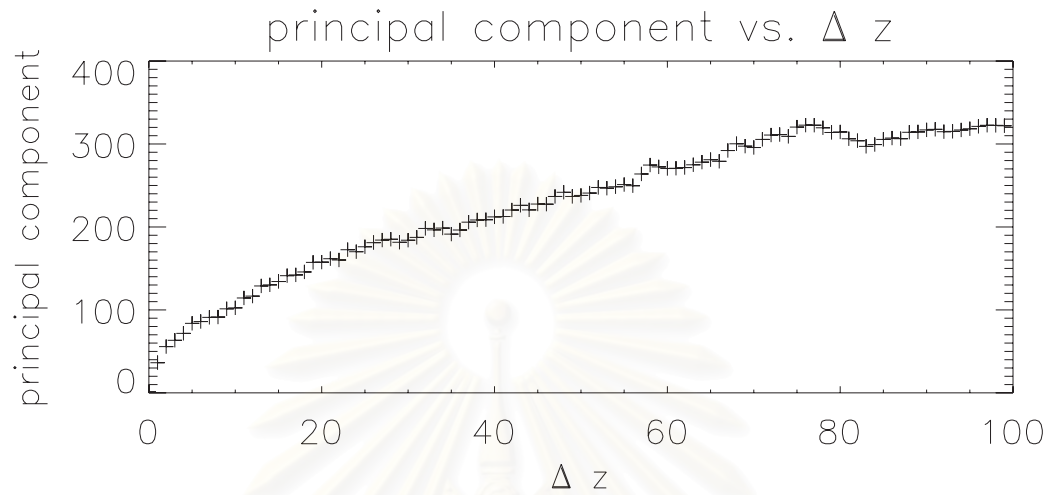


Figure 4.55: The longer principal component vs.  $\Delta z$  for a pure slab field, starting with random initial positions in  $z$ .

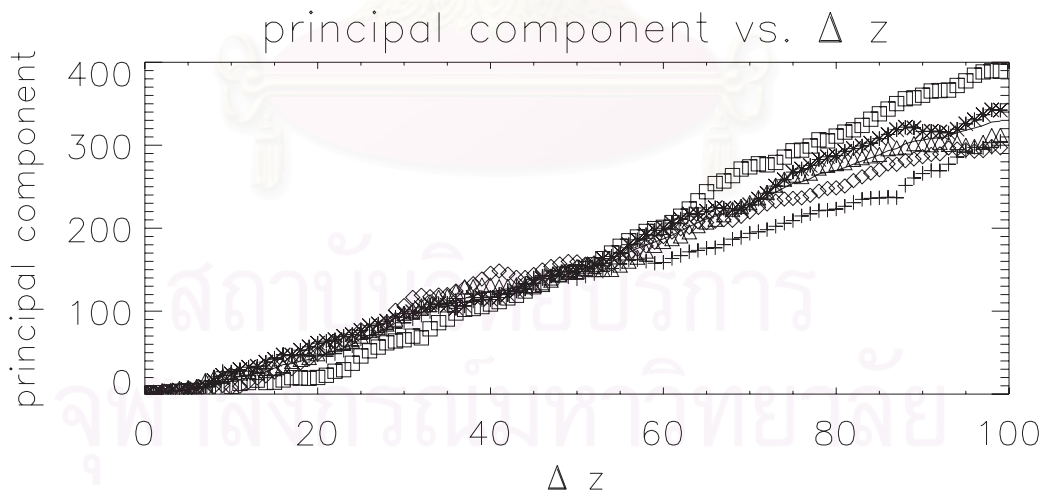


Figure 4.56: The longer principal component vs.  $\Delta z$  when the energy ratio between the slab and 2D turbulence is 99:1.

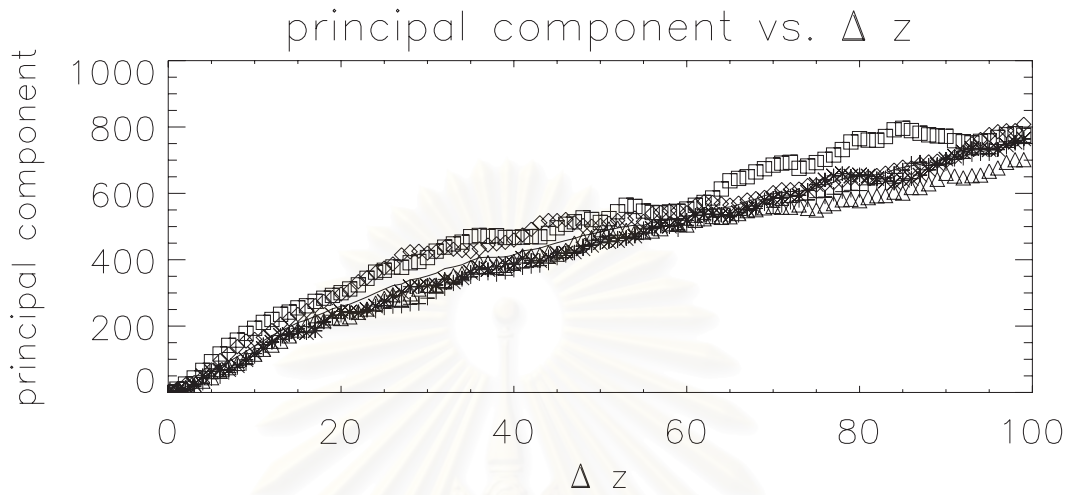


Figure 4.57: The longer principal component vs.  $\Delta z$  when the energy ratio between the slab and 2D turbulence is 90:10.

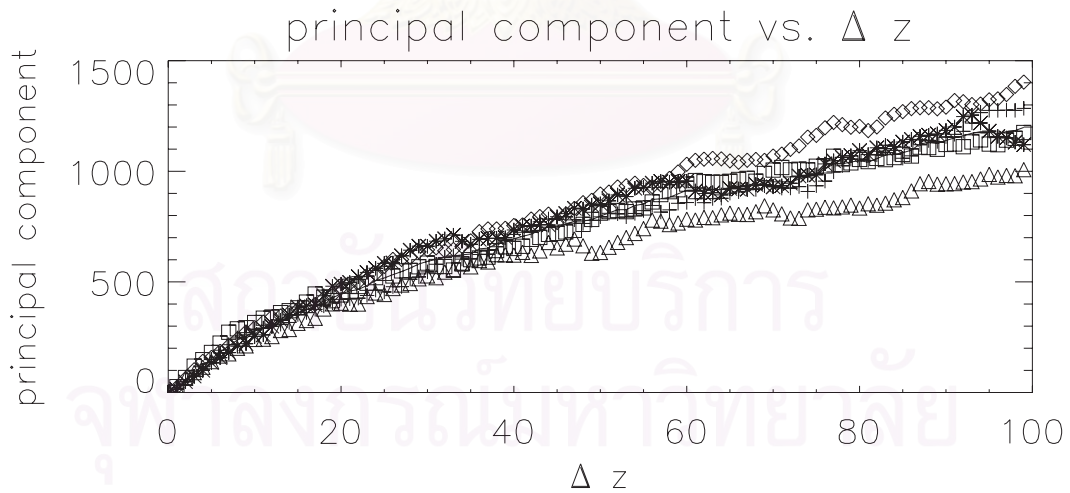


Figure 4.58: The longer principal component vs.  $\Delta z$  when the energy ratio between the slab and 2D turbulence is 50:50.

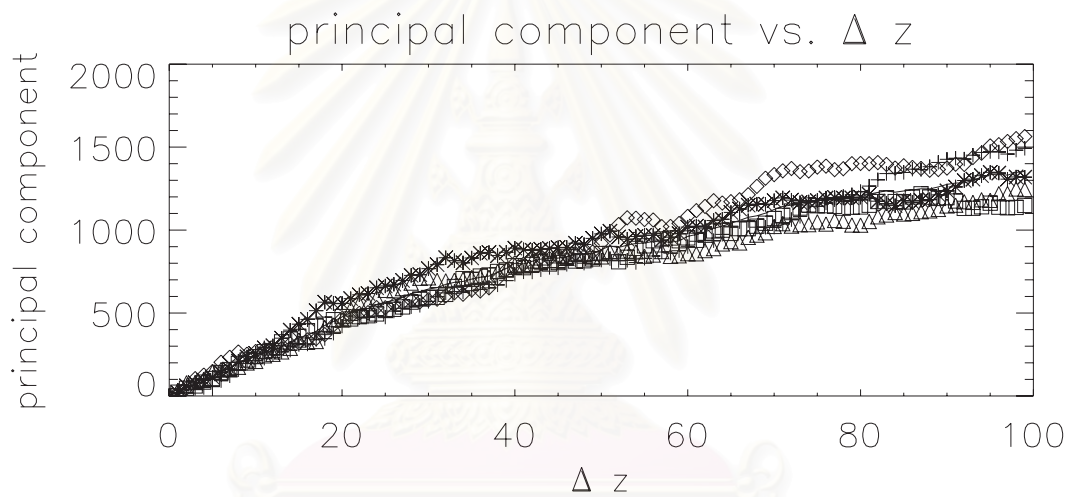


Figure 4.59: The longer principal component vs.  $\Delta z$  when the energy ratio between the slab and 2D turbulence is 20:80.

สถาบันวิทยบริการ  
จุฬาลงกรณ์มหาวิทยาลัย

Now we consider the ratio between the longer principal axis and the shorter principal axis vs.  $\Delta z$ . For a pure slab field with random initial positions in  $z$ , the group of magnetic field lines diffuses with a similar rate in all directions in the  $x$ - $y$  plane. Therefore, the ratio between the longer principal axis and the shorter principal axis is close to one over all  $\Delta z$  (Fig. 4.65). For the slab+2D field, we can separate the graphs of the ratio between the longer principal axis and the shorter principal axis vs.  $\Delta z$  into two regions. At low  $\Delta z$  ( $\Delta z = 0 \rightarrow 10$ ,  $\Delta z = 0 \rightarrow 15$ ,  $\Delta z = 0 \rightarrow 20$ , and  $\Delta z = 0 \rightarrow 35$  when the energy ratio of the slab to 2D turbulence is 20:80, 50:50, 90:10, and 99:1, respectively), the ratio between the longer principal axis and the shorter principal axis swings widely, mostly much higher than one (Figures 4.66 to 4.69). This is because the group of magnetic field lines is sheared by the magnetic potential as we discussed in Chapter III. At higher  $\Delta z$ , the ratio between the longer principal axis and the shorter principal axis converges to one. This is because the effect of the slab turbulence makes the group of magnetic field lines diffuse in the direction perpendicular to the contour of the magnetic potential. Thus, the distances at  $\Delta z = 10, 15, 20$ , and 35 for the energy ratio between the slab and 2D turbulence of 20:80, 50:50, 90:10, and 99:1, respectively, are the distances for the 2D turbulence to randomize the distribution.

Moreover, when the energy ratio between the slab and 2D turbulence is 20:80, the group of magnetic field lines in the representations presented by  $\Delta$  and  $\square$  has initial positions near an O-point, so they are trapped in a magnetic island. We can see that the ratio between the longer principal axis and the shorter principal axis of these representations is much higher than one over high  $\Delta z$ . Thus, the ratio between the longer principal axis and the shorter principal

axis when the energy ratio between the slab and 2D turbulence is 20:80 depends on the shape of the magnetic island if the initial positions of the magnetic field lines are near an O-point. For the other representations, the field lines start near an X-point. Near X-points, the magnetic field lines can shear quickly at low  $\Delta z$ , so the ratio between the longer principal axis and the shorter principal axis has a high value. However, at high  $\Delta z$ , the group of magnetic field lines starting near an X-point will have high diffusion perpendicular to the contour of the magnetic potential. Therefore the ratio between the longer principal axis and the shorter principal axis converges to one quickly. For other energy ratios, the effect of the initial position of the group of magnetic field lines is not as clear. When the slab turbulence dominates the magnetic field line trajectory more than the 2D turbulence, the magnetic field lines spread out more than shear.

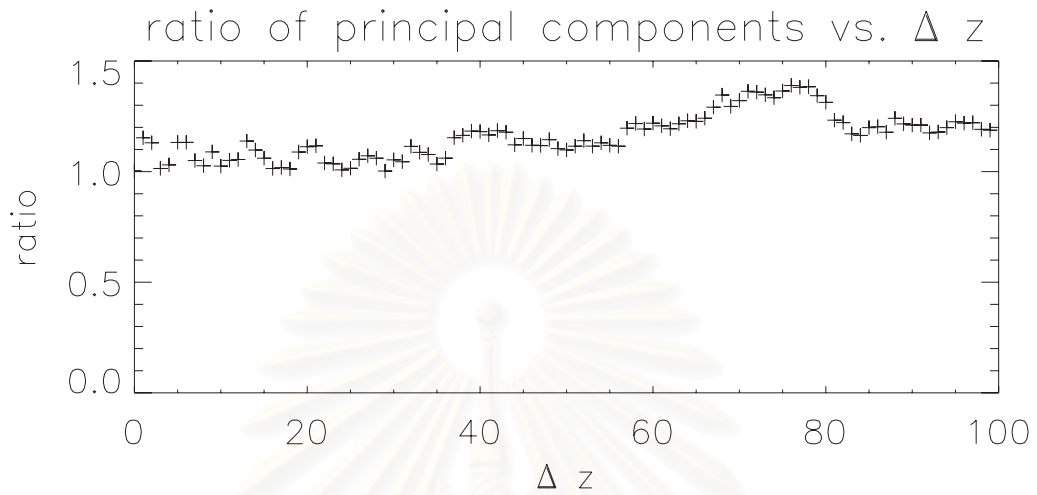


Figure 4.60: Ratio of principal components vs.  $\Delta z$  for a pure slab field, starting with random initial positions in  $z$ .

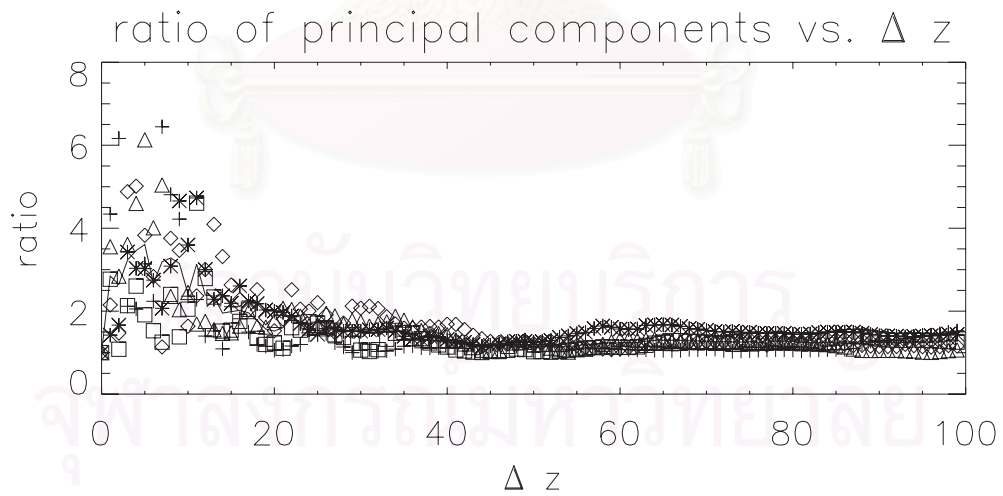


Figure 4.61: Ratio of principal components vs.  $\Delta z$  when the energy ratio between the slab and 2D turbulence is 99:1.

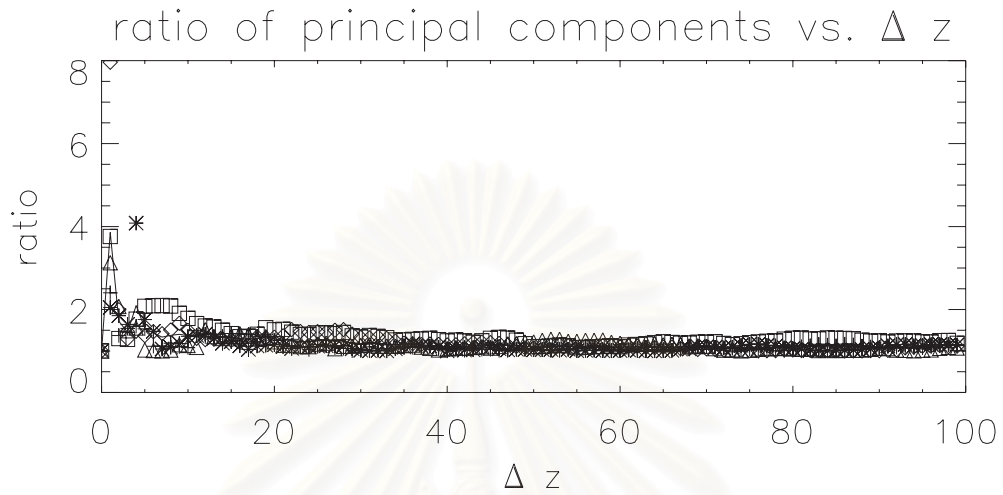


Figure 4.62: Ratio of principal components vs.  $\Delta z$  when the energy ratio between the slab and 2D turbulence is 90:10.

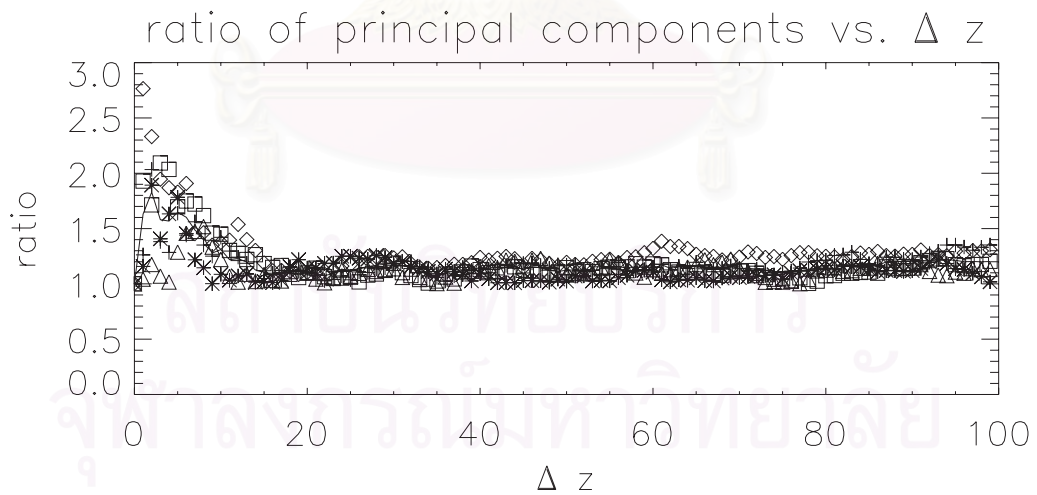


Figure 4.63: Ratio of principal components vs.  $\Delta z$  when the energy ratio between the slab and 2D turbulence is 50:50.



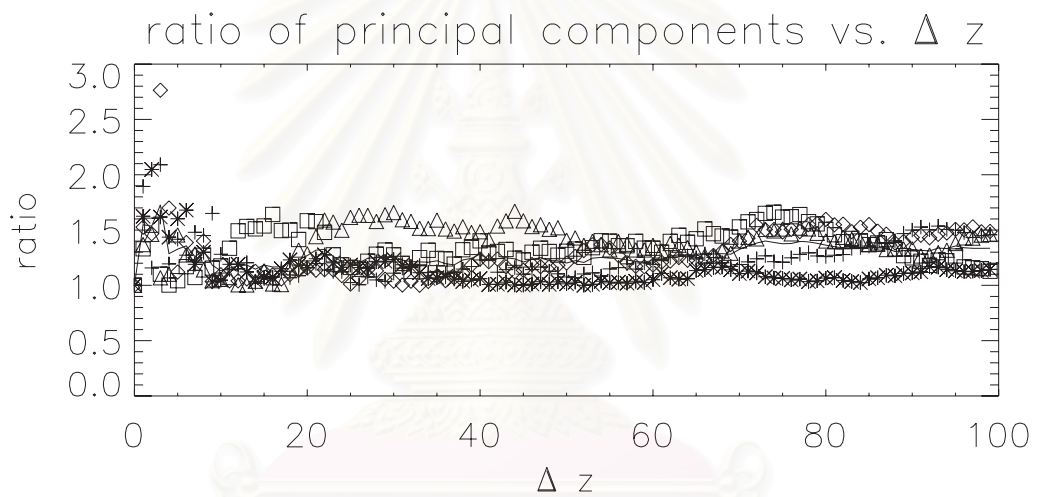


Figure 4.64: Ratio of principal components vs.  $\Delta z$  when the energy ratio between the slab and 2D turbulence is 20:80.

สถาบันวิทยบริการ  
จุฬาลงกรณ์มหาวิทยาลัย

# CHAPTER V

## SUMMARY

In this chapter, we summarize the results from all of the data analysis methods. In this project, we aim to understand the separation of the magnetic field lines and measure the distance over which the group of the magnetic field lines breaks apart and diffuses as in the dropouts of the SEPs. We develop and use the methods of box counting, anisotropy, dual lattice, and principal components to attain these objectives.

In the simulations, we set the initial position of the magnetic field lines in a certain circle in the  $x - y$  plane. For the initial positions of the magnetic field lines in  $z$  direction, we divide into two cases. In the case of the pure slab field, the initial positions of the magnetic field lines in the  $z$  direction are random in order to visualize the distribution of the magnetic field lines. In the case of the slab+2D field, we set all of the initial positions of the magnetic field lines at  $z = 0$ . From the initial positions, we trace and collect the positions of the magnetic field lines along  $\Delta z$ .

For the Box-Counting Method, we count the number of boxes which contain the magnetic field lines. The negative slope of the log-log plot between the number of boxes containing magnetic field lines and the box size can be determined as the fractal dimension of that group of magnetic field lines. However, the results show that the fractal dimension of the group of magnetic field lines at each  $\Delta z$  depends strongly on the number of magnetic field lines.

To determine the field line separation, we use the Anisotropy Method and the Dual Lattice Method. Both methods are developed from the Box-Counting Method but have the different details. The Anisotropy Method finds the number of boxes in which the magnetic field lines in those boxes are anisotropic (not uniform) in the  $x - y$  plane. A box with an anisotropy of magnetic field lines in the  $x - y$  plane can be determined to be at the edge of a group of magnetic field lines. The Dual Lattice Method compares the number of magnetic field lines in each box with the neighboring boxes in both  $x$  and  $y$  directions. If the ratio of the number of the magnetic field lines in that box to that neighboring box is greater than six (or less than  $1/6$ ), that box can be counted to be at the edge of a group of magnetic field lines. The anisotropy number and the dual lattice number are related to the boundary length of the groups of the magnetic field lines. Because of the separation of neighboring magnetic field lines, the group of magnetic field lines will increase its size and can also break apart into smaller groups, which makes the sum of the edge length increase, too.

We can understand the results in terms of the theory of field line separation (Ruffolo et al. 2004). When changing the fluctuation energy and the parallel length scale, we found that in the pure slab case with random initial positions in  $z$ , the field line separation depends on the slab fluctuations with  $D_{sep} = 2D_{slab}$ . In the slab+2D case with the initial positions of the magnetic field lines at  $z = 0$ , the field line separation depends on the both slab and 2D turbulence with  $D_{sep} = 2D_{2D}^2/D_{\perp}$  where  $D_{\perp} = (D_{slab} + \sqrt{D_{slab}^2 + 4D_{2D}^2})/2$ .

The initial circle size of the group of magnetic field lines is analogous with the injection area of the solar energetic particles. The small initial circle is analogous with the injection area for the impulsive solar flares in which the particles are ejected over a small region. In this case, the results show the anisotropy number and the dual lattice number rising and falling, implying that the group of magnetic field lines breaks apart into smaller groups and then diffuses. On the other hand, for a large initial circle, the anisotropy number and the dual lattice number have high values at low  $\Delta z$  and decrease along  $\Delta z$ . At low  $\Delta z$ , the group of magnetic field lines can only diffuse without breaking apart as in the control run of Ruffolo et al. (2003). This case is related to the gradual solar flares, in which the particles are ejected over a large region on the surface of the Sun. For the gradual flares we cannot observe the dropout phenomena.

For the changing perpendicular length scale, the results have a physical meaning similar to changing the size of the initial circle. Increasing the perpendicular length scale is analogous with reducing the initial circle and vice versa.

For the Principal Component Method, we find the principal components to characterize the distribution of the data. We measure two properties of the principal components: the length of the longer axis and the ratio of those two axes. In the pure slab case with the initial positions of the magnetic field line random in  $z$ , the results show that the length of the longer principal component is proportional to  $(\Delta z)^{1/2}$  all along  $\Delta z$ . Thus, the group of magnetic field lines is diffusive for all  $\Delta z$ . In the slab+2D case with varying energy ratios and setting the initial positions of the magnetic field line at  $z = 0$ , the results from the ratio of the principal components show that there are two regions along  $\Delta z$ . At low  $\Delta z$ , the group of magnetic field lines is sheared by the 2D potential more

than diffusive while at higher  $\Delta z$ , the magnetic field lines diffuse in the direction perpendicular to the contour of the 2D potential function.

In summary, we have explained the characteristics of the magnetic field line trapping and separation in turbulent fields, which are qualitatively consistent with the dropout phenomena of the SEPs. We describe conditions and length scales over which dropouts can occur.



สถาบันวิทยบริการ  
จุฬาลงกรณ์มหาวิทยาลัย

# REFERENCES

- Bieber, J. W., Matthaeus, W. H., Smith, C. W., Wanner, W., Kallenrode, M.-B., and Wibberenz, G. Proton and electron mean free paths: The Palmer consensus revisited. *Astrophys. J.* **420** (1994): 294-306.
- Bieber, J. W., Evenson, P., Dröge, W., Pyle, R., Ruffolo, D., Rujiwarodom, M., Tooprakai, P., and Khumlumlert, T. Spaceship Earth Observations of the Easter 2001 Solar Particle Event. *Astrophys. J. Lett.* **601** (2004) L103-L106.
- Chuychai, P., Model of random magnetic fields and some implications for turbulence structure and particle transport in the heliosphere. Ph.D. Thesis. Chulalongkorn University, 2005.
- Chuychai, P., Ruffolo, D., Matthaeus, W. H., Rowlands, G. Suppressed diffusive escape of topologically trapped magnetic field lines. *Astrophys. J. Lett.* **633** (2005): L49-L52.
- Corrsin, S. in Advances in Geophysics, Volume 6: Atmospheric diffusion and air pollution ed. F. Frenkel and P. Sheppard, New York: Academic Press, 1959.
- Foukal, P., Solar Astrophysics New York: Wiley-Interscience, 1989.
- Giacalone, J., Jokipii, J. R., and Mazur, J. E. Small-scale gradients and large-scale diffusion of charged particles in the heliospheric magnetic field. *Astrophys. J. Lett.* **532** (2000): L75-L78.
- Kolmogorov, A. N. The local structure of turbulence in incompressible viscous fluids for very large Reynolds numbers. *Dokl. Akad. Nauk SSSR* **30** (1941): 299-303.

- Matthaeus, W. H., Goldstein, M. L., and Roberts, D. A. Evidence for the presence of quasi-two-dimensional nearly incompressible fluctuations in the solar wind. J. Geophys. Res. **95** (1990): 20673-20683.
- Matthaeus, W. H., Gray, P. C., Pontius, D. H., Jr., and Bieber, J. W. Spatial structure and field-line diffusion in transverse magnetic turbulence. Phys. Rev. Lett. **75** (1995): 2136-2139.
- Mazur, J. E., Mason, G. M., Dwyer, J. R., Giacalone, J., Jokipii, J. R., and Stone, E. C. Interplanetary magnetic field line mixing deduced from impulsive solar flare particles. Astrophys. J. Lett. **532** (2000): L79-L82.
- McKibben, R. B., Connell, J. J., Lopate, C., Zhang, M., Balogh, A., Dalla, S., Marsden, R. G., Sanderson, T. R., Tranquille, C., Anglin, J. D., Kunow, H., Müller-Mellin, R., Heber, B., Raviart, A., and Paizis, C. ULYSSES COSPIN observations of the energy and charge dependence of propagation of solar energetic particles to the Sun's south polar regions. Proc. 27th Int. Cosmic Ray Conf. (Hamburg) **8** (2001): 3281-3284.
- Meechai, J., Trapping boundary of turbulent magnetic field lines. B.Sc. Senior project. Chulalongkorn University, 2004.
- Pongkitiwanchkul, P., Sawtooth mechanism of particle acceleration at shocks in random magnetic fields. M.Sc. Thesis. Chulalongkorn University, 2005.
- Pope, S. B., Turbulent Flows Cambridge: Cambridge University Press, 2000.
- Press, W. H., Teukolsky, S. A., Vetterling, W. T., and Flannery, B. P. Numerical recipes in FORTRAN: The art of scientific computing Cambridge: Cambridge University Press, 1992.
- Richardson, L. F., Water prediction by numerical process Cambridge: Cambridge University Press, 1922.



- Ruffolo, D., Matthaeus, W. H., and Chuychai, P. Trapping of solar energetic particles by the small-scale topology of solar wind turbulence. Astrophys. J. Lett. **597** (2003): L169-L172.
- Ruffolo, D., Matthaeus, W. H., and Chuychai, P. Separation of magnetic field lines in two-component turbulence. Astrophys. J. **614** (2004): 420-434.
- Simanca, S. R. and Sutherland, S. Mathematical Problem Solving with Computers. Lecture Notes. Stony Brook University, USA, 2002.
- Smith, L. I. A tutorial on Principal Components Analysis. Lecture Notes. University of Otago, New Zealand, 2002.
- Tennekes, H., and Lumbe, J. L. A First Course in Turbulence Massachusetts: the MIT Press, 1994.



สถาบันวิทยบริการ  
จุฬาลงกรณ์มหาวิทยาลัย

## VITAE

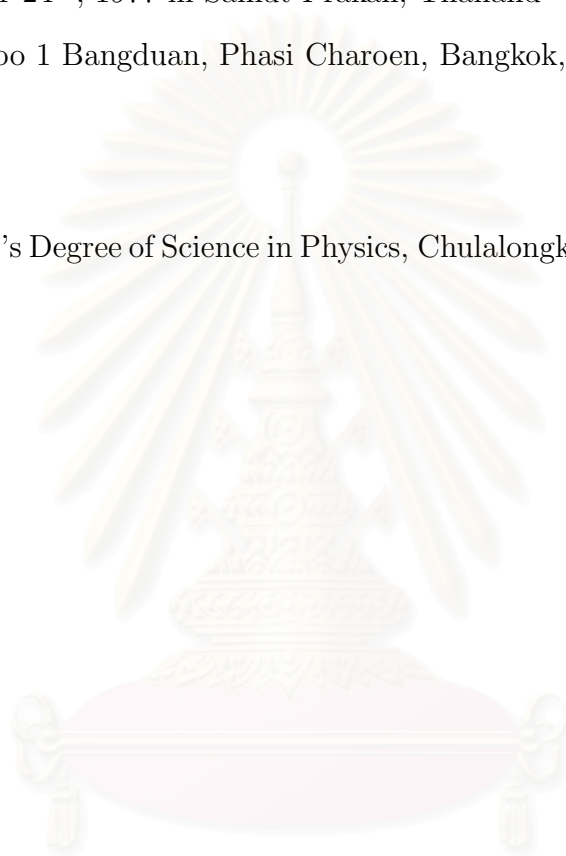
**Name:** Mr. Nimit Kimpraphan

**Born:** November 24<sup>th</sup>, 1977 in Samut Prakan, Thailand

**Address:** 43 Moo 1 Bangduan, Phasi Charoen, Bangkok, Thailand

**Education:**

**1999** Bachelor's Degree of Science in Physics, Chulalongkorn University, Bangkok, Thailand



สถาบันวิทยบริการ  
จุฬาลงกรณ์มหาวิทยาลัย